7-12-2014

Structural Scaling Metrics For Tensioned-Blanket Space Systems

Jeremy Banik
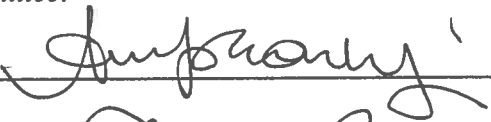
Jeremy A. Banik

Candidate

Civil Engineering

Department

This dissertation is approved, and it is acceptable in quality
and form for publication:

Approved by the Dissertation Committee:

Dr. Arup Maji, Chairperson

Dr. Percy Tang-Tat Ng

Dr. Christopher Jenkins

Dr. Brandon Arritt

i

**STRUCTURAL SCALING METRICS FOR TENSIONED-BLANKET
SPACE SYSTEMS**

BY

JEREMY A. BANIK

B.S., Mechanical Engineering, South Dakota School of Mines and Tech, 2004
M.S., Mechanical Engineering, South Dakota School of Mines and Tech, 2005

DISSERTATION

Submitted in Partial Fulfillment of the
Requirements for the Degree of

Doctor of Philosophy

Engineering

The University of New Mexico
Albuquerque, New Mexico

May, 2014

DEDICATION

   This work is dedicated to my bride, Stephanie, an enduring source of inspiration and support. Any recognition given me is equally due her. This is also dedicated to my young tribe—Caleb, Keira, and Liam—within whom my most meaningful legacy will be carried.

ACKNOWLEDGMENTS

STRUCTURAL SCALING METRICS FOR TENSIONED-BLANKET SPACE SYSTEMS

by

Jeremy A. Banik

B.S., MECHANICAL ENGINEERING,
SOUTH DAKOTA SCHOOL OF MINES AND TECHNOLOGY, 2004
M.S., MECHANICAL ENGINEERING,
SOUTH DAKOTA SCHOOL OF MINES AND TECHNOLOGY, 2005
PH.D., ENGINEERING,
UNIVERSITY OF NEW MEXICO, 2014

ABSTRACT

Structural metrics have been used for nearly a century to provide designers with simple, rational tools for comparing the mass performance of aircraft and spacecraft platforms. Large space structures designers and evaluators rely on metrics to compare boom, telescope, and long antenna architectures. In this work, scaling metrics are established for rectangular flexible blanket solar array structural architectures. The approach takes advantage of the fact that an ideal solar array structure is a system of coupled beam and tensioned blanket components rather than the typical simplifying approach of considering only one beam with a distributed mass as the blanket. A fundamental frequency relation is developed to represent a beam-cable system in a clamped-free boundary condition. A structural model of the array is developed on the basis of minimum mass and minimum beam cost using constraint analysis methods and

weight equations. This structural model expression is solved numerically using root finding algorithms, is transformed into an approximate expression using regression techniques, and the terms are symbolically related into scaling parameters and scaling indices. These metrics enable straightforward comparison of a wide range of array sizes, geometric forms, column types, column quantities, blanket mass densities, acceleration loads, fundamental frequencies, and power production values. Finally, practical application and accuracy of these metrics is demonstrated by comparing to the latest heritage tensioned blanket systems on-orbit and those still in prototype form: Terra (EOS-AM), the Milstar constellation, the International Space Station, MegaROSA, and MegaFlex.

TABLE OF CONTENTS

LIST OF FIGURES

LIST OF TABLES

CHAPTER 1.   INTRODUCTION

Structural engineering is the discipline of combining material types and member elements to efficiently work together as a collective structural system that supports loads. The geometric arrangement of and materials used in this structural system is collectively identified as the structural architecture. The selection of a structural architecture for a particular usage is based upon the external loading applied and the design constraints driving that application scenario. Prudent aircraft and spacecraft structural design also demands minimization of the structural mass.

1.1   Bridge Analogy

An analogy in civil engineering would be the selection of the appropriate type of structure and material to build a bridge across the Bering Strait, a distance of 53 miles. Many different structural architectures are available to the design engineer who must first consider the requirements: the number and weight of vehicles; expected earthquake and wind loads; gravity-induced loads; free-span distance; the cost to manufacture and maintain; aesthetics; durability in the context of the environment; and water depth through the channel.

A wooden beam would collapse under its own weight for spans of only a few dozen meters; thus tens of thousands of pier columns would be required along the 53 mile stretch. On the other hand, a beam formed from a carbon fiber composite into a complex non-prismatic tube is more mass efficient and is technically feasible but prohibitively expensive.

Next consider a truss bridge. Because of increased structural depth over a solid rod or hollow tube, a truss has higher structural efficiency and thus can reach longer spans between piers. However, for spans greater than a few hundred meters, a suspension or cable-stayed bridge can achieve higher structural efficiency than even a truss bridge. Certainly there are other extreme cases where the span is too long for even a suspension bridge to reach given current limitations on materials, construction equipment and other technical limits.

The point to take away is that each structural architecture, type and material combination, has unique scaling characteristics that determine the range and limits of its application. Understanding these limitations also drive research and improvement in technology in the relevant field.

Technical evaluators and conceptual designers of large spacecraft structures benefit from a similar understanding of scaling limits. Metrics are especially needed at the concept formulation phase of new programs. These early decisions represent large R&D investment commitments and thus must be guided toward concepts and technology components that promise only the highest payoff for the least risk. A variety of valuable metrics and parametric relationships have been developed over several decades to serve this purpose.

1.2   Objectives, Approach, and Limitations

The present work adds to this historical repertoire by developing a set of metrics related to large tensioned-supported spacecraft payloads that are substantially planar in dimension. This payload class is identified by the three structural elements used in the

construction—a tensioned flexible blanket(s) to collect or transmit radiation energy, a compression column(s) to react the tension, and a spreader bar(s) to transfer load from the blanket to the column. This is an attractive structural system for both low and high precision spacecraft payloads due to the packaging efficiency and mass efficiency that compression structures provide over flexural structures. Tensioned-blanket photovoltaic solar arrays (i.e., flexible blanket solar arrays) and tensioned precision antenna arrays are two platforms well poised to take advantage of this structural support approach. The focus of this work is photovoltaic arrays where dimensional stability is not a driving requirement.

Previous approaches that have addressed this need are limited to a simple single beam model with the blanket mass distributed along the beam length. The approach proposed in the present study is differentiated from these previous approaches in that the solar array structural system is considered rather than just a single beam component. The system approach accounts for the dynamic interaction and mass scaling of multiple beams and blankets connected in parallel.

The advantage of addressing the problem from the system level is that the results become more relevant for a broader range of solar array architectures, namely those that are substantially rectangular in deployed geometry rather than just rectilinear. The disadvantage is that more structural terms are needed adding analytic complexity and potentially confusing the usability of the results. A balanced approach is needed between model complexity and practical usability. Structural scaling metrics must be readily understandable and quickly usable by those comparing structural architectures, those

3

considering mission concepts, and those crafting technology investment strategies. These models are not intended to serve detailed structural design activities. Instead they should provide a practical tool that helps to set investment trajectories on paths that are well-founded on solid structures principles.

1.3   Outline of Dissertation

The process by which the metrics are developed is outlined by Figure 1. This provides a roadmap through the dissertation. The first step as recorded in Chapter 2 is a systems analysis. Historical structural metrics are reviewed and flexible blanket solar array types, support column types, and blanket types are consolidated. This analysis includes historical surveys as well as projections into the future art of the possible. The outcome of this system analysis step is a comprehensive understanding of the bounds of this problem.

Chapter 3 describes the distillation of this design boundary into the absolute minimum set of solar array performance constraints and design parameters. A range of values defines a general solar array physical model that represents all practical manifestations of a rectangular-shaped flexible blanket solar array.

In Chapter 4 loading relations are developed for both the array fundamental frequency and strength. This analytical development leverages first principles, finite element techniques, and minimization techniques. Appendix A provides more detail into the finite element model used to develop the fundamental frequency relation.

Chapter 5 combines the loading equations into an array weight equation in terms of the requirement constraint terms and the array design terms. This relation is then

subjected to two objective constraints: minimize array mass and minimize beam cost. The first half of the chapter builds this array mass objective function, ultimately culminating in the apex of analytical complexity—a transcendental equation for array mass that is solved by numerical methods. The second half of this chapter starts back down the path of simplification by breaking down this complex solution into approximation model for array mass in terms of array loading terms and design terms. This simplification process leverages a modified design of experiments process along with linear and power function regression techniques. Appendix B is provided as a supplement to Chapter 5, detailing the regression analysis process. Finally in Chapter 6, terms are grouped to form the scaling parameter and scaling index. Practical application and metric accuracy is then demonstrated by comparing existing array architectures on the basis of the newly minted array scaling metrics.

Array Requirements:
$f \geq f$ required
$\alpha \geq \alpha$ required
$A \geq A$ required

Component Design
Parameters:
[EI, M, n, L, γb, wsb, wpb]

Chapter 4

Appendix A.

Develop the finite element
model of a beam-cable.

Introduce beam efficiency index:
$\mu = f\,(M,\ EI,\ wpb)$

Eliminate *M* and *EI* by rearranging frequency
and strength functions and substituting into
the beam efficiency function:
$\mu = f\,(a,\ f,\ L,\ A,\ n,\ \gamma b,\ wsb,\ wpb)$

Develop the weight equation as the sum of
beam, blanket, and bar mass terms.
Solve the function using numerical methods:
$\gamma = f\,(\mu,\ a,\ f,\ L,\ A,\ n,\ \gamma b,\ wsb,\ wpb)$

Appendix B.

Develop Mathematica-based
numerical solver code.

Chapter 5

Create approximation
model by minimizing
array mass and beam
cost as the objective
function.

Appendix C.

Use regression techniques to
extract approximate symbolic
relationships between γ, μ, and
[α, f, L, A, n, γb, wsb, wpb]

Chapter 6

Demonstrate practical
function of the metrics
on solar array examples.

Appendix D.

Metrics Users' Guide

Figure 1. Dissertation roadmap.

1.4   Photovoltaic Solar Array Overview

Essential for nearly every spacecraft, solar arrays utilize the photovoltaic effect[1] to convert solar radiation into electricity that is conditioned to power spacecraft components or charge batteries. Solar arrays started as simple body-mounts in 1958 and have progressed over the last 50 years into two structural support types: accordion-folded rigid panels and tensioned flexible blankets.[2]

The standard array type in use today is the rigid panel type. Through a series of accordion folded composite plates of thicknesses typically ranging 0.25 to 1 inches, rigid panel arrays rely on bending stiffness through structural depth for stiffness and strength. Each panel is populated with electrically connected photovoltaic cells. Rigid panel arrays have a heritage of deployment reliability, and they package into launch vehicle fairings reasonably well for most missions. But the stacked-plate packaged form factor and poor mass efficiency does not scale well to the larger array sizes needed to satisfy future government and private industry spacecraft power needs. State of the art commercial communications satellites are approaching 20 kW of total power generation with as many as seven panels per wing. But to do so, these wings require two-staged deployments of side panels, a step that increases the risk of an unsuccessful deployment. For example, one of the six-panel wings on the Loral SES-4 spacecraft launched in 2012 appeared to have had deployment challenges according to *Space News* (URL: http://www.spacenews.com/article/launch-siriusxm-satellite-delayed-solar-array-concerns, accessed 8 March 2012).

In contrast, flexible blanket photovoltaic arrays are less common. They have been used for several decades but in limited quantities, appearing on-orbit as early as 1990 on the Hubble Space Telescope.[3,4] A few years later in 1994 the U.S. Air Force launched the first of several Milstar communications satellites according to a fact sheet (URL: http://www.losangeles.af.mil/library/factsheets/factsheet.asp?id=5328, accessed 4 April 2013). Each uses a flexible blanket solar array for power generation. Two 4.3 kW array wings are shown on the Milstar space vehicle in Figure 2; each is tension-supported by a continuous longeron lattice truss compression column built by Astro Aerospace visibly extended along the center of the gold colored photovoltaic blankets in the figure. This solar array type has been successfully used on a handful of other spacecraft systems such as the International Space Station[5] (ISS) and the Terra EOS-AM[6] spacecraft, but these examples remain the exceptions rather than the standard.

Figure 2. A Milstar communications satellite with two opposing 4.3 kW tensioned photovoltaic blanket winglets each supported by a compression column.

Flexible blanket arrays have shown strong promise of scalability toward high power levels due to exceptional packaging efficiency and good mass efficiency, reasons specifically cited in selecting the flexible blanket approach for Milstar.[7] But the

structural effects of scaling these tensioned arrays are currently not well understood by the spacecraft community. The design space has been narrow up to this point in history. All known historically flown rectangular flexible blanket arrays have used a single compression column to react the tension and enforce deployment of either one or two flexible blankets. The downside of this traditional approach is the high cost of the deployable truss and the awkward stowage situation of a cylindrical boom canister joined orthogonally to a rectangular blanket box. Other support structure configurations are possible as have been proposed over the years as will be detailed in the following section. One historical example is a single compression column that reacts as many as 10 separate blankets.[8] More recently a multiple column support approach has been under development by the interest of the United States government.[9,10,11] where a rollable tube column has been suggested rather than a truss. These emerging concepts appear promising but must be compared on the basis of common, quantifiable metrics. Circular form factors have also been proposed as flexible blanket arrays[12,13,14,15], but these are not directly considered in this study.

1.5   Nomenclature

A =   Deployed area, m^2

AR =   Aspect ratio, m/m

a =   Acceleration load as a fraction of Earth's gravity, 9.81 m/s^2

b =   Blanket

bb =   Backbone boom

EA =   Beam axial stiffness, N

EI	$=$	Beam flexural stiffness, Nm^2
GJ	$=$	Beam torsion stiffness, Nm^2
g	$=$	Acceleration due to Earth's gravity, 9.81 m/s^2
I_p	$=$	Polar moment of Inertia, m^4
k	$=$	Spring stiffness, N/m
k_{eq}	$=$	Equivalent spring stiffness, N/m
L	$=$	Length, m
M	$=$	Beam moment due to inertial loading, Nm
m	$=$	Total array mass
m_{pb}	$=$	Primary boom mass, kg
n	$=$	Quantity of primary booms
P	$=$	Axial load, N
P_{cr}	$=$	Critical Euler load, N
pb	$=$	Primary boom
R^2	$=$	Coefficient of determination
r	$=$	Root
S	$=$	Tension per unit width, N/m
sb	$=$	Spreader bar
T	$=$	Tension, N
W	$=$	Array width, m
w	$=$	Primary boom linear mass density, kg/m

β	=	Structural mass fraction, kg/kg
f	=	Fundamental frequency of vibration, Hz
γ	=	Array areal mass density, kg/m^2
δ	=	Frequency knockdown factor, 0.76
ε	=	Areal Power Density, W/m^2
κ	=	Scaling Index, $m^{2.374} / (kg^{0.824}\, s^{0.648})$
κ_l	=	Load Scaling Index, $m^{2.158} / kg^{0.824}$
κ_p	=	Power Scaling Index, $m^{0.864} / (kg^{0.824}\, s^{0.648})$
η	=	Scaling Parameter, $m^{0.374}\, kg^{0.176} / s^{0.648}$
η_r	=	Requirements Scaling Parameter, $1 / (m^{0.274}\, s^{0.648})$
η_a	=	Architecture Scaling Parameter, $m^{0.648}\, kg^{0.176}$
μ	=	Beam efficiency index, $N^{3/5}\, m^{9/5} / kg$
ρ	=	Mass density, kg/m^3
σ	=	Standard deviation

CHAPTER 2.　　SYSTEMS ANALYSIS

This goal of this chapter is to develop an understanding of the bounds of the solar array design and analysis space. Developing practical structural metrics requires a sound understanding of structural architectures throughout time—historical successes, the present state of the art, and the future art of the possible. It also requires an understanding of the interactions of key structural variables through the study of historically developed structural metrics. Analysis of this broad and complex design space is reported in this chapter.

2.1　Structural Metrics

Many structural metrics, structural indices, and performance charts have been developed over the last century to aid in structural design within the aerospace community. Introduction of these tools followed soon after the birth of piloted aircraft in the early 20th century. But it was the voracious demand for lightweight aircraft during World War II that fully inspired the development of structural metrics. These metrics were used to reduce the amount of structural testing required for new aircraft fuselages, skins, spars, and struts.

2.1.1　Early Developments

Herbert Wagner[16] was a prominent German-American rocket scientist who arrived in the United States immediately following World War II; although his broad contributions to aerospace engineering started many years prior. He succinctly described light metal aircraft design as the art of avoiding buckling of struts and sheet metal walls.

But the problem was that at that time, no analytical methods existed to predict the strength of open walled struts and skins. Instead designers relied exclusively on extensive experimentation to find the most mass-efficient spar and skin forms. In response to this laborious task, Wagner published simple metrics for sizing aircraft struts and girders based on minimum mass. He introduced the concept of a structural index in 1928, a quantity referring to a loading term divided by a mass term. The index proved useful for interpolating between experimental results to reveal the most mass efficient structural forms and materials, reducing the number of experiments required to arrive at the optimum design. These indices were based on the law of similarity of the strength of materials, defined by Wager in the following:

The basis for this evaluation is supplied by the law of similarity of the strength of materials. This law says that, with two geometrically similar struts, made of exactly the same material and similarly loaded from a geometric stand-point, all deformations will be geometrically similar and all geometrically corresponding points will be subjected to like stresses, provided the external loads are proportional to the square of the linear dimensions of the struts. This law applies even when the yield point is exceeded.

Fifteen years after Wagner published the structural index, Goodier[17] published a process for developing structural metrics using dimensional analysis, a rigorous process of generating dimensionless scaling coefficients. He specifically addressed the problem

of a square plate that has a central hole being subject to shear loads. He developed

dimensionless quantities that were validated through a series of structural experiments on

plates over a range of sizes. Structural coefficients were proven numerically identical

regardless of plate size. This contribution was useful again for reducing the quantity of

structural testing necessary to optimize the weight of aircraft support structures.

Building on Wagner and Goodier's work, Shanley in 1952[18] published a

comprehensive set of practical relations between allowable stress and a structural index

for aircraft wing ribs, airfoils, and fuselage sections. Shanley, unlike Goodier, did not

implement the strict use of dimensional analysis to arrive at dimensionless coefficients.

Instead he used dimensional similarity principles to develop a structural index to have

units of stress (i.e., force per unit area). For example, the column loading structural index

is the axial load divided by length squared, P/L^2, and for a thin walled tube in bending,

the structural index is the moment load divided by the diameter cubed, M/D^3. The

structural index is typically related to allowable stress graphically.

The principal of the structural index is important because it allows many different

structural members to be compared within a given structural system on the basis of

performance only, independent of the material or proportions by which that member is

constructed. These indices helped aircraft designers to understand the mass penalty paid

for using a non-optimum structural form that may in fact be necessary for practical

reasons.

Shanley's method of strength analysis starts with development of the weight

equation. It is defined by the four fundamental variables affecting the weight of any

structure: the load P, the length of the transmission path L, the material density ρ, and the allowable stress σ. For the case of a beam column under compression, the weight equation is written according to Eq. (1).

$$m = P L \frac{\rho}{\sigma} \tag{1}$$

The critical Euler compressive stress is represented by σ. This method is restricted to evaluating strength only; stiffness must be considered separately.

2.1.2 Structural Components

A quarter century later through the advent of the Space Shuttle and the promise of weekly launches, another push for structural metrics had developed. It was at this time that aircraft design approaches were first adapted for use on large space structures concepts by John Hedgepeth[19] and Martin Mikulas[20].

The adaptation of structural metrics from aircraft to spacecraft was natural since the design parameters are quite similar. Aircraft design is predominantly driven by mass minimization and strength maximization, both material strength and elastic stability. Similarly, stiffness and mass are parameters of especially high concern to spacecraft bus and payload engineers. Strength remains important but mostly for larger structures susceptible to large on-orbit deformations from slewing motions or aggressive thruster firing sequences.

Next, both Mikulas and Murphey developed truss performance metrics that are used for simplified comparison of long, slender, lightly-loaded trusses. Each was

developed into different formulations but both use the same basic assumptions. A comparison of methodologies is provided to follow.

Mikulas[20,21] used weight equations and similarity principles to develop a relation for the allowable bending strength of lightly-loaded, beam-columns. This relation, shown as Eq. (2), is derived using the fundamental principles of bending stress in a thin-walled tube and column buckling strength.

$$\frac{M}{m} = \frac{\pi^2 \sqrt{2}}{2\Sigma} \frac{E}{\rho} \left(\frac{R_1}{L_1}\right)^2 r \tag{2}$$

R_l is the longeron radius of gyration, E is the Elastic Modulus, L_l is the longeron length, M is the applied moment, and ρ is the mass density. This metric is adapted for a truss by adding a parasitic mass factor to account for the additional non-structural mass of diagonals, battens, and joints where $\Sigma = 1.0$ for the ideal case of no parasitic mass and $\Sigma = 4.0$ for the case of a typical deployable space truss where the load-bearing longeron members account for one-fourth the total mass.

The longeron cross section mass is assumed to be uniformly distributed around the truss circumference. Allowable moment is directly related to the column buckling limit load of a single longeron located along the line of maximum compressive stress for a truss subjected to the said bending moment. It is assumed that as the truss scales in diameter, the longeron length scales proportionally so as to maintain a fixed longeron slenderness ratio, longeron length divided by longeron diameter, of 100.

In similar fashion Murphey[22] developed two boom indices for the two most common loading scenarios: beam (i.e., bending) loading and column loading. The higher

the indicial value for a given truss design, the more mass efficient that truss. The indices for column and bending loads are listed as Eqs. (3) and (4) respectively.

$$\mu_c = \frac{(LP)^{2/3}}{w} \tag{3}$$

$$\mu = \frac{(M^2EI)^{1/5}}{w} \tag{4}$$

The bending index, Eq. (4), will be used extensively in the analytical modeling to follow in later chapters.

This approach allows comparison of truss performance without knowledge of detailed truss construction or even the materials used. The benefit of these indices is they capture the strength, stiffness, and weight performance of a truss using testable boom properties: critical bending moment M, flexural stiffness EI, linear density w, length L, and critical Euler buckling load P. This allows many different boom types to be objectively compared on an even playing field despite drastic design differences.

The beam index assumes that the truss failure mode is longeron buckling. It also assumes that the truss behaves like an Euler-Bernoulli beam where plane cross-sections remain plane during bending. Also the stiffness of battens and diagonals can be neglected because these elements are very lightly stressed during bending and column loading.

The differences between Mikulas' and Murphey's approaches are subtle. Mikulas chose to hold longeron slenderness ratio constant; therefore as truss bay length and diameter grow, the diagonal angle must change. Thus the truss radius of gyration is defined by bay length and cannot be scaled independently.

Murphey on the other hand chose to hold truss diagonal angle constant while treating the longeron radius of gyration as an independent variable. Similar to Mikulas he assumes the longeron is always adequately slender in order to maintain to the Euler buckling failure mode. But as the truss radius grows, the longeron length grows proportionally to hold diagonal angle constant. Similarly, as the number of longerons grows, longeron length decreases proportionally to maintain constant diagonal angle. This enables independent scaling of longeron length and radius of gyration enabling direct comparison of different longeron hierarchy from a solid rod to a tube to a truss. This treatment of truss strength[22,23] is based on the following review that will be derived into an expression of similar form to Mikulas' for a direct comparison.

One underlying assumption is that the truss geometric center is always coincident with the neutral axis regardless of the number of longerons. This assumption shows that the flexural stiffness of the truss is equivalent to the axial stiffness contribution of each longeron. Each longeron is therefore treated as a fraction of the cross-section area of a thin-walled tube according to Eq. (5).

$$EI = \sum_{i=1}^{n} EA_l x_i^2 = EA_l r^2 \sum_{i=1}^{n} \cos^2\left(\psi_1 + \frac{2\pi}{n}(i-1)\right) = \frac{n}{2} EA_l r^2 \qquad (5)$$

The area term, A_l, refers to each longeron cross-section; the quantity of longerons is given by n; and the truss cross-section radius is given by r. The distance from the truss geometric center to a specific longeron is further defined by Eq. (6).

$$x_i = r \cos \psi_i \qquad (6)$$

Beam flexural stiffness is commonly defined as the applied moment divided by the resulting beam curvature κ, shown by Eq. (7).

18

$$EI = \frac{M}{\kappa} \tag{7}$$

Combining Eq. (5) with (7) produces Eq. (8), the moment curvature relationship for a truss.

$$\frac{M}{\kappa} = \frac{n}{2} EA_l r^2 \tag{8}$$

Assuming the longeron elements are pinned at both ends such that they only carry axial loads, the load in a single longeron is related to the longeron strain, ε_l, as defined by Eq. (9).

$$P_l = \varepsilon_l EA_l \tag{9}$$

The longeron strain can also be expressed in terms of truss curvature by Eq. (10) where ϑ is the circumferential angle of the longeron with respect to the bend axis. The desired direction of bending load is applied such that maximum deformation occurs perpendicular to one of the truss faces.

$$\varepsilon_l = \kappa r \sin \theta \tag{10}$$

By combining Eqs. (8), (9), and (10) the truss bending moment can be expressed by Eq. (11) in terms of the truss radius, longeron axial load, number of longerons, and angle of the furthest most longeron from the bending axis.

$$M = \frac{rP_l n}{2 \sin \theta} \tag{11}$$

If the truss failure mode is assumed to be longeron buckling then Eq.(11) can be expanded into Eq.(12).

$$M = \frac{rn}{2\sin\theta}\frac{\pi^2 EI_l}{L_l^2} \qquad (12)$$

The radius of gyration of the longeron is defined by Eq. (13) where I is defined as the area moment of inertia.

$$R_l^2 = \frac{I_l}{A_l} \qquad (13)$$

The axial material fraction β of the truss is defined by Eq. (14) as the ratio of longeron cross section area to the total effective cross section area of the truss including battens and diagonals,

$$\beta = \frac{nA_l}{A} \qquad (14)$$

The linear density of the truss is then expressed in terms of longeron cross section area and material density through Eq. (15).

$$w = \frac{m}{L} = \rho A = \rho\frac{nA_l}{\beta} \qquad (15)$$

Eqs. (12), (13), (14), and (15) are combined into Eq. (16) to express the truss moment in terms of truss radius, number of longerons, and longeron cross-section geometry.

$$\frac{M}{w} = \frac{\beta\pi^2}{2\sin\theta}\frac{E}{\rho}\left(\frac{R_l}{L_l}\right)^2 r \qquad (16)$$

When the methods of Murphey in Eq. (16) are compared to those by Mikulas in Eq. (2), the equations are nearly identical. The only two differences are that Eq. (16) includes an axial material fraction term and a term for the angle of the bend axis with respect to the longerons. Whereas Eq. (2) accounts for the material fraction with an

20

equivalent inverse term in the denominator, Σ, and the longeron angle is assumed fixed at 45 degrees as represented by the $\sqrt{2}$ term in place of $\sin \vartheta$ although, curiously, the angle term is inversed.

Weight-strength metrics have been developed for other structural components as well. In the 1970's Williams[24] presented metrics for rib stiffened compression panels and cylinders. In the 1960's Anderson[25] developed metrics for Aerodynamic decelerators. In both cases, the metrics were reduced to a weight parameter with units of force per length cubed and a loading parameter with units of force per length squared, equivalent to the units of stress.

2.1.3 Planar Structural Systems

More recently, Mikulas built on the beam index from Eq. (2) to develop a loading parameter that relates solar array structural requirements to beam design parameters. The solar array is treated as a single optimized composite tube with a distributed mass to represent the tensioned photovoltaic blanket. It is shown that growth of the solar array loading parameter is related to the growth of the structural mass fraction. Mikulas defines structural mass fraction as the ratio of column mass to blanket mass. The loading parameter defined by Eq. (17) quantifies the mass penalty of increasing solar array structural requirements: length, acceleration load, and the fundamental frequency of vibration (printed with the written permission of Dr. Martin Mikulas).

$$\frac{m_{structure}}{m_{blanket}} \sim L^2 \left(\frac{af}{m_{blanket}} \right)^{2/5} \tag{17}$$

As the loading parameter grows, the structural mass fraction grows proportionally by necessity. As is evident by this relation, growth in array length is especially detrimental to mass efficiency when compared to growth in acceleration loading or the fundamental frequency requirement.

A similar approach was developed by Murphey[22] using his beam efficiency index previously defined by Eq. (4). Again, a single beam column is the structural basis, and a distributed mass along the beam is used to represent the blanket. Rather than sizing a specific composite tube as the benchmark of beam performance, the beam is characterized generically by the beam efficiency index. As defined earlier, this term quantifies the relationship between truss bending strength, flexural stiffness, and mass per length in terms of testable performance parameters. It is not necessary to know the truss construction details.

Originally developed for trusses, this index is also useful for comparing other slender beam column architectures such as rollable tubes. The loading equations are based on thin-walled tube behavior that neglect shear stiffness effects.

From this index, it is shown that growth in solar array length, frequency, and strength requirements require a beam with a larger index value, similar to how Eq. (17) shows a necessary growth in structural mass fraction to accommodate growth of the loading parameter.

Both of these previous approaches are limited to a single beam with the blanket mass distributed along the beam length. The approach proposed in the present study is

differentiated from these previous approaches in that the solar array structural *system* is considered rather than just a single beam *component*. The system approach accounts for the dynamic interaction and mass scaling of multiple beams and blankets.

The advantage of addressing the problem from the system level is that the results become more relevant for a broader range of solar array architectures, namely those that are substantially rectangular in deployed geometry rather than just rectilinear. The disadvantage is that more structural terms are needed adding analytic complexity and potentially confusing the usability of the results.

2.2 Flexible-Blanket Solar Array Structural Architectures

Many different tensioned blanket support structure concepts have been proposed over the last four decades. They each fit into one of four structural architecture categories: radial, rectangular segmented, rectangular coupled, or rectangular grillage. Understanding how the various components of the system fit and function together is a necessary prelude to structural analysis of the system.

The first radial architecture was patented by Kaplan[26] in 1977 as shown in Figure 3. Radial lines extending from a central drum are tensioned by a concentrated compression hoop column structure. Deployment is enforced by torsion spring elements located at several hinge locations on the hoop rim. Rate is controlled by a motor that unfurls the radial tension lines. Deployed strength is ensured by the structural depth of alternating top to bottom drum attachment location of each radial tension line. Blankets are unfurled from the drum synchronously with the tension lines, one blanket gore for each rim segment.
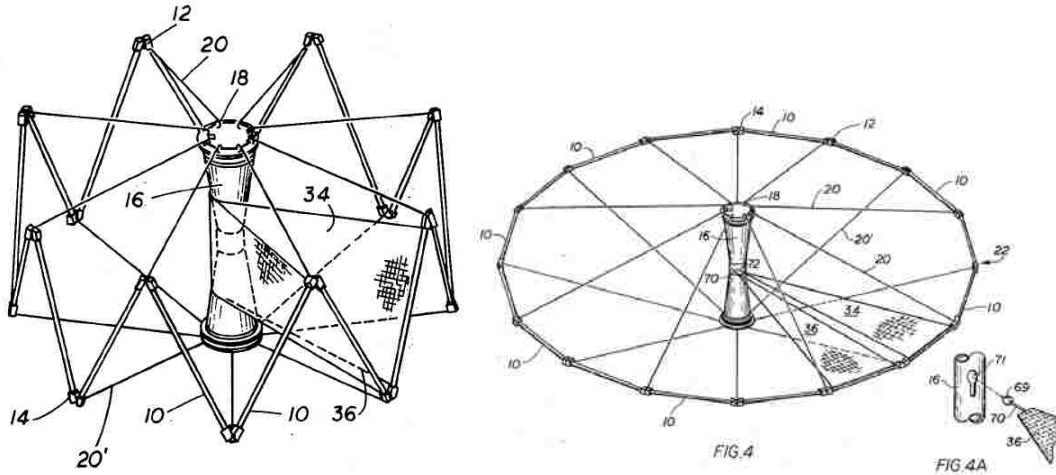
Figure 3. Patent 4,030,102 by Kaplan.

This Kaplan invented concept was further developed by Crawford[27] and eventually designated the Astro Spoked Wheel Array (that would later also be known also as the ATK HexWheel). A one megawatt version was conceptually sized to fit in the Space Shuttle payload bay at a deployed diameter of 109 meters, a mass of 6100 kg, and an estimated fundamental frequency of 0.063 Hz. The gore tension was approximated as a single string with variable mass per radial length given according to the gore mass, *m*, rim segment length, *L*, and gore area, *A*, by Eq. (18).

$$w = \frac{ml}{A} \tag{18}$$

Fundamental frequency of the gore was approximated in Eq. (19) as a string according to the total gore tension, *T*, mass per radial length, *w*, and total radial arm length, *x*.

$$f = \sqrt{\frac{T}{2wx^2}} \qquad (19)$$

Compression in the rim was approximated by assuming the hoop is circular and that each radial tension line carries half the gore blanket tension. The radial arm compression load, P, is related to the number of gores, n, through Eq. (20).

$$P = \frac{Tn}{\pi} \qquad (20)$$

The partially stowed and deployed views of the Spoked Wheel Array are shown by Figure 4.
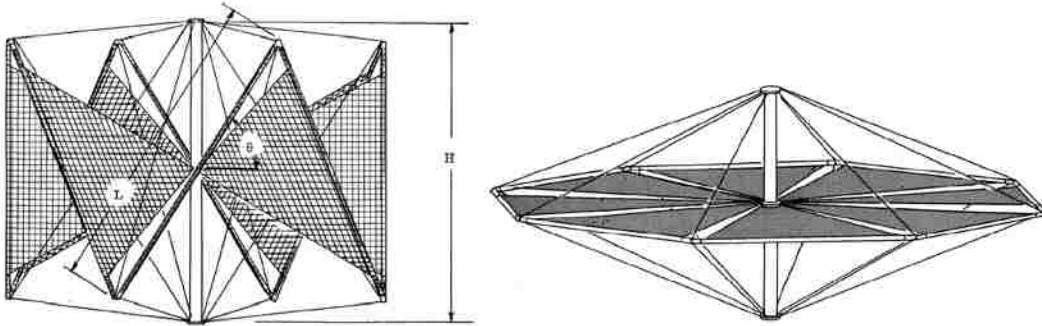
Figure 4. Astro Spoked Wheel Array partially stowed and deployed

Another radial architecture commonly known as the UltraFlex Array from AEC-ABLE (ATK) was first patented by Harvey[28] in 1994. Instead of a hoop column reaction structure with guy-wires, this architecture uses radial (intermediate) spars to react gore tension. These intermediate spars are intentionally deflected out of plane cup-up to provide tension to the gores. Each gore, surrounded by two intermediate spars, has a mid-gore flexure hinge that is pre-creased into the stowed configuration to generate circumferential tension. Deployment is actuated by driving rotation of a hub around a fixed axle. The lead spar, labeled as 21 in Figure 5, is connected to the rotating hub and

thus leads the circumferential deployment motion, intermediate spars and gores follow. The root spar connects the spacecraft bus to the fixed axel. At full deployment the lead spar is connected to a honeycomb plate to provide reaction for gore preload. Polyimide foam is used between gores to control preload when stowed.
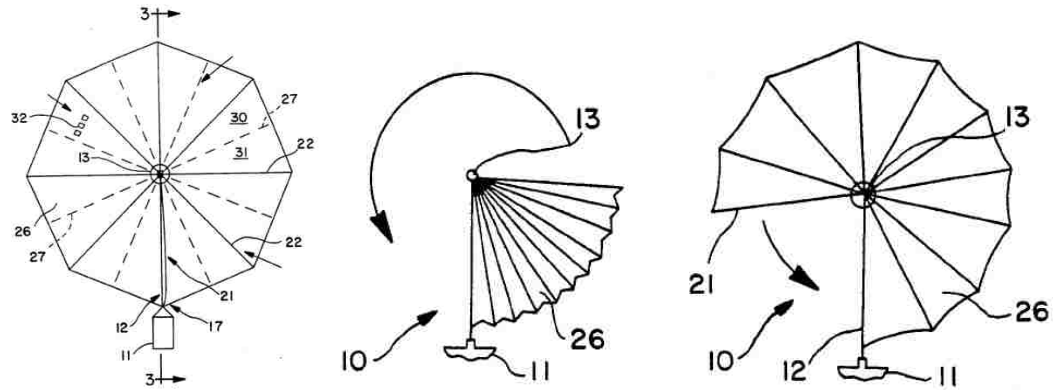
Figure 5. UltraFlex patent 5,296,044 by Harvey is shown deployed and in two partially deployed states.

In 2009, an application was filed by White[29] that reveals a new embodiment of the UltraFlex Array. This new embodiment is known as MegaFlex[30]. Among other new details, the primary changes include a secondary fold of the root spar and a secondary fold of the gores for the purpose of increased packaging efficiency over the UltraFlex concept. The secondary root spar articulation is evident from Figure 6.

Structural depth is incorporated by spar support struts shown in Figure 7. These struts, labeled as 190 in the figure, are secured to the intermediate spars at one-third the distance from the hub. A circumferential cable, labeled as 193 in the figure, connects these support struts for even greater deployed stiffness and strength.
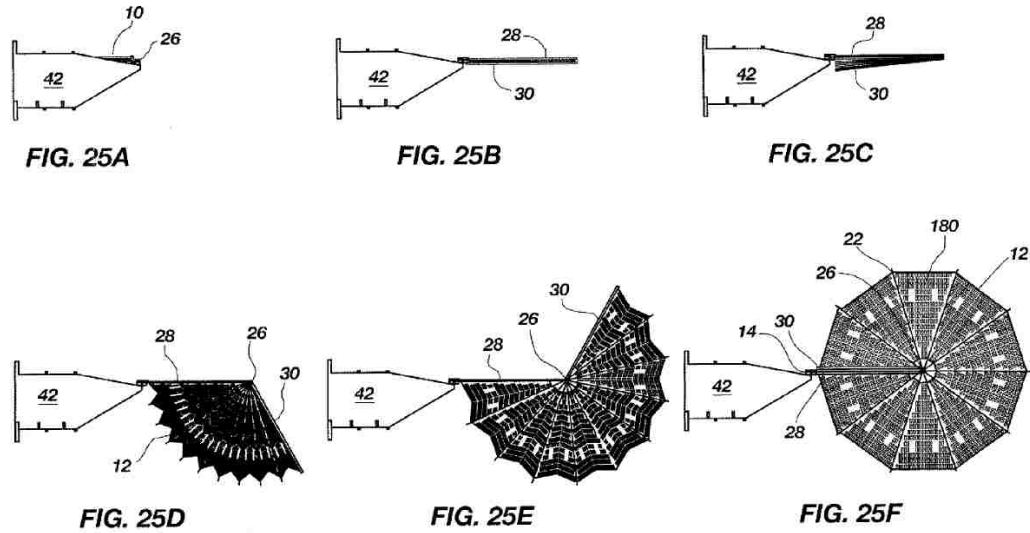
Figure 6. Deployment stages of application 11/944061 show a secondary articulation of the root spar in 25B.
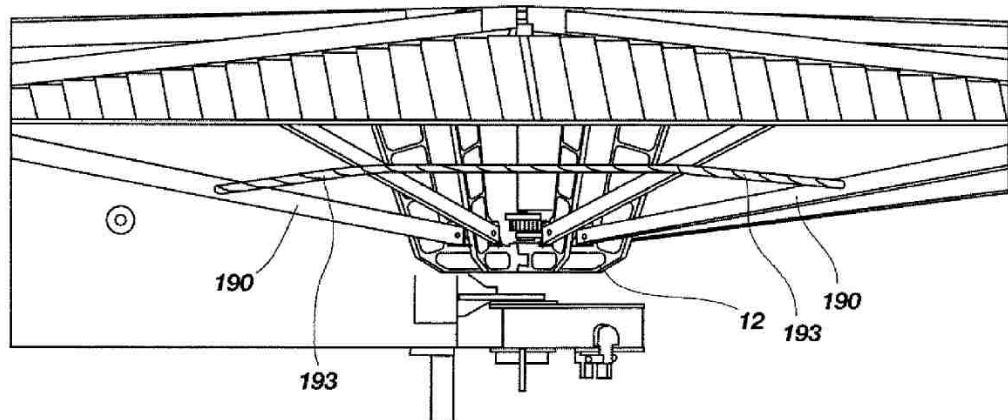
Figure 7. Patent application 11/944061 shows spar support struts, 190, and a circumferential cable, 193.

Rectangular segmented is by far the most common tensioned blanket array type in use today. Rectangular coupled is very similar to segmented except the blankets are joined at the tip by a continuous spreader bar and thus are synchronously deployed rather than sequentially deployed.

The first recorded rectangular array concept was a coupled system prototyped in 1972. A spreader bar was used to transfer tension loads from 10 separate blankets to a single compression column. This concept was conceived to deploy a 10,000 ft^2 blanket area. The deployment test article showing half of the blankets is illustrated in Figure 8.[8]
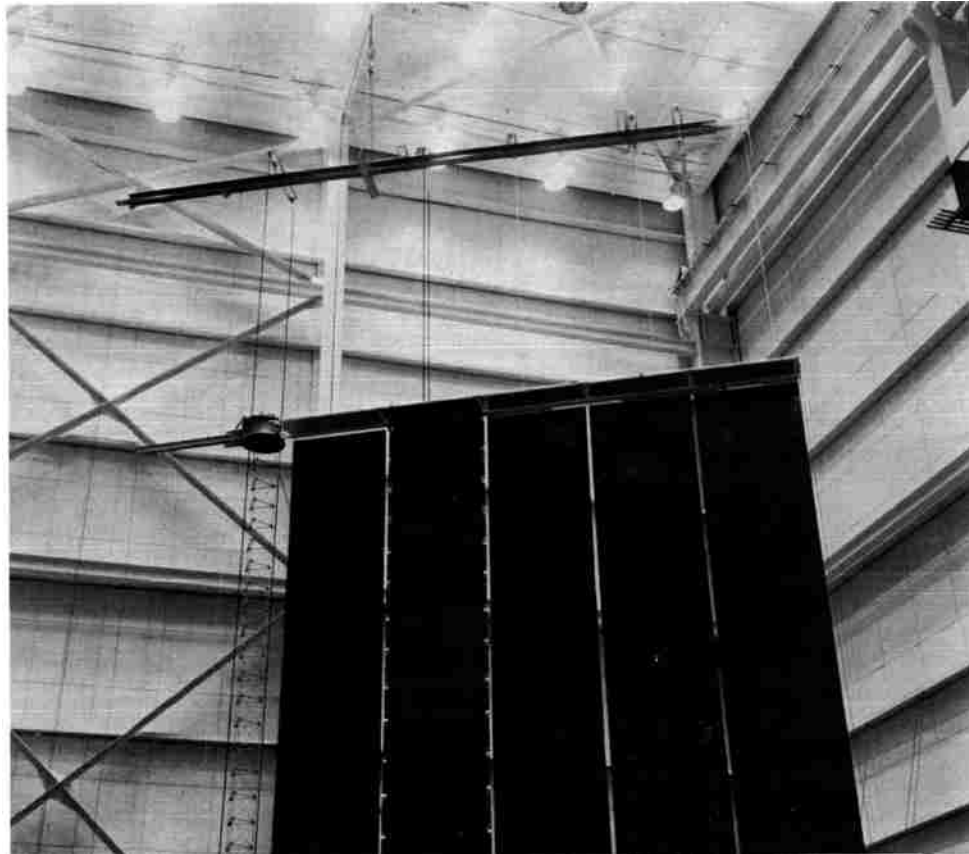
Figure 8. Deployment concept for a 10,000 ft^2 rectangular coupled concept from 1972.

In 1983, Rauschenbach[31] from TRW, Inc., patented one of the most common of rectangular segmented types known as the Advanced Photovoltaic Solar Array (APSA). This concept uses a central compression column, most commonly the continuous longeron lattice truss, to support an accordion folded blanket. The blanket structure is composed of rib-stiffened panels connected by elastic hinge elements that are strain free in the stowed state and strained in the deployed state. This concept was developed into a

prototype using JPL funding that became the foundational technology upon which many other accordion folded solar arrays were based over the past 30 years. The baseline APSA[32] was sized to be 15.25 meters long by 2.81 meters wide. This design later morphed into the array used on the NASA Terra EOS-AM[33] climate monitoring spacecraft launched in 1999. This array was deployed to 8.5 meters long by 4.9 meters wide.

The Europeans also adopted this TRW developed architecture on the Olympus-F1 (i.e., L-SAT-1)[34] experimental telecommunications satellite launched in 1989. Each of two wings spans were 11 meters long and 5.5 meters wide.

While the APSA was certainly foundational for maturing necessary technology elements, there was another array that was the first to demonstrate the tensioned blanket compression column concept. In 1984 the Solar Array Flight Experiment (SAFE)[35] deployed a Lockheed Martin developed FlexArray from the Space Shuttle Discovery cargo bay to a length of 32 meters and width of 4 meters on the STS-41D mission. Following this experiment, eight wings (16 blankets) were used on the International Space Station, each stretching 35 meters long and 11.6 meters wide.[64] Another version of this array was used on the United States Air Force communications satellite constellation Milstar first launched in 1994[7]. Each wing stretched 15.2 meters long and 3.0 meters wide.

APSA, SAFE, ISS, Milstar, EOS-AM, and Olympus all use a single continuous longeron lattice truss for primary deployment and structural support. Other deployment and support methods have been proposed for rectangular segmented arrays including the

scissor pantograph, accordion folded truss, rollable slit tube, rollable Bi-STEM, and a guy-wire stabilized STEM. Each of these approaches is described in detail to follow.

In 1999 Benton[36] patented a method to deploy and support an accordion folded blanket with a spring-loaded sliding friction scissor pantograph. The invention is shown in Figure 9 in the partially deployed state. Three years later, Murphy[37] patented a similar but improved version known by ATK Space Systems as Aurora. The accordion folded blanket is supported using a spring-loaded scissor pantograph attached to the tip and base plates. Deployment is enforced by tension springs attached to cables tied between opposing outer links, extending the pantograph by drawing the links together. Kicker springs are included in the central links to force initial deployment motion. Deployment rate is controlled by a pair of lanyards connecting the tip and base plates. The lanyards pass through eyelets on the blanket and are wound around a rotational damper at the root. Deployment binding is prevented by the secondary links at the base and tip plates labeled as 26 and 27 in Figure 10. A flexible harness is included on the lengthwise perimeter. Blanket preload in the stowed state is enforced by foam buttons attached to each blanket facet. To manage thermal expansion, contraction, and deployment impulses, a set of thin flexible spines are continuously attached to the full length of the blanket. These spines are joined to the tip and base plates through constant force Neg'ator springs.
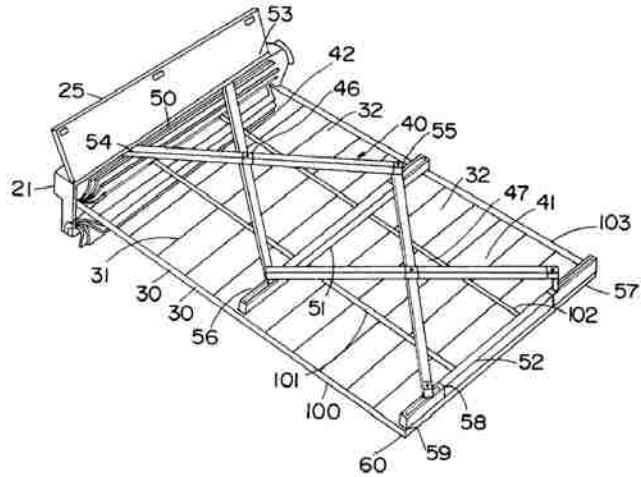
Figure 9. Patent 5,961,738 by Benton.
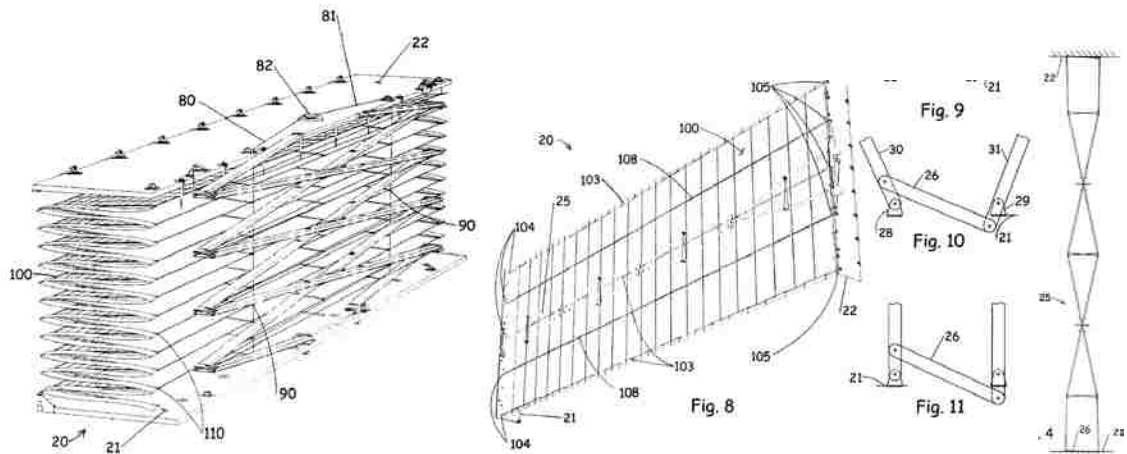
Figure 10. Patent 6,423,895 by Murphy.

In 2009 a patent application was filed by Murphey[38] for an accordion folded solar array blanket deployed and supported with an accordion folded compression column truss[39]. Because the column neutral axis lies coincident with the blanket tension axis, the column is required only to carry pure compression loads with no eccentricity. Deployment is enforced through the release of strain energy in the concentrated strain hinges of the accordion folded truss. This concept is readily scaled to a rectangular

coupled architecture by adding an additional accordion articulation of the blanket boxes.

Figure 10 illustrates both the segmented and coupled manifestations of this concept.
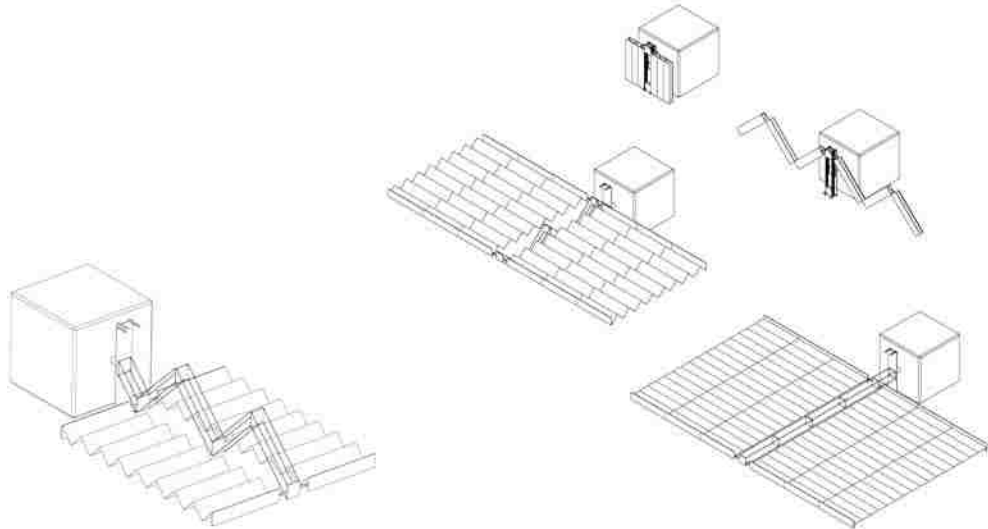
Figure 11. Patent application 12/55012 by Murphey shows both segmented and coupled array forms.

Another type of rectangular segmented solar array was patented by Beidleman[40] in 2010. This architecture known as RAPDAR is defined as having a tensioned blanket that is supported by two slit-tube (i.e., open section thin-walled tube) longerons connected to the root and the tip spreader bars and separated with multiple spreader bars along the boom length. Deployment is enforced by a shape memory effect inherent to one of the fiber reinforced polymer plies. As the rolled (i.e, stowed) boom is heated, the polymer in the exposed region softens allowing the other fully rigid composite plies to force the boom to recover the as-fabricated deployed shape. This architecture also works with bi-stable slit-tubes, those that have two elastically stable states, rolled and deployed. Figure 12 shows the stowed and deployed states of RAPDAR along with a close-up of the connection between the slit-tube and a batten.

32
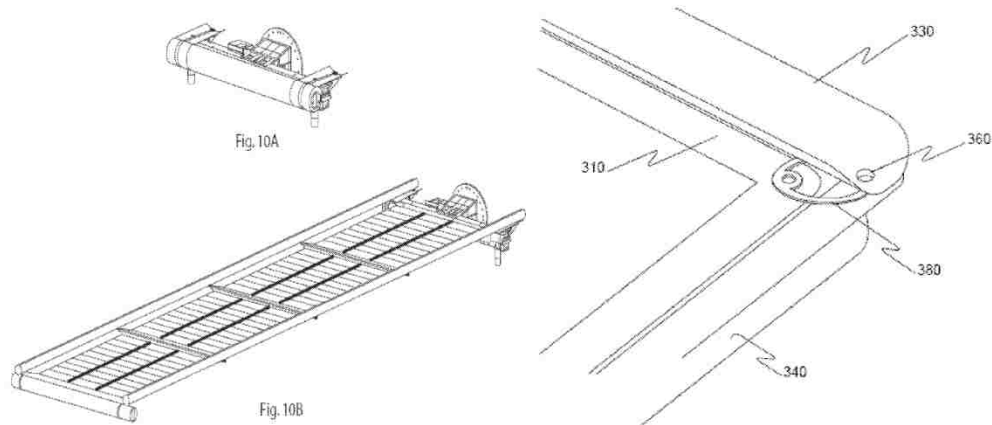
Figure 12. Patent 7,806,370 by Beidleman.

RAPDAR is not the first concept to use the roll-out boom and blanket approach. The Hubble telescope solar arrays, Flexible Rolled-Up Solar Array (FRUSA)[41], were the first to implement the roll-out approach. FRUSA is supported by a pair of stainless steel Bi-STEM booms (two nested Storable Tubular Extendible Members) attached to a tip spreader bar and a root spar tube. Two blankets and two pairs of Bi-STEM booms synchronously unfurl from the spar tube in opposite directions by a motor drive. An embossed cushion is rolled with the blanket to provide preload for launch loads. During deployment the cushion is separated from the blanket and furled around a secondary drum shown in Figure 13. Each of the two nested Bi-STEM elements is a 6.4 cm diameter, 0.13 mm thick tube with a 30° slit opening oriented 180° from each other.
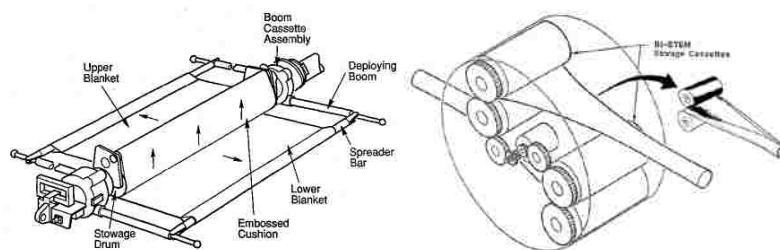
Figure 13. The FRUSA array is shown partially deployed alongside an illustration of the Bi-STEM booms used to deploy and support the blanket.

33

Although few details have been made public to date, others have been actively developing a roll-out solar array concept. In 2010 Deployable Space Systems was awarded an Air Force contract to develop the ultra-lightweight elastically Self-Deployable Roll-Out Solar Array (ROSA)[42] for ultra-thin multijunction photovoltaic blankets and has since developed the concept for other U.S. Government agencies[10].

Yet another rectangular segmented architecture was patented by Stribling[43] in 2006. This patented concept known as the Boeing High Power Solar Array (HPSA) uses either a rolled or an accordion folded blanket. This blanket is supported by a pair of STEM booms attached to a tip spreader bar and to the array root. The booms (i.e., bow beams) are intentionally buckled so as to provide a constant tension force to the blanket and to a pair of guy-wires, one end attached to the boom tips and the other to the tip of a pair of tether beams. This guy-wire approach adds structural depth to the system improving strength and stiffness. Figure 14 shows a partially stowed array with the STEM booms, guy-wires, and tether beams.

In a later publication by Stribling[44], additional design refinements are described through a graphic shown as Figure 15. Notice from this figure the critical nature of the force balance between the bow beam critical load, the tether tension, and constant force springs used to tension the blanket. Other bow beam architectures are suggested such as a carbon fiber reinforced plastic (CFRP) STEM rather than the stainless STEM described in the patent.
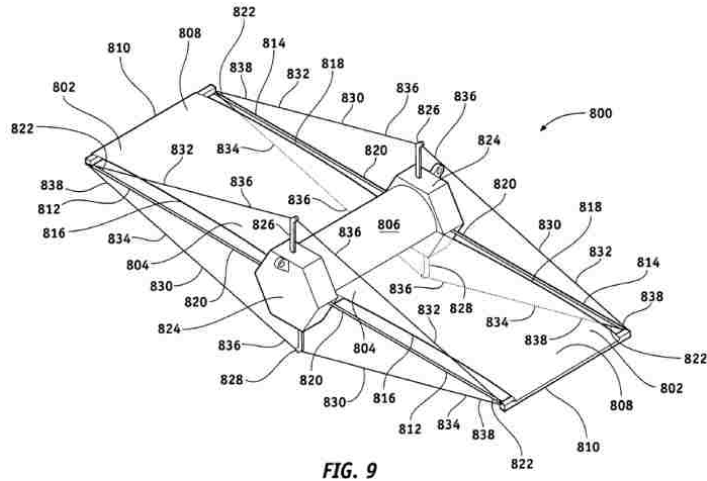
Figure 14. Patent 6,983,914 of the HPSA array uses guy-wires for structural depth.
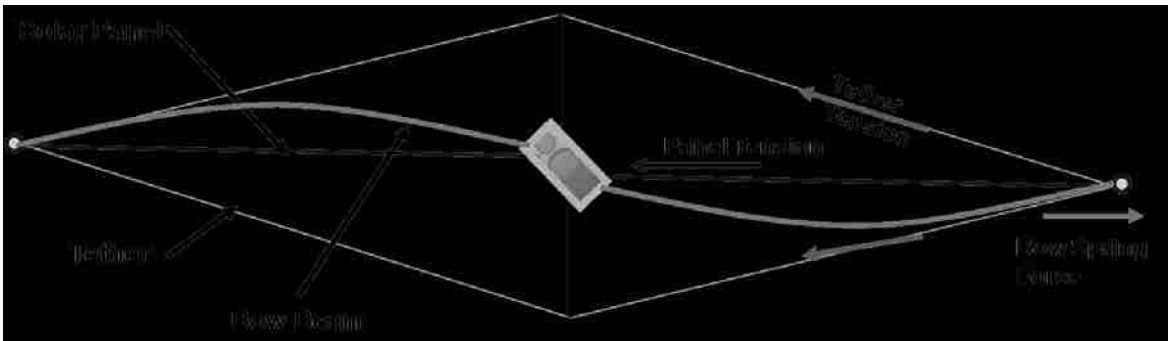
Figure 15. The restoring force of the buckled bow beam generates blanket and tether tension.

The fourth and last tensioned blanket support structure category is the rectangular grillage (i.e., tiled network of repeating bays of frame members), the least common of the four forms. Two types of grillage structures have been proposed, those that use hexagonal bays and those that use rectangular. Both can be engineered to fold into a bundle of struts, but rectangular bays have been preferred in every case thus far because of the direct load path across the bays and the ease of constructing rectangular blankets versus hexagonal.

In 2007, Murphy[45] patented the AEC-Able Engineering SquareRigger architecture. The support method is a grillage of rectangular bays of 2:1 aspect ratio.

35

Within each bay is an accordion or roll stowed blanket tensioned between the two opposing short struts. Six struts of equal length are used for each bay with the cross section preferably rectangular of dimensions 4 to 10 centimeters by 2 to 5 centimeters. Deployment method is a synchronous rotation of hinge pin joints located at the corner of each bay and at the mid-point of each bay length. Deployment is enforced by a motor located at alternating corner hinge tables. In addition to driving the strut rotations, each motor spool has four cables attached with the opposing cable ends attached to two blankets, one cable at each of the free corners of the two blankets. As the motors deploy the hinges, the cables are furled around the motor drum. Then once the strut hinges have been locked out, the motor is reversed to unfurl the cable and thus hoist a pair of blankets into their respective bays.

Figure 14 shows the synchronous deployment of two twelve-bay wings. The figure also shows a close-up of one hinge table including the tapes (118) used to synchronize deployment of the struts. Lastly, the figure shows a cross-section of one stowed bay where the blanket (34) nests inside the six folded struts (22 and 24).
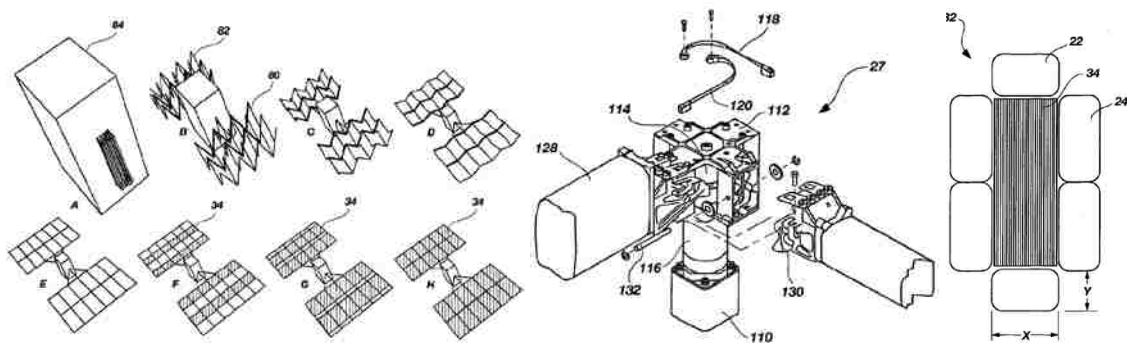
Figure 16. The SquareRigger architecture synchronously deploys dozens of struts into a rectangular grillage of bays filled with tensioned blankets.

2.3   Structural Architecture Categories

Based on the previous historical survey, flexible blanket solar arrays may be categorized according to four distinctly different structural architecture categories:

1.   Rectangular segmented

2.   Rectangular coupled

3.   Rectangular grillage

4.   Radial

Each of these architectures is characterized by the following design terms: (a) area, (b) number of segments, (c) segment length, and (d) segment width. Each of these terms is defined slightly differently for each of the array forms. Yet each array form has the same four basic structural components: (a) primary boom, (b) spreader bar, backbone boom, and (c) flexible blanket. Figure 17 labels the defining characteristics of each array architecture category.

Each of these three structural components is defined by a list of design parameters. Some parameters are defined through assumption of industry practice, and others are derived through expression. The focus of the work herein is the rectangular segmented and the rectangular coupled architectures. The rectangular grillage and radial architectures will not be considered.
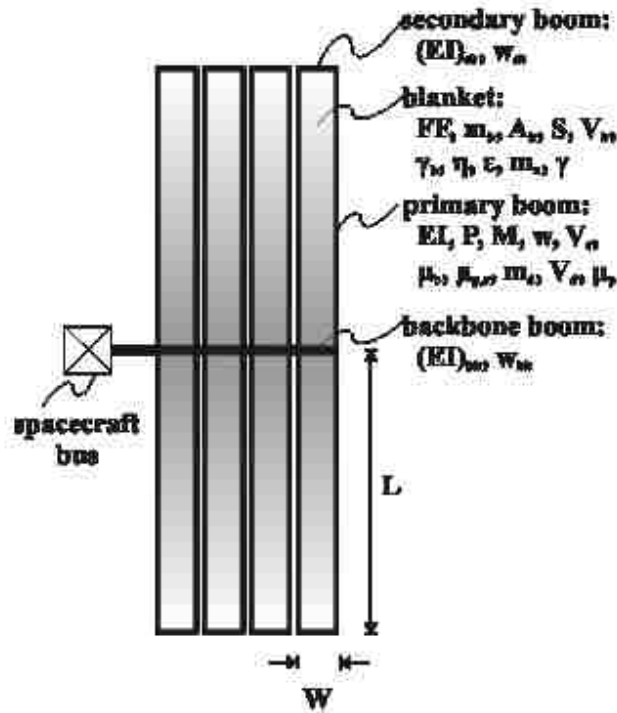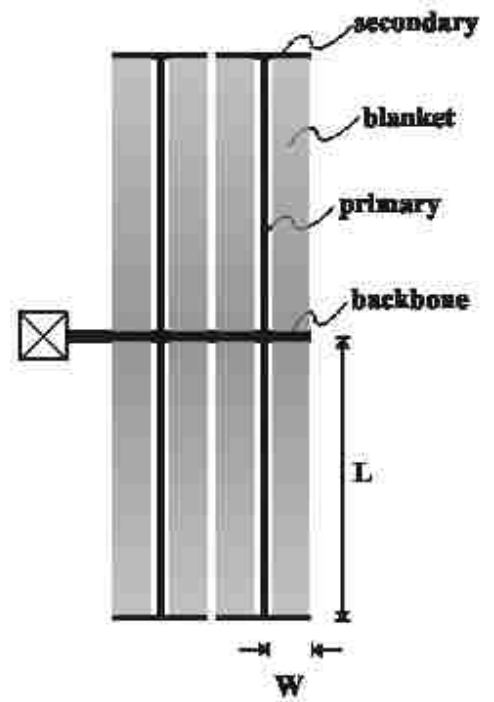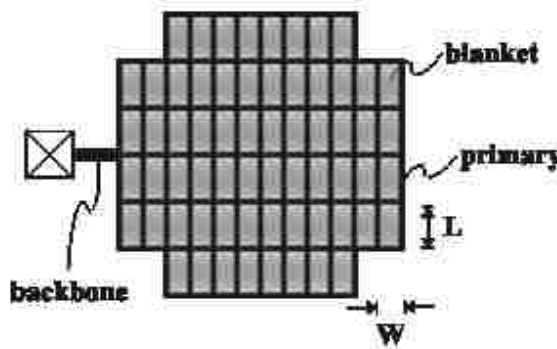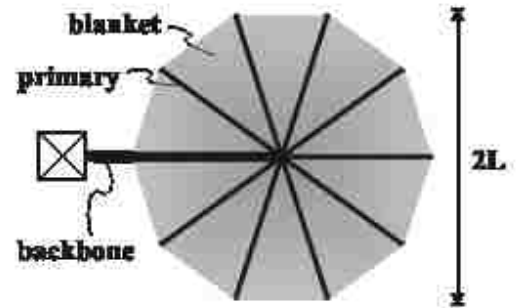
Figure 17.   Each array architecture is described by a set of common variables.

2.4   Deployable Boom Performance

For each of the solar array architectures illustrated in the previous section, a range of deployable boom types is available. The structural efficiency of a given boom type is directly tied to the structural hierarchy by which that boom is constructed. Figure 18

illustrates the growth in boom hierarchy from a solid rod to a truss of tubes. As structural hierarchy grows, the strength and stiffness performance grows for a given mass (i.e., structural efficiency). But the mass savings of increased hierarchy always comes at a cost—these booms are usually more complex to construct and they package into larger volumes when folded.

Increasing structural efficiency
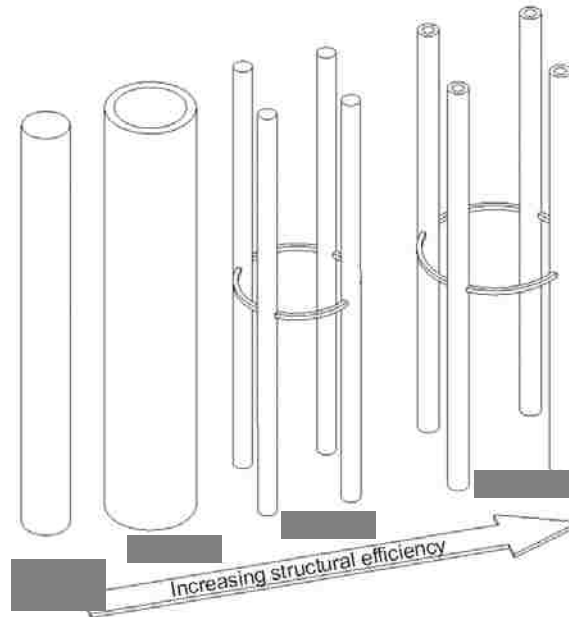
Figure 18. Illustration of boom hierarchy, (a) solid rod, (b) tube, (c) truss of rod longerons, (d) truss of tube longerons.

A survey of heritage and prototype deployable trusses is provided in Table 1. On the last row, the beam performance index is listed. These performance values were collected and published previously by Murphey[22].

A class of boom not included in this table is the collapsible tube. This class is generally lower in structural efficiency than a truss but tends to be simpler in construction and smaller in packaged volume. This type includes the Storable Tubular Extendible Member (STEM)[46,47], the Collapsible Tube Member (CTM)[48,49,50] also known as the

Lenticular, and the Triangular Rollable And Collapsible (TRAC)[51,52] mast. The cross-section shapes of these boom types are shown in Figure 4 in the two states: flattened and deployed.
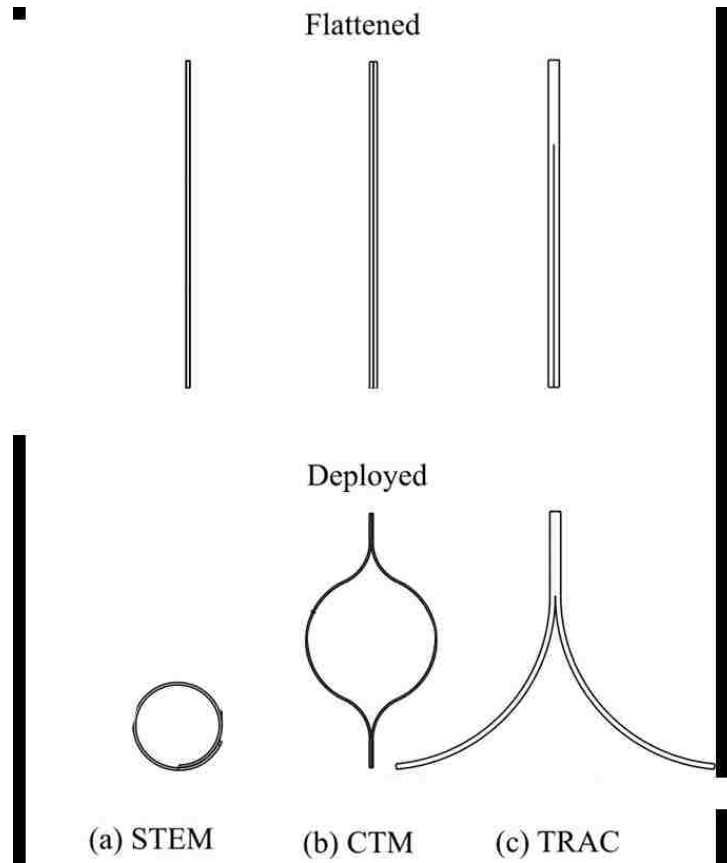
Figure 19. Collapsible tube boom types shown collapsed and deployed (expanded).

Table 1. *Truss parameters either measured (m), derived through analysis (a) or determined by inspection (i).*

	AFRL DECS-MAR	L' Garde SSP Truss	ATK-ABLE S2 Coil-able	ATK-ABLE GR1 Coil-able	ATK-ABLE GR2 Coil-able	ATK-ABLE SRTM	ATK-Tri-Lok™ GS2	ILC Dover Ultra-Boom De-ployed	ILC Dover Ultra-Boom Pris-tine	Foster-Miller Tubu-lar Truss	Foster-Miller Slit Tape Truss	Foster-Miller Boom Iso-grid
Bending stiffness (Nm^2), EI	99,200 a	1.536E6 m	0.100E6 m	81,352 m	11,162 m	15.78E6 m	1.202E6 a/m	11,740 m	6,505 m	4,588 m	36,724 m	5,835 a
Bending strength (Nm), M	289.0 a	1,087 a	270.2 m	48.6 m	10.6 m	6,525 m	383.0 a/m	63.6 m	19.4 m	3.50 m	18.30 m	0.95 m
Axial Stiffness (N), EA	10.3E6 a	6.584E6 m	5.19E6 m	4.20E6 m	1.55E6 m	94.3E6 m	9.34E6 a/m	2.89E6 m	1.43E6 m	0.457E6 m	1.84E6 m	0.461E6 a
Axial strength (N), P	2,493 a	2,473 a	2,745 m	494 m	176 m	23,290m	1,308 a/m	1,413 m	431.2 m	60.0 m	155.0 m	12.0 m
Column length (m), L	19.82 a	78.28 a	19.01 a	40.30 a	25.02 a	81.78 a	95.25 a	9.06 a	12.20 a	27.47 a	48.36 a	69.28 a
Mass per length (kg/m), w	0.1570 a	0.700 m	0.420 m	0.070 m	0.0318 m	5.232 m	0.140 a/m	0.1445 m	0.0655 m	0.0475 m	0.0577 m	0.023 m
Number of lonergons, n	3 a	3 i	3 i	3 i	3 i	4 i	3 i	16 i	16 i	3 i	3 i	18 i
Truss radius (m), R	0.1476 a	0.680 m	0.197 m	0.197 m	0.120 m	0.560 m	0.500 a/m	0.090 m	0.090 m	0.175 m	0.200 m	0.159 m
Diagonal angle (deg), θ	38.48 a	56.00 m	33.80 m	33.80 m	33.80 m	41.91 m	45.00 a/m	30.00 m	30.00 m	58.90 m	45.00 m	30.00 m
Material density (kg/m^3), ρ	1,600 a	1,661 m	2,020 m	1,605 m	1,605 m	1,633 m	1,661 m	1,462 m	1,462 m	1,522 m	1,522 m	1,567 a
Material modulus (GPa), E	165.0 a	65.8 m	51.7 m	188 m	188 m	165.5 m	172.4 m	143.1 m	143.1 m	86.2 m	136.0 m	140.2 a
μ_b, N$^{3/5}$m$^{9/5}$/kg	613	404	224	648	521	177	1,268	237	290	187	454	242

2.5   Photovoltaic Blanket Performance

The primary function of a photovoltaic solar array is not simply to support a large flexible blanket. The blanket must, of course, be populated with photovoltaic cells capable of converting solar radiation into an electrical current and passing that current back to the spacecraft bus. From the perspective of structural scaling, only the blanket mass and area is of concern. However it is eventually necessary to relate deployed area to the actual power produced. Table 2 provides the necessary information for this conversion. Flexible blanket areal mass densities and areal power densities are listed for the current state of practice in photovoltaic cell power conversion efficiencies as well as anticipated future advancements in multi-junction technologies.

The current state of practice areal power density is represented by a 29.5% efficient triple-junction cell between the range of 250 to 280 W/m^2. The exact value within this range depends on cell manufacturer, size, cell laydown spacing, and blanket harness voltage. These cell conversion values represent the beginning of mission life and the low-earth-orbit solar spectrum parameters of 28°C Air Mass Zero (AM0).

Blanket area and mass values are also documented in the table. The mass includes the substrate, cell modules, and harnessing, but does not include any non-functioning area consumed by the deployment structure such as a gap between two suspended blankets. Lower power densities and mass densities are typical of flexible thin-film cells and the higher densities are typical of multi-junction silicon cells, both types are used in a tensioned blanket configuration. The high end of areal densities in the table refer to specialized missions traveling to or through Medium Earth Orbit where a

thick cover glass protection is needed to shield cells from radiation damage. Thin film

cells are less susceptible to this radiation damage therefore do not require as much

protection.

Although not annotated in Table 2, it is worth noting that arrays operating at

higher than typical voltages are lighter-weight than the lower voltage counterparts. The

reason is that higher voltage conduction lines are able to transmit at lower current levels

than lower voltage lines for the same power levels according to Ohm's Law. Lower

currents do not need as much conductor diameter ultimately reducing the copper mass on

the array. For example, blanket areal mass density is reduced by approximately 10%

when the harness voltage level is increased from 70 V to 210 V on a large array. The

table assumes 70 V blanket harnessing.

The final performance measure is the solar array power produced. This will be

reported as a beginning of life (BOL) metric for this study. Arrays generate less power at

the end of mission life (EOL) than at the beginning because cell materials degrade over

long duration exposure to the space environment. An array in low, middle, or

geosynchronous orbit over a typical 7-15 year mission lifetime will generate 25% to 35%

less power at the end of life than at the beginning.[58] Factors that influence these losses

include operating temperature, ultraviolet darkening, thermal cycling, contamination,

radiation, and debris damage. These losses are highly dependent upon the cell substrate

and cover glass material used as well as the array orbital environment. Without

knowledge of these mission and cell construction details, beginning of life power is a

more appropriate metric to compare arrays.

Table 2. Survey of flexible blanket areal mass density and areal power density.

Cell Efficiency and Type	γ (kg/m^2)	ε (W/m^2)	measured, m projected, p
13% Thin Film, a-Si	0.5-2.5	95-113	m
15% Thin Film, 1J CIGS	0.5-2.5	110-130	p
20% Thin Film, 2J CIGS	0.5-2.5	147-173	p
29.5% 3J XTJ/ZTJ**	1.0-2.0	250-280	m
33% 3J IMM	1.0-2.0	290-320	m
35% 4J IMM	1.0-2.0	307-340	p
38% 6J IMM	1.0-2.0	334-368	p
29.5% XTJ/ZTJ, 8x Stretched Lens Array	0.6-1.4	350-420	p
38% 6J IMM, 8x Stretched Lens Array	0.6-1.4	450-540	p
Flexible Blanket Array State of Practice			
1994 Milstar, Si	1.2	97.8	m
1999 Terra (EOS-AM), 18% GaAs/Ge	1.7	120	m
2000 International Space Station, 14% Si	1.2	109	m
2013 Ground Prototype 1, 29.5% XTJ/ZTJ	1.6	280	m
2013 Ground Prototype 2, 29.5% XTJ/ZTJ	1.2	275	m

2.6   Large Space Structures Loading

The next step in the systems analysis process is to consider the loading. Large space structures must endure unique loading regimes that are not intuitive.

Spacecraft attitude control systems tend to drive many of the structural load requirements levied on the large appendages to which they are attached. The three structural parameters that drive the design of spacecraft attitude determination and control systems are as follows: the fundamental frequency of structural vibration, the critical damping ratio, and the mass moment of inertia. As an example consider the case of a flexible beam extending equidistant from a bus. The appendage fundamental frequency, f, is shown to be related to the control system frequency, f_c, through Eq.(21) with the following terms: appendage mass moment of inertia, I_2, bus inertia, I_1, appendage damping ratio, ξ, and order of the roll-off filter, r, where a first order filter is defined as 6dB/octave.[19]

$$\left(\frac{f}{f_c}\right)^{2+r} = \frac{\dfrac{I_2}{I_1}}{\left(1+\dfrac{I_2}{I_1}\right)\dfrac{(3+r)}{2}\zeta}\frac{1}{\zeta} \tag{21}$$

Also, it has been shown that the control frequency is related to the disturbance torque, Q, an allowable angular displacement, delta theta, and the total spacecraft mass moment of inertia about the same axis through Eq. (22).

$$f_c = \frac{1}{2\pi} \sqrt{\frac{\frac{Q}{\Delta\theta}}{I_1 + I_2}} \qquad (22)$$

The conclusion is that low frequency, lightly damped, high moment of inertia structures can impart uncontrollably high loads to the spacecraft bus after being excited by a torque.[53] These high dynamic loads require control actuators with both high bandwidth and high torque authority to execute the artificial damping control schemes necessary to maintain spacecraft stability. Combining high rolloff bandwidth and high torque authority is the most stressing case for attitude control actuators such as momentum wheels, control moment gyros, and torque rods.

Even if spacecraft stability can be maintained in these cases, the time required to stabilize may not be practical. High precision, time sensitive sensing instruments on geostationary missions require the large deployed structures to settle quickly so that sensing data can be collected. Time spent waiting for the array to settle after a torque maneuver is time lost gathering sensing data. In such cases dynamic isolation of the array from the spacecraft bus may be necessary. The Traveler-ARM[54] is one such dynamic isolation solution that allows the sensor to collect data immediately after a maneuver torque. While an elegant solution, this system introduces considerable cost.

Depthless (surface) structures such as most solar arrays are unique in that the dynamic vibration characteristics can be highly non-linear.[53] Since these structures lack depth, deployment hinges become primary load paths. Mechanical hinges commonly used in deployable booms (as opposed to flexible material deformation hinges) are susceptible to manufacturing imperfections that cause joint dead-band. Because these

hinges are primary load paths this dead-band causes uneven blanket tensions and discontinuities in array structural vibration which are manifested as jitter coupled with dynamic shock.[53] The number of kinematic hinges is directly related to the complexity of modeling and ground testing validation efforts.

Array deployed strength limit is defined as the maximum single-event acceleration that the array can endure without failure. A wide range of acceleration magnitudes are possible depending on mission scenarios.

Orbit transfers and earth departure maneuvers require chemical thruster burns that induce large unidirectional impulses into the array. These forces translate to single-event root array accelerations of 0.1 to 0.25 gees (g's)[68]. For these events, the array is assumed to be oriented in the optimal strength direction prior to firing thrusters. For this study, that will be the out-of-plane load direction. Missions requiring spacecraft docking are rare; however if needed they induce single-event accelerations as high as 1g.[55]

Spacecraft angular accelerations are induced by both active and passive means. Spacecraft pointing and orbit correction maneuvers are examples of active acceleration sources. Passive accelerations are caused by gravity gradient, atmospheric drag, and solar radiation pressure. Large area surface structures such as those studied herein are especially susceptible to atmospheric drag and gravity gradient torque effects in low earth orbit.[19] For higher orbits, atmospheric drag and gravity gradient effects fall off and solar pressure is more noticeable although still typically orders of magnitude less than slewing accelerations. The dominating sources of angular acceleration are gravity gradient and slew maneuvers that typically range from 0.01g to 0.001g.[55]

The moments transmitted to the array during these accelerations can be severe. In the extreme case of undamped vibrations from a typical bang-bang slew maneuver, the dynamic load factor can be three times greater than the steady-state applied moment.[56] On the other hand for an optimized slew profile and fully damped vibrations, the input moment is well approximated by a steady-state acceleration.

Damping ratio is a detailed-design-specific parameter that is not likely to be affected by the general differences in architecture type as considered at the conceptual design phase. Rather damping is dictated by the frictional forces and inelastic deformations specific to detailed design aspects such as structural damping, joint friction, and blanket processing. A typical value for damping in mechanically joined precision structures is $\xi \approx 0.01$ (or 1%).[57] For structures that rely on material deformation hinges, the damping value is likely lower than 1% since fewer load paths are contact-friction dependent, a primary source of structural damping. For tensioned blanket solar arrays damping values can be much higher. For the Solar Array Flight Experiment[58] on STS-41D, damping ratios ranging from 2% to 8% were measured during the first bending mode of vibration where the fundamental frequency was measured between the range of 0.059 Hz to 0.072 Hz.

Mass and packaged volume are performance measures that primarily impact the monetary cost of launching a spacecraft. While throw weight is the limiting factor for most launch vehicles, packaged volume is just as important a consideration for large solar arrays. The lower the mass and smaller the stowed volume, the smaller and thus lower

the cost of the launch vehicle. Tens of millions of dollars are saved in launch costs by

moving from a larger to a smaller class launch vehicle.[59]

2.7   Solar Array Parametric Studies

The next step in the systems analysis is to study past work in solar array

parametric sizing studies. Rather than a broad focus on structural size scaling, these

studies have primarily focused on design optimization or on generic mass scaling effects

for a single structural architecture.

The first to note is a parametric comparison of solar array performance based on

detailed part-by-part sizing for generic mission sets by Murphy[60]. One of the stated goals

of this comparison was to understand the trade between thin-film (TF) and crystalline

multi-junction (MJ) devices. The first observation is that array power production,

measured in Watts (W), is a key performance driver. Four essential metrics for evaluating

solar array performance were rank ordered in this study: W/kg, W/m^2, W/m^3, and mass

moment of inertia. Several array structural architectures were compared for each of four

typical mission sets: 3 kW low earth orbit, 10 kW medium earth orbit, 20 kW

geosynchronous orbit, and a 10 kW inter-planetary mission. Each mission listed in

Table 3 has unique environmental and spacecraft pointing considerations that affect cell

degradation, temperature cycles, and structural requirements.

Table 3. Typical missions and derived solar array requirements used in point design comparison.

	LEO	MEO	GEO	Interplanetary (IP)
End of Life (EOL) Power Class	3 kW	10 kW	20 kW	10 kW
Orbit	1000 km, 90° incl.	8000 km, 0°	36,000 km, circular	0.7 to 5 AU
Lifetime	7 years	7 years	15 years	7 years
Temperature Range	120°C to -100°C	110°C to -140°C	100°C to -180°C	150°C to -160°C
Circuit at EOL	30 V	30 V	100 V	100 V
Deployed f_1	0.25 Hz	0.10 Hz	0.05 Hz	0.10 Hz
Deployed Strength	0.01 g	0.01 g	0.007 g	0.01 g
Stowed f_1	40 Hz	35 Hz	35 Hz	40 Hz
Stowed Strength	20 g	20 g	20 g	20 g
Acoustic Loading	147 dB	147 dB	147 dB	147 dB

Three tensioned blanket solar arrays were sized and performance metrics compared for each of these mission sets. Aurora[37] is a rectangular array supported by a single pantograph compression column. UltraFlex[28] is a radial array supported by hinged radial booms. And SquareRigger[45] is a rectangular grillage array supported by smaller rectangular bays of hinged struts. MJ blankets were assumed to be 30% efficient at the beginning of life (BOL) while TF was assumed to be 15%. Table 4 lists the performance metrics of each array point design[60]. All represent AEC-ABLE Engineering designs as of the time of publication, 2002.

In 2000, Hoffman[61], developed a parametric model that compares both tensioned and rigid panel thin-film (TF) and multi-junction (MJ) arrays for a variety of missions

ranging from several hundred watts to 20 kilowatts. This Array Design Assessment

Model (ADAM) accounted for dozens of blanket performance characteristics as well as

power subsystem differences at the spacecraft level. Performance trends were predicted

based on end of life power requirements for each mission considered. Since missions

beyond 20kW were not considered only single wing configurations were included. For

the tensioned blanket devices, a single compression column coilable lattice boom was

used. The boom was sized for a 0.5 Hz fundamental array frequency. Boom strength was

not considered for either loading case: Euler buckling due to blanket tension or critical

moment due to spacecraft slew accelerations.

Both Murphy and Hoffman developed parametric assessments of tensioned

blanket solar arrays but from different approaches. Murphy focused on comparing array

point designs in order to show the benefits and drawbacks of TF and MJ tensioned

blanket arrays sized for realistic loading conditions on three different structural forms,

radial, rectangular single wing, and rectangular grillage. Hoffman on the other hand

showed general performance trends between tensioned TF and MJ arrays for a single

method of structural support, a rectangular blanket tensioned by a coilable lattice boom.

Table 4. Point design solar array comparison.

		UltraFLex (Radial)							Aurora (Rectangular Single Wing)			SquareRigger (Rectangular Grillage)							
Power Goal	kW	3	10	10	20	3	10	10	10	20	20	3	10	10	20	3	10	20	10
Mission	--	LEO	MEO	IP	GEO	LEO	MEO	IP	MEO	GEO	GEO	LEO	MEO	IP	GEO	LEO	MEO	GEO	IP
Cell Type	--	MJ	MJ	MJ	MJ	TF	TF	TF	MJ	MJ	TF	MJ	MJ	MJ	MJ	TF	TF	TF	TF
BOL Power	kW	3.4	15.4	11.1	26.5	3	17	10.2	15.6	24.2	21.9	3.4	18.1	11.1	25	3.2	16.4	22.5	10.7
BOL Specific Mass	W/kg	152	81	204	219	146	53	210	52	104	159	84	85	124	133	96	43	182	168
BOL Areal Power	W/m²	270	305	324	337	113	131	129	305	314	121	259	267	293	288	102	101	118	119
BOL Stowage Efficiency	kW/m³	58	66	70	73	24	28	28	22	30	41	24	48	46	54	15	24	31	25
EOL Power	kW	3	10.2	9.9	20.2	2.7	9.8	9.5	10	20	20	3	9.9	10	20	3	9.7	20	10
EOL Specific Mass	W/kg	133	54	182	167	130	30	196	33	86	145	73	47	111	107	89	26	161	157
EOL Areal Power	W/m²	235	202	290	257	101	76	120	196	260	110	224	147	262	231	94	60	105	112
EOL Stowage Efficiency	kW/m³	51	44	62	55	22	16	26	14	25	37	21	26	41	43	14	14	27	23
Areal Mass	kg/m²	1.78	3.78	1.59	1.53	0.77	2.48	0.61	5.92	3.04	0.76	3.08	3.13	2.37	2.17	1.06	2.33	0.65	0.71
Array Area	m²	13	50	34	79	27	129	79	51	77	182	13	68	38	87	32	163	191	89
Wing Aspect Ratio (L/W)	--	1.1	1.1	1.1	1.1	1.1	1.1	1.1	2.1	3.1	7.4	1	2	1	1.3	1	1	1	0.5
Moment of Inertia	kg·m²	0.32	0.2	0.28	0.19	0.62	0.88	0.58	0.47	0.65	1.73	0.91	0.52	0.8	0.37	1.72	1.15	0.4	0.65
Stowed Volume	m³	0.06	0.23	0.16	0.37	0.12	0.6	0.37	0.36	0.41	0.27	0.14	0.38	0.24	0.46	0.22	0.68	0.73	0.43
Deployed First Frequency	f	0.7	0.12	0.4	0.12	0.9	--	0.4	--	--	--	0.6	0.09	0.24	0.09	0.35	0.06	0.07	0.2
Stowed First Frequency	f	40	40	40	35	40	35	45	--	--	--	114	36	36	49	77	34	49	51
PV Assemblies	kg	6.2	71	18	44	3	138	9	78	51	20	6.8	63	21	47	3.6	142	22	10
Harness	kg	1	4	1.6	3.2	1	3.3	1.6	4.6	4.3	3.4	1	8.8	1.8	2.9	2.1	13	7.2	2.8
Structure and substrate	kg	2	17	4.8	10.1	3.9	16	10.2	60.1	53.5	38.8	2.1	21.5	13.6	30.3	2.9	19.3	16.9	8.4
Mechanisms	kg	0.5	0.6	0.6	0.6	0.6	1	0.6	1.2	1.2	1.3	2.9	4.6	2.9	6.2	2.9	9.4	9.4	5.4
Yoke & Root	kg	1	1.6	1.4	1.9	1.2	1.5	1.9	2.9	2.9	2.9	2.4	5.2	3.1	4.2	2.4	3.8	4.1	2.5
Tiedowns	kg	0.4	1	0.6	0.8	0.5	0.5	0.8	4.1	3.6	2.4	2.4	3	2.6	2.9	2	2	2	2
Total Wing	kg	11	95	27	60	10	161	24	151	117	69	18	106	45	94	16	190	62	32
Off Angle at 90% Power	+/- deg	23	23	23	23	23	23	23	25	25	25	25	25	25	25	25	25	25	25

52

2.8   High Power Mission Applications

The motivation for scaling up flexible blanket solar arrays is to generate more power for future spacecraft. United States Government spacecraft sectors have long expressed the need for more power to both on-orbit assets and exploration spacecraft. In some cases, more power enhances mission goals. In others it enables new missions or reduces mission cost. The highest power arrays that have been used on-orbit generate 18 kW to 25 kW at the beginning of array life and are of rigid panel construction.[62,63] This excludes the eight International Space Station wings that together generate 84 kW[64], but the high mass and packaged volume of these wings required each to be launched separately on the recently retired Space Shuttle and assembled manually in space.

The need is for hundreds of kilowatts rather than only 25 kW. In the last five years alone, the National Aeronautics and Space Administration (NASA) and several Department of Defense organizations have endorsed efforts to develop high power solar arrays. The Defense Advanced Research Projects Agency (DARPA) funded the Fast Access Spacecraft Testbed (FAST)[65]. The Air Force Research Laboratory (AFRL) announced the Advanced eXperiment In Orbital Manipulation (AXIOM)[66] experiment that requires a high power, lightweight solar array to power Hall effect thrusters. NASA recently awarded several industry contracts to study solar electric propulsion mission concepts that include risk reduction of high power, lightweight solar arrays.[10]

In the early 2000's, the AFRL initiated a program called PowerSail to develop a generic solar array system capable of supporting growth in satellite power demand for the next 20 years.[67] The driving need was for an array scalable beyond 100 kW but that

could be acquired at a 5X decrease in cost, a 5X increase in watts per kilogram, and a drastic decrease in the stowed volume of the array. Cost, mass, and stowed volume were recognized as the three primary constraints that limit available power in present day satellites. This program yielded a specific solar array concept of which sub-scale deployable modules were ground tested, but the full array was never matured into the flight demonstration phase. Yet the need for more power continues to prevail.

A 2010 Aerospace study revealed several defense missions that are either enhanced or enabled by higher power, lighter weight, more compactly packaged solar arrays. Table 3 lists the power levels required to enable each respective mission.[65]

NASA has expressed interest in high power solar arrays scalable to 400 kW for the purpose of solar electric propulsion (SEP) tugs. Table 5 shows that the defense need for SEP tugs is to transfer communications satellites from a LEO to a GEO orbit. The NASA need is similar except the purpose is to travel beyond earth orbit for human exploration of Mars, human rendezvous with a near-earth asteroid, or science missions to the far reaches of the solar system.[68]

The SEP tug concept relies on chemical rockets to launch heavy payloads into LEO then uses electric propulsion combined with high power solar arrays to transport these payloads to higher orbits or beyond Earth orbit to an assembly point such as the Lagrange point between the Earth and the moon where modules are joined in preparation for the long trip to a nearby planet or asteroid.[69] The advantage of electric propulsion is that it does not require expendable chemical agents for propulsion fuel therefore propulsive impulses can be sustained almost indefinitely. The specific impulse is

estimated to be ten times higher than that of chemical propulsion.[68] NASA roadmaps for

science, exploration, and advanced technology all consider SEP as a vital future

capability.[69]

Table 5. Defense and civil missions enabled by increasing available power on-orbit.

	Power Required to Enable
Laser Communications	100 kW
Laser Remote Detection of Chemical Species	50 kW
Laser Water Vapor Atmospheric Profile	100 kW
Laser Space Defense	220 kW
LIDAR Terrestrial Imaging from 1500 km	100 kW
Airborne Moving Target Indicator Radar	65 kW
Space Solar Power Demonstrator	700 kW
Electric Propulsion LEO to GEO Orbit Transfer from a Minotaur IV Class Vehicle	15 kW
Electric Propulsion LEO to GEO Orbit Transfer of 100 kW Communications Sat	200 kW

CHAPTER 3.   ANALYTIC APPROACH

The systems analysis reported in the previous chapter forms the basis upon which a solar array model is formed. This model represents all practical rectangular flexible blanket solar array architectures and is defined by a minimum set of performance constraints and design parameters. The analytical process developed to operate on this model is then presented. Solutions are generated that quantify the effects of each design parameter on array performance.

3.1   Performance Parameters and Design Variables

Based on the systems analysis reported in *Chapter 2*, the solar array performance constraints considered in this analytical model include the following: the deployed area (a quantity proportional to the total power produced), the fundamental frequency of vibration, and the maximum acceleration strength limit. Other external design attributes are certainly affected by architecture selection but are not quantified for consideration herein; these include packaging efficiency and several sources of cost such as fabrication, analysis, test, integration, deployment, and on-orbit operations.

The worst case external loads applied to the array are assumed to be rectilinear accelerations. The source of these loads includes spacecraft thruster impulses or rendezvous docking event impulses. Attitude control slew maneuvers are also a common acceleration source, but these loads are rotational in nature and much lower in magnitude than the rectilinear acceleration sources. The solar array failure mode is assumed to occur as an out-of-plane bending due to these acceleration loads, reacted in the boom as a maximum root moment. Knowledge of the exact boom failure mode or design margin is

not needed for this study. Instead it is only necessary that the boom design limit moment be known.

The solar array architecture is structurally represented by three components—the blanket, the primary boom, and the spreader bar—each having a unique contribution toward system performance and mass. The blanket design is further defined by three parameters: the deployed area, areal mass density, and the applied tension load. The spreader bar is defined only by the length and linear mass density since it is assumed rigid.

Figure 20 provides a physical description of the model used as the basis for this constraint analysis. The primary support booms are beam columns that serve three functions:

1) react the tension load in the blankets,

2) stiffen the array system in conjunction with the tensioned blankets, and

3) strengthen the array system.

The boom design is therefore characterized only by performance measures: flexural stiffness, strength limit moment, linear density, length, and quantity.

The solar array structural system is defined as the unique assemblage of these three primary components and the performance ranges of each. While rectangular in dimension, the array system size is defined by the blanket area where the length is equivalent to the primary boom length and the width equivalent to the spreader bar length. The structural system is further defined by the quantity of primary booms used to deploy and tension the blanket(s) and achieve system stiffness and strength.

Array Requirements
[f, a, A]

Spreader Bar
[w_{sb}]

Primary Booms
[EI, M, w_{pb}, L, n]

Photovoltaic Blanket
[γ_b]

Rigid Spacecraft Interface or
Backbone Boom
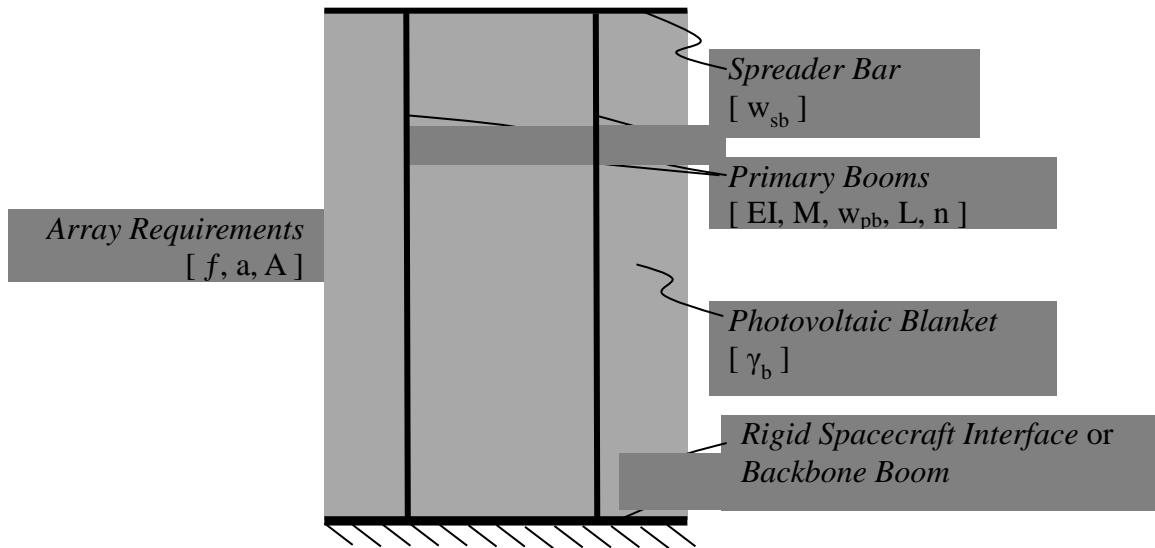
Figure 20. A physical description of the constraint analysis model.

The physical model as illustrated in Figure 20 considers any number of primary

support booms arranged in a parallel layout. The inertial loading is assumed to be evenly

distributed across all booms, and the bending stiffness of each boom is combined into an

equivalent array bending stiffness as will be detailed in a section to follow. The spreader

bar connects the boom tips and transfers blanket tension loads into boom compression

loads. The bar is characterized by a linear density and is assumed rigid based on the fact

that standard solar array design practice is to size the spreader bar stiffness to be much

higher than that of the primary booms in order to avoid substantial blanket shear strains.

While the figure shows two primary booms as an example, the model considers a range

of primary boom quantities [1:10] and a large blanket area range [10:2000] m^2.

The blanket component is characterized only by two terms, area and areal mass

density. The area of the blanket is the product of the primary boom length and the

spreader bar width. This assumption does not account for gaps between adjacent blankets

where no active multi-junction photovoltaic cells are populated which is sometimes

necessary in practical design to allow room for deployment of primary booms or to modularize blanket fabrication. A wing on the ISS, for example, has an active area that is about 80% of the total projected area. Two 4.57 meter blankets are stretched along either side of a 2-meter gap that allows room for deployment of the ATK FAST mast.

Note that neither the blanket tension nor the boom critical Euler load is listed as a design parameter despite the obvious influence on array strength and fundamental frequency performance. The reason is that these equitable quantities were discovered to be readily optimized by maximizing the coupled beam-blanket fundamental frequency. The optimized blanket tension and the approximate fundamental frequency solution is developed in a section to follow, *Clamped-Free Beam-Cable*.

The interface between the array and the spacecraft is assumed to be rigid and thus is represented as a clamped boundary condition in the model. This assumption renders the results relevant to the widest possible range of array sizes but still allows the user space to consider the mass and stiffness effects of the attachment method.

Two methods are typical as illustrated in Figure 21, one for a small array and one for a very large array. A small 10 m^2 array would likely be joined directly to a spacecraft bus through a yoke structure and a solar array drive assembly interface, no backbone boom is needed. In practice this interface introduces additional compliance and mass to the array structure resulting in a lower fundamental frequency of vibration. Quantifying this effect requires detailed knowledge of the spacecraft construction and therefore is not appropriate for this model.
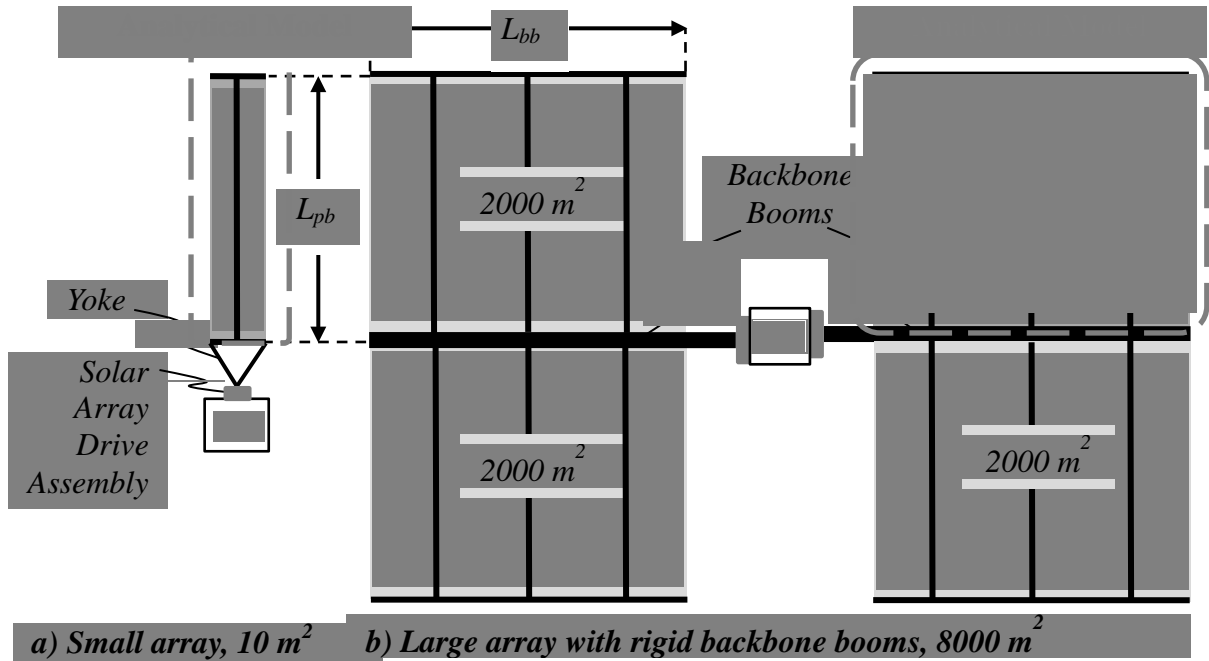
Figure 21. The smallest and largest array sizes considered in the constraint model.

On the other hand a very large 8000 m^2 array would likely be split into two

4000 m^2 wings, each wing constructed of multiple winglets, joined down the center by a

backbone boom. While the backbone boom and the winglets are dynamically coupled, it

is most convenient to separate the individual effects in order to preserve generalization of

the structural scaling results. In practice the backbone boom is likely to be sized

according to the principle that the system fundamental frequency shall be lower than that

of the individual solar array winglets by some multiplication factor of two or greater.

This sizing requirement is necessary in order to prevent the excitation of symmetric mode

shapes during a spacecraft acceleration maneuver. Symmetric mode shapes create a

dynamic vibration scenario that is highly problematic from a spacecraft attitude control

standpoint—several different fundamental modes of vibration oscillate at identical

frequencies rendering active control schemes ineffective at compensating. Nevertheless, the backbone boom is considered rigid herein.

Table 6 lists the practical range of performance constraints and component properties that bound the solution space for the array model. This data is compiled from several heritage tensioned blanket array systems including Milstar[7,7], APSA[70,71], Terra EOS-AM[6,72], Olympus[73], Hubble Space Telescope[4], and the International Space Station[5]. Recent and projected advancements in solar array architectures[74], cell power conversion efficiency trends[75] are all captured in this table.

Table 6. Practical ranges used to bound the constraint analysis solution space.

		Range	Units
Objective Constraint			
Areal Mass Density	γ	0 - 10	kg/m^2
Array Performance Parameters			
Fundamental Frequency	f	0.001 - 5	Hz
Lateral Acceleration Load	a	0.001 - 0.2	$9.81 \ m/s^2$
Deployed Area	A	10 - 2000	m^2
Primary Boom Properties			
Beam Efficiency Index	μ	1 - 5000	$N^{3/5}m^{9/5}/ \ kg$
(Flexural Stiffness)	EI	--	$N \ m^2$
(Moment Strength)	M	--	N m
Structural Mass Fraction	β	0.01 - 0.5	kg/kg
(Linear Mass Density)	w_{pb}	--	kg/m
Length	L_{pb}	5 - 30	m
Boom Quantity	n	1 - 10	--
Blanket Properties			
Areal Mass Density	γ_b	0.5 - 2.0	kg/m^2
Spreader Bar Properties			
Linear Mass Density	w_{sb}	1 - 5	kg/m

3.2   Analytic Process Flow

Figure 22 illustrates the overall flow of the constraint analysis process that has been developed for this solar array model. The process starts by categorizing the three array performance constraints then defining the minimum set of component parameters necessary to characterize the structural architecture in light of the constraints as reported in the previous section. Loading equations are then developed to characterize array fundamental frequency and strength. These functions are substituted into the beam efficiency index in order to consolidate bending stiffness and strength limit into a single beam efficiency term that also quantifies beam cost.

Next, the array weight equation is developed in terms of the component design parameters and array performance constraints. For example, this weight equation combines mass terms for the three array components: primary boom, blanket, and spreader bar.

This weight equation is solved by numerical methods. Throughout this process, the array mass and beam efficiency (i.e., cost) are simultaneously minimized. This minimized beam efficiency value and minimized array mass value is recorded for each of 2,430 design cases to form the approximation model. The approximation model is then tested for accuracy and symbolic expressions developed using error minimization techniques. The last step is then to extract the scaling metrics from the approximation model that represent solar array scaling trends.

PERFORMANCE PARAMETERS	COMPONENT DESIGN PARAMETERS	OBJECTIVE FUNCTION

$f \geq f$ required
$\alpha \geq \alpha$ required
$A \geq A$ required

EI, M, n, L, γb, wsb, wpb

Develop the array weight equation as the sum of beam, blanket, and spreader mass:
$\gamma = f\,(\mu,\ a,\ f,\ L,\ A,\ n,\ \gamma b,\ wsb,\ wpb)$

Develop functions for array frequency and strength in terms of component design parameters:
FEA→ $f = f\,(EI,\ L,\ A,\ n,\ \gamma b,\ wsb,\ wpb)$
First Principles→ $\alpha = f\,(M,\ L,\ A,\ n,\ \gamma b,\ wsb,\ wpb)$

Solve numerically then graphically explore the relative influence of all max/min combinations of design parameters on array mass, γ.

Beam efficiency index:
$\mu = f\,(M,\ EI,\ wpb)$

Form approx. model of 2,430 cases by constraining the solution to the min. mass and beam efficiency.

Eliminate M and EI by rearranging frequency and strength functions and substituting into the beam efficiency function:
$\mu = f\,(a,\ f,\ L,\ A,\ n,\ \gamma b,\ wsb,\ wpb)$

Use regression techniques to extract approximate symbolic relationships between γ and $[\alpha,\ f,\ L,\ A,\ n,\ \gamma b,\ wsb,\ wpb]$

Figure 22.   Constraint analysis process flow.

Solar array power production, measured in Watts, is not directly included as a parameter in the model development since it has no bearing on the array structural behavior. Instead, blanket area and areal mass density are considered. Array power production is readily predicted with knowledge of the array area and the power conversion efficiency of the selected photovoltaic cell.

3.3   Observations

This analytical model is developed to represent the structural dynamics and strength behavior of a general rectangular tensioned blanket solar array architecture. The architecture is constructed from one or multiple beam columns that support a tensioned

photovoltaic blanket ranging in area from 10 to 2000 m^2. This model leverages first

principles, finite element techniques, structural indices, and numerical analysis methods

to relate the array frequency and strength constraints to component sizes and layouts

needed to meet those constraints while minimizing both array mass and beam cost. This

numerical model is not the goal of this overall work, only the basis upon which a

symbolic approximation model and ultimately metrics are developed to represent the

structural scaling behavior of an array architecture.

CHAPTER 4.   ARRAY LOADING

This chapter reports on the development of fundamental frequency and strength relations for the tensioned blanket solar array model. This analytical development leverages first principles, finite element techniques, and minimization techniques. Appendix A is provided as a supplement to this chapter for more detail into the finite element structural model.

This structural model is developed to represent a tensioned blanket solar array as a coupled system. The hypothesis is that a large aspect ratio (i.e., long and narrow) tensioned blanket can be structurally represented by simple tensioned-cable mechanics rather than by the more complex membrane mechanics. Since by definition cables do not have torsional modes of structural vibration, it is necessary to discuss the practical design parameters by which tensioned blankets vibrate in torsion versus the out-of-plane sinusoidal shapes typical in the fundamental mode of structural vibration. This discussion is also useful for discerning the parameters by which very large arrays with backbone booms vibrate in torsion versus bending. A discussion of cable dynamics is provided first, followed by an analytic examination of slender beam dynamics, and finally empirical data is provided for validation.

4.1   Cable-Membrane Approximation

The structural dynamics behavior of a cable and a membrane are quite different. The simplest place to start in understanding these differences is the example of a suspended straight cable with fixed boundaries. The fundamental frequency of this

component is well known as Eq. (25), defined by three terms: cable tension, length, and linear mass density.[76]

$$f = \frac{1}{2L} \left(\frac{T}{w} \right)^{1/2} \tag{23}$$

This one-dimensional cable equation can be extended into a two-dimensional "areal" cable by introducing the width dimension to the tension and mass terms expressed as Eq. (24).

$$f = \frac{1}{2L} \left(\frac{S}{\gamma} \right)^{1/2} \tag{24}$$

But the behavior of this relation is still one-dimensional. A cable does not account for shear effects thus a torsion mode of natural vibration is not possible, only sinusoidal mode shapes are possible. A membrane, on the other hand, does exhibit some torsion/shear stiffness that is readily approximated. For example, a membrane tensioned to a fixed distance then twisted reacts with a restoring force that drives the membrane back to the equidistant equilibrium state, a behavior that resembles a torsional pendulum seeking equilibrium. Equation (25) was published in 1973[77] as a tool for approximating the lowest torsion frequency of such a membrane assuming a rigid column support and a mass-less, rigid spreader bar on a twisting pivot. This relation was developed at a time when tensioned blanket solar array options were being evaluated for the ISS.

$$f = \frac{\sqrt{3}}{2\pi L} \left(\frac{S}{\gamma} \right)^{1/2} \tag{25}$$

Notice that this equation matches the cable solution from Eq. (24) sans the constant reduction of the square root of 3 divided by pi or approximately 0.55. Therefore

the fundamental frequency of torsional vibration for a narrow blanket is approximately half that of out-of-plane sinusoidal vibration. Of course, this conclusion assumes a rigid support column.

Next, the dynamic behavior of the support is examined to provide further understanding of the tensioned blanket solar array modes of fundamental structural vibration. The fundamental frequency of torsional vibration of a slender shaft is expressed by Eq. (26) in two forms.[77]

$$f_{torsion} = \frac{1}{4}\left(\frac{GJ}{\rho I_p L^2}\right)^{1/2}$$
$$f_{torsion} = \left(\frac{3GJ}{32\gamma W^3 L^2}\right)^{1/2}$$

(26)

The first form is generic, and the second is modified to account for the polar area moment of inertia of a rigid rectangular blanket joined to the beam-shaft. The blanket is characterized by an areal density, γ, length, L, and width, W. This expression is valid for both array layouts illustrated in Figure 21. For a single-beam-blanket segment, L_{pb} is substituted for the generic length term in Eq. (26). For the backbone boom array system, L_{bb} is substituted for the length term, and $2L_{pb}$ is substituted for the width term as the primary boom mass and blanket mass are lumped into the areal mass density term. This relation does not apply to array configurations where multiple primary booms support a single blanket; such cases are expected to respond exclusively in a bending mode of structural vibration due to the shear frame stiffness effect.

The fundamental frequency of bending vibration is represented by the expression for a clamped-free Euler-Bernoulli beam in Eq. (24).[78] As before, both the generic form and the modified forms are expressed.

$$f_{bending} = \frac{3.516}{2\pi}\left(\frac{EI}{wL^4}\right)^{1/2}$$

$$f_{bending} = \frac{3.516}{2\pi}\left(\frac{EI}{2\gamma WL^4}\right)^{1/2}$$

(27)

Equations (3) and (4) are combined into a ratio of the torsion frequency to the bending frequency expressed as Eq. (28).

$$\frac{f_{torsion}}{f_{bending}} = 1.5476\left(\frac{GJ}{EI}\right)^{1/2} AR$$

$$AR = \frac{L_{pb}}{W}; \text{ for a beam-blanket segment, e.g., Fig. 21a}$$

$$AR = \frac{L_{bb}}{2L_{pb}}; \text{ for a backbone boom system, e.g., Fig. 21b}$$

(28)

The blanket aspect ratio term, *AR*, is defined for the two extreme array size classes previously discussed and illustrated in Figure 21a and 21b respectively, a beam-blanket array segment and a backbone boom array system. In this ratio form, a value less than one indicates the fundamental mode of structural vibration to be torsion; conversely a value greater than one indicates the mode to be bending. Notice the beam stiffness ratio term *(GJ/EI)$^{1/2}$* is representative of either a primary boom or a backbone boom depending again on the respective use of the relation for either a beam-blanket segment or a backbone boom system.

Figure 23 uses the frequency ratio to show how the array aspect ratio and beam stiffness ratio affect whether the array mode of fundamental vibration is expected to be

torsion or bending. For large aspect ratios (e.g., long and narrow), the lowest frequency

of fundamental vibration occurs as a bending mode for all but only extremely small

stiffness ratios where *GJ* is very low when compared to *EI*. For example when *AR = 10,*

torsion is expected only when $(GJ/EI)^{1/2} < 0.065$, indicative of a boom with extremely

small torsion stiffness such as an open section tube.
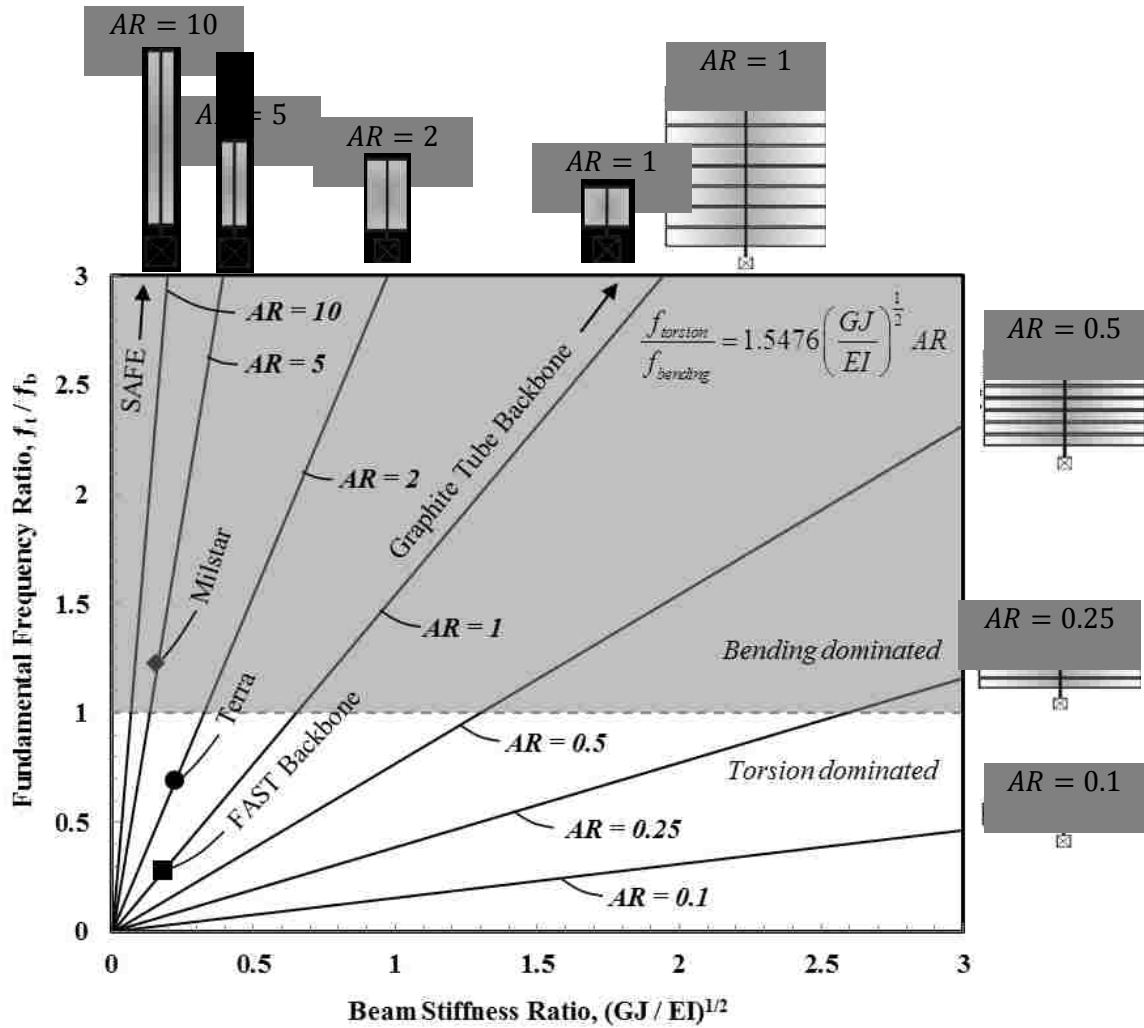
Figure 23. Array aspect ratio and the support beam stiffness ratio related to the fundamental mode of structural vibration.

Conversely, for small aspect ratios, the lowest frequency is more likely to be torsion unless a boom with very high torsion stiffness is used. When *AR = 0.1*, torsion is expected when $(GJ/EI)^{1/2} < 6.48$, indicative of a closed-section tube or a robust articulated truss. In summary, the smaller the aspect ratio, the greater the boom *GJ* required to ensure the fundamental frequency of vibration is a bending mode rather than a torsion mode. The inverse is also true. Several empirical examples are plotted in Figure 23 to add confidence to the developed relation. Each example is further described in the following.

The Solar Array Flight Experiment (SAFE) was conducted in 1984 on the Space Transportation System-41D[35] mission. A 4.0 meter wide by 30.9 meter long blanket (i.e., *AR = 10*) was deployed and supported with a continuous longeron lattice truss column. Given the estimated stiffness ratio of the truss-column to be well above one and the aspect ratio to be large, the frequency ratio for this example is expected to be well above one, strongly into the bending dominated range as indicated in the figure. On-orbit dynamic measurements of this array confirm this to be true. The on-orbit deployed fundamental frequency was measured to be in the range of 0.059 Hz to 0.072 Hz depending on tension variability and orientation to full-sun or eclipse. The mode shape of fundamental vibration is observed to be very similar to a clamped-free beam. There are no noticeable torsion or transverse bending components to these blanket mode shapes, only out-of-plane sinusoidal shapes were observed.

A second example is established by one of the most proliferated tensioned blanket solar arrays on-orbit today, on Milstar, perhaps second only to the ISS. Each spacecraft

in the Milstar constellation uses a 2.97 meter wide by 14.8 meter long solar array blanket (i.e., *AR = 5),* each supported by a continuous longeron mast. The mode shape of fundamental vibration was analytically predicted to be out-of-plane bending at a frequency of 0.162 Hz. The second and third modes of vibration are expected to be in-plane and torsion modes at frequencies of 0.200 Hz and 0.391 Hz respectively.[7] When this example is plotted on Figure 23 based on the beam stiffness ratio and array aspect ratio, the frequency ratio is 1.25 as expected based on the published analytic prediction that bending is the lowest mode of fundamental vibration but the fundamental mode of torsion vibration is not far away.

A third and final example is provided by the most recently known tensioned blanket array to be deployed on-orbit, the Terra (EOS-AM) spacecraft. Similar to the previous two examples, deployment and tensioning was accomplished with a single continuous longeron truss column. This blanket is relatively short but wide, measuring 8.92 meters long and 5.08 meters wide (i.e., *AR = 2).* According to the estimated beam stiffness ratio of 0.134, this array falls into the torsion dominated region of the figure with a predicted frequency ratio of 0.56. The actual fundamental mode of structural vibration is not confirmed, although the minimum required fundamental frequency is recorded as 0.16 Hz.[6]

Two imaginary backbone boom cases are also provided in Figure 23 for the likely array aspect ratio of one. The first backbone type is a high modulus carbon fiber composite tube with a diameter of 30 cm and a wall thickness of 1 cm. The stiffness ratio for this boom is estimated to be *(GJ/EI)$^{1/2}$ = 38.7,* and the corresponding frequency ratio

is 59.9, well into the bending dominated range. On the other hand, an articulated four-longeron truss such as the ATK FAST mast behaves quite differently than the tube. The stiffness ratio and frequency ratio for this truss as the backbone on a square aspect ratio array are $(GJ/EI)^{1/2} = 0.18$ and $f_t/f_b = 0.28$ respectively, down into the torsion dominated frequency range. Two different backbone boom architectures yield two very different frequency responses; the truss backbone responds fundamentally in torsion and the tube backbone in bending.

4.2   Clamped-Free Beam-Cable Fundamental Frequency

The next step is to capture the coupled dynamic effects of a beam-blanket solar array segment. A finite element model is created to predict the coupled fundamental frequency response of a beam-cable assembly and used to develop a relation that approximately represents this response given practical design ranges. The presumption in this section is that the dynamic response of the suspended cable is substantially affected by the motion of the beam to which it is attached and vice versa.

The beam is assumed constrained in a clamped-free condition and the cable is fixed to the two opposing beam ends. Naturally the beam boundary condition has an impact on the cable dynamic behavior. Common practice in modeling an appendage joined to a spacecraft bus is to assume one of two boundary conditions, pinned-pinned or clamped-free. The pinned-pinned condition is appropriate when a long beam is joined to a bus at the beam mid-point or when the beam mass is much greater than the bus mass. The beam mode shape of fundamental vibration then naturally creates a node at the bus attachment point closely approximating a true free-free on-orbit condition. A clamped-

free condition is more appropriate when the bus mass is commensurate with the beam mass or when the structural interface needs to be modeled separately. The wide range of array sizes considered in the present study warrants the use of a clamped-free boundary condition. This allows the results to be used in either the case of a yoke spacecraft interface or a backbone boom interface.

Two fundamental mechanics properties drive the dynamic response of a tensioned beam-cable system—tension stiffening of the cable and compression softening of the beam—properties that are in direct contrast when the tension in the cable is equivalent to compression in the beam as assumed here.

The fundamental frequency of a straight cable is dependent on only three parameters: mass, length, and tension. As shown previously by Eq. (25). Strictly speaking all physical cables have a non-zero bending stiffness, but it is insubstantial when compared to the tension-induced stiffness; therefore it is common practice to assume it is zero due to the small area moment of inertia.

The fundamental frequency of a generic beam on the other hand is characterized by mass, bending stiffness, and torsion stiffness since a beam, by definition, has a substantial area moment of inertia. The stiffening or softening effect of tension or compression loading is typically neglected unless that load is high relative to the critical Euler load. For large space structures, beams are commonly long and narrow (i.e., slender), rendering them susceptible to Euler buckling. Therefore the beam tension and compression loads must be considered for these cases.

To date this compression-softening and tension-stiffening effect has not been considered in developing structural metrics for a beam-cable assembly likely due to the absence of a readily available closed form solution for such an assembly. Common practice is instead to distribute the cable (i.e., blanket) mass onto the beam for convenient use of well-known beam fundamental frequency relations. For example, a common reference material[78] reports independent closed form solutions for a cable in tension and a beam in compression, but the coupled effects are not considered. The approach of the current effort is to model these coupled effects using finite element analysis techniques then through observation and optimization, develop an approximate fundamental frequency equation for a beam-cable assembly.

The fundamental frequency of a clamped-free Euler-Bernoulli beam has been previously defined as Eq.(24). An approximate solution is also available that captures the compression softening effect and the tension stiffening effect of the load P applied uniaxial to a beam listed as Eq. (29), an expression that is readily used along with Eq. (24).

$$f_{\text{withaxialload}} = f_{\text{noaxialload}} \left(1 + \frac{P}{P_{cr}}\right)^{1/2} \tag{29}$$

The fixed-free Euler buckling load is denoted by P_{cr} and is defined by Eq. (30).[79] This represents the special case when the compressive load always points back to the column root rather than fixed in one downward direction as is commonly assumed. The cable follower load case used here has a critical load four times higher than the classical Euler load case.

$$P_{cr} = \pi^2 \frac{EI}{L^2} \qquad (30)$$

The ABAQUS/Standard[80] commercial finite element analysis code is used to model the beam-cable assembly. Figure 24 shows the model components, illustrating that the tension load in the cable is equivalent to the compressive load in the beam. While the figure shows the cable deformed for illustrative clarity, the model considers the beam and the cable to be collinear in the unperturbed state. A detailed description of the finite element model is provided in Appendix A.
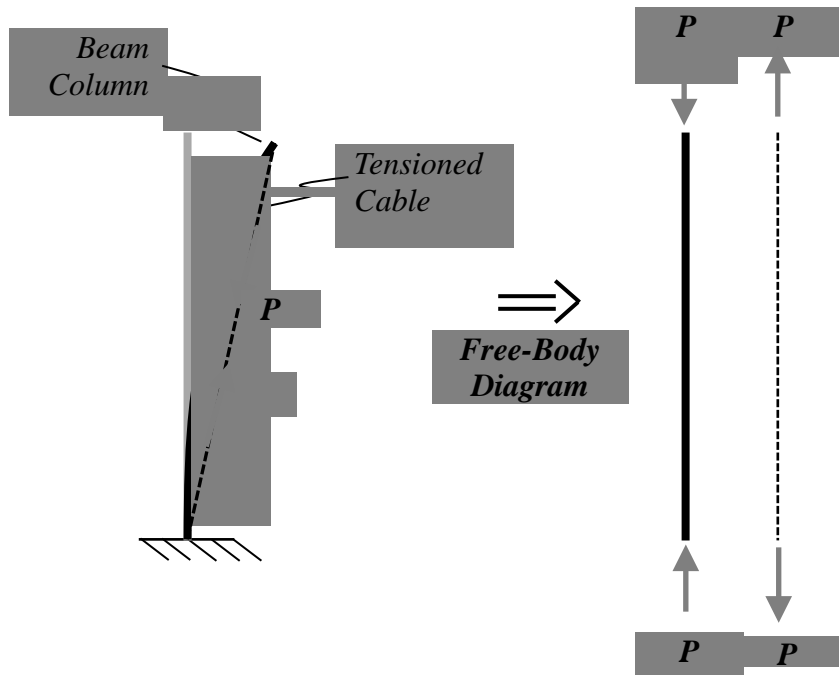
Figure 24. A physical description of the finite element numerical model.

A parametric study is performed on six different beam elements and four truss elements where the fundamental frequency and critical buckling load is predicted using a linear perturbation analysis and compared to the respective closed form equivalents, Eqns. (24) and (26) respectively. Cubic Euler-Bernoulli beam elements (i.e., B33) are

selected as a result. This element type is valid when no transverse shear deformation is expected, when plane sections remain plane (i.e., no warping), when the beam is considered slender such that the ratio of diameter to length is less than 1/15, and when transverse loading is expected. For the cable component, two-node truss elements (e.g., T3D2) with null compressive stiffness are selected. The cross-sections of the beam and cable components are chosen arbitrarily, and the length is chosen to be 1 meter for convenience. These elements prove to be the most consistent in predicting the frequency over the range of compression loads and tensions of interest.

A mesh density study is performed on the two beam and truss element types with fundamental frequency again used as the figure of merit. Five element lengths were compared: 4 cm, 2 cm, 1 cm, 0.5 cm, 0.25 cm. As expected the results showed the frequency drops as element length is shortened—finer mesh densities generate more compliant models. The frequency changed by less than one hundredth of a percent from the 1 cm to the 0.5 cm size; therefore 1 cm length is selected. The beam and cable components are each represented by one hundred elements.

This beam-cable model is subjected to a series of parametric analysis cases to understand the impact of tension and mass fraction on the system fundamental frequency. The cable tension is varied over a range from zero to the critical Euler load given as Eq. (30). The mass is parameterized through two terms, the cable linear mass density and the structural mass fraction. Structural mass fraction is the ratio of the primary boom (column) mass to the total payload mass that includes the boom and all parasitic, non-

structural masses such as the photovoltaic blanket and in later cases the spreader bar.

This fraction is defined by Eq. (31).

$$\beta = \frac{m_{pb}}{m_{pb} + m_{sb} + m_{b}} = \frac{m_{pb}}{m} \qquad (31)$$

A mass fraction range of 0.01 to 0.5 is used in the present study. It is important to note that this mass fraction includes only the cantilevered components, those that have the strongest influence on fundamental frequency. Solar array components at the root have little contribution to modal mass. These include the root pallet, yoke, and any mechanisms or restraint devices fixed to the root. These components will be documented later for the effect on total mass but are not included in the analytical development of strength and fundamental frequency.

The cable tension is controlled in the model using a temperature gradient applied as an initial condition. The cable tensile strain directly transfers into the beam column as a compressive load through a rigid tie constraint during the first analysis step. The non-linear solver is used in the first step to enable the tension and compression pre-loads to transfer to the second step, a linear perturbation dynamic analysis. The system fundamental frequency is extracted as the first non-zero eigenvalue frequency regardless of whether the motion is dominated by the beam or by the cable.

Figure 25 shows the results of the analysis in terms of three normalized quantities: the load ratio of cable tension to the critical Euler load on the abscissa, the frequency ratio on the ordinate, and the structural mass fraction. The ratio of the model fundamental frequency to the closed-form beam-only frequency, Eq. (24), where the cable mass is distributed along the beam length. The horizontal line at the top of the

figure represents this normalized frequency value. The additional effect of a compressive

load on this closed-form beam solution is also represented as defined in the figure by

Eq. (29). Notice that when no load is applied the frequency ratio is unity, but as

compression is introduced the beam frequency drops, eventually falling to zero as the

load approaches the critical Euler load. The exact solution for a tensioned cable is also

plotted from Eq. (25). The effect is opposite that of the compression beam. For a cable
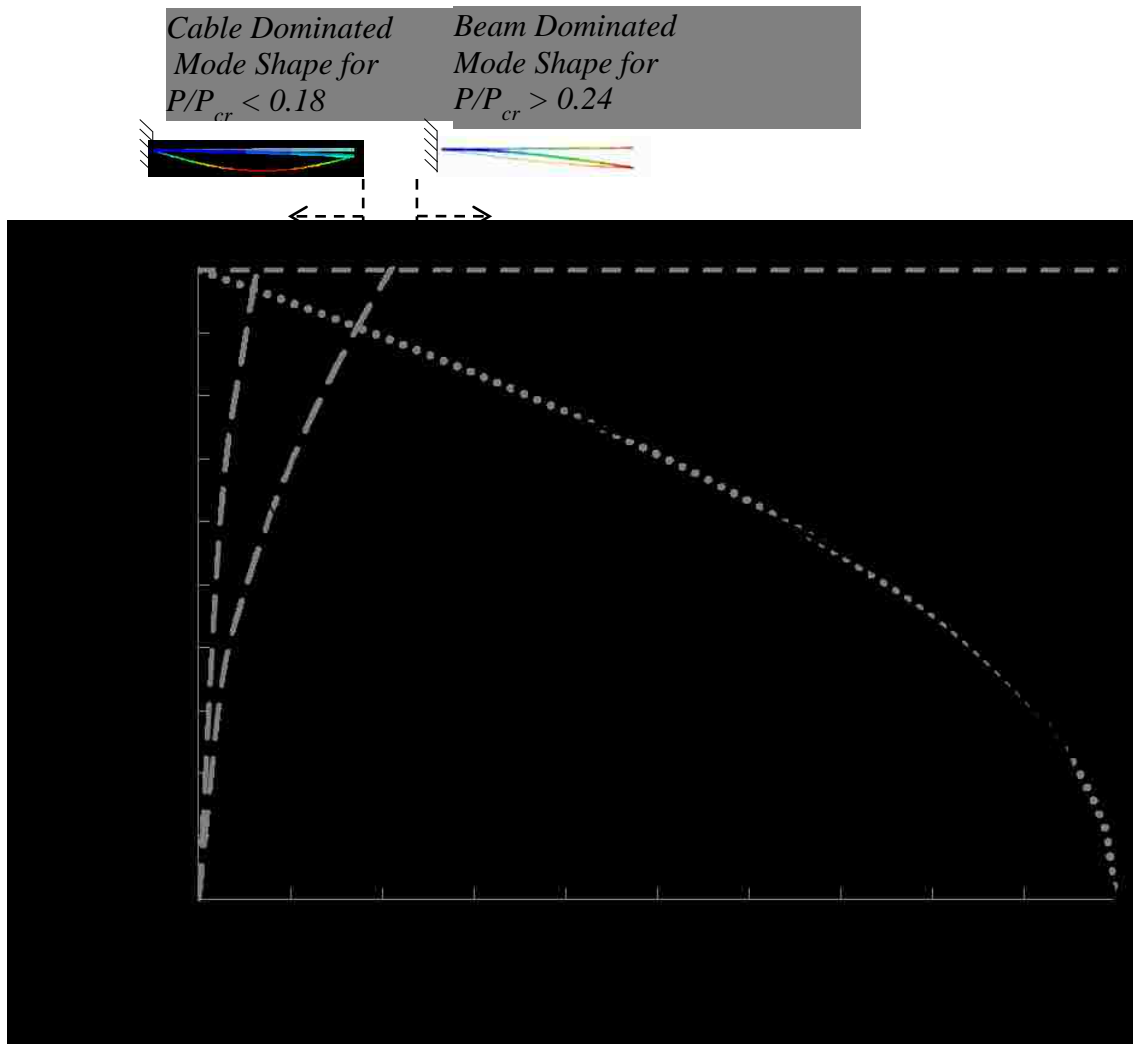
Figure 25. The beam-cable system fundamental frequency related to axial compressive load

ratio.

under zero tension the frequency is zero. As tension increases from zero, the frequency

quickly rises as expected. The blanket torsion frequency is also plotted in the figure

based on Eq. (25). The results show the same trend as the cable-only solution but at a

lower frequency by a factor of 0.55 as discovered previously.

For all three structural mass fraction cases in Figure 25, the frequency ratio shows

vibration of a narrow tensioned membrane, defined by Eq. (25), is similar to the

fundamental cable frequency, and both are higher than the peak frequencies of the beam-

cable assembly. This observation adds credence to the assumption that the cable

mechanics adequately approximate a blanket for tensioned solar array architectures.

For all three structural mass fraction cases in Figure 25, the frequency ratio shows

a two-part response that is similar in magnitude between the three. First the system

frequency rises sharply as cable tension increases from zero to about 18% of the critical

Euler load. For this stage the mode shape of fundamental vibration is dominated by cable

motion; the beam moves very little.   From there, the frequency levels off before starting

into the second stage of the response at about 24% the critical Euler load. The frequency

steadily decreases back down to zero as the cable tension approaches the beam critical

Euler load. The dynamic motion during this second phase is dominated by the beam as it

slowly suffers from compressive softening effects. The first stage of the frequency

response closely resembles the exact solution for a cable. Similarly the second stage

response resembles the approximate solution for a compression beam.

It is observed that since a clamped-free beam does not have symmetric boundary

conditions that the dynamic response is tightly coupled between the cable and beam. For

79

example, beam tip motion demands cable motion, regardless of the cable tension or mass. If the tension is low and cable mass high then the cable contributes a strong inertial mass to the beam response; conversely if the cable tension is high and the mass is low then the cable introduces compliance into the beam response. In both cases, the cable has a reduction effect on the system fundamental frequency.

This frequency response in Figure 25 is surprisingly insensitive to the large changes in the structural mass fraction, $\beta = 0.01$ to 0.5. The peak frequency for the largest structural mass fraction beam-cable is 0.82 of the exact beam frequency, and this occurs at a 18% the critical Euler load. On the other hand, the peak frequency for the smallest structural mass fraction case was 0.70 of the exact beam frequency at a load ratio of 0.24. This consistent behavior lends itself to a convenient approximation of the fundamental frequency of a generic beam-cable system. The average peak frequency and load ratio is calculated from the two bounding cases for structural mass fraction. The desired blanket tension is 0.21 of the critical Euler load, and the fundamental frequency of a beam-cable is less than the exact clamped-free solution by a factor of approximately 0.76. This is introduced as the frequency knockdown factor δ in Eq. (32), a modified relation for the fundamental frequency of a clamped-free beam. Note that the linear mass density term, w, includes both the beam and blanket mass.

$$f = \delta \frac{3.516}{2\pi} \left(\frac{EI}{wL^4} \right)^{1/2} \tag{32}$$

Equation (32) approximates the fundamental frequency of a clamped-free beam-cable assembly. This coupled beam-string fundamental frequency is insensitive to changes over the structural mass fraction range considered, $\beta = 0.01$ to 0.5, but is highly sensitive

to changes in the cable tension. The desired cable tension is determined to be 21% the critical Euler load of the support column. The system fundamental frequency of vibration at this optimized tension level is equivalent to 76% of the closed form clamped-free beam frequency, a constant defined as the frequency knockdown factor. A general conclusion of clamped-free tensioned cable systems is that calculating the fundamental frequency using a simple distributed mass approach will always over predict the frequency by 30%. Conversely, joining the tensioned cable along the beam length rather than just the two opposing ends will increase the frequency by 30%.

4.3   Array System Fundamental Frequency

The next step is to expand the single beam fundamental frequency relation into a multi-beam system. The guiding assumption is that the multi-beam, solar array structural architecture behaves like an undamped single degree-of-freedom dynamic system of parallel springs. The general fundamental frequency expression for these assumptions is Eq. (33).[76]

$$f = \frac{1}{2\pi}\left(\frac{k}{m}\right)^{1/2} \tag{33}$$

The mass, m, is located at the tip of the spring. It is also known that the spring stiffness of a clamped-free beam in flexure is represented by Eq. (34).

$$k = \frac{3EI}{L^3} \tag{34}$$

A relation has been developed as Eq. (35) that approximates the tip mass in terms of a distributed mass along the beam length using the Raleigh-Ritz energy method.[76]

$$m = 0.24wl \tag{35}$$

The equivalent stiffness of multiple identical beams in parallel is readily expressed through Eq. (36).

$$k_{eq} = k_1 + k_2 + \ldots k_n = nk \tag{36}$$

Substituting Eqns. (34), (35), and (36) into Eq. (33) and adding the frequency knockdown factor produces Eq. (37), an expression for the system fundamental frequency of multiple clamped-free parallel beams joint at the tip, each of identical bending stiffness, *EI*, length, *L*, and linear mass density, *w*.

$$f = \delta \frac{1}{2\pi} \left(\frac{3nEI}{0.24wL^4} \right)^{1/2} \tag{37}$$

This expression is expanded to include the relevant solar array mass terms into Eqn (38).

$$f = \delta \frac{3.536}{2\pi} \left(\frac{nEI}{L_{pb}^4 \left(nw_{pb} + \dfrac{\gamma_b A}{L_{pb}} + \dfrac{w_{sb} A}{L_{pb}^2} \right)} \right)^{1/2} \tag{38}$$

This relation is rearranged in terms of flexure stiffness into Eq. (39). Note that the frequency term represents the array system frequency while the flexure stiffness term is characteristic of a single primary boom.

$$EI = \left(f \frac{2\pi}{3.536\delta} \right)^2 \frac{L_{pb}^4}{n} \left(nw_{pb} + \frac{\gamma_b A}{L_{pb}} + \frac{w_{sb} A}{L_{pb}^2} \right) \tag{39}$$

Eq. (38) is used to predict the fundamental frequency of the solar array system examined herein. This expression combines the boom stiffness effects using the principle

of superposition to represent a system of clamped-free beam-cable structural elements joined at the tip arranged parallel.

4.4   Array Strength

Now that fundamental frequency is known, a relation for array strength is needed. Two assumptions of strength govern this development. First, the most likely structural failure mode is beam flexure strength due to an out-of-plane rectilinear acceleration load on the array. Second, beam failure could occur as either local buckling, crippling, material failure, global buckling, or self-contact. Knowledge of the exact failure mode is not important for model development; it is only necessary to have knowledge of the maximum moment the array must endure and to have knowledge of the tested limit moment of the beam column(s) enduring that load.

The fundamental equation governing inertial loading is developed through first principles. Consider a slender beam cantilevered from the spacecraft bus. A rectilinear acceleration load is applied to a mass-less bus which imparts an inertial load onto the beam. The beam root must react that inertial load with a moment. Examination of the free body and kinetic diagrams of this beam in Figure 26 reveals that the distributed inertial force is represented by Eq. (40) which is a function of the beam distributed mass and the rectilinear acceleration applied at the root.

$$F(x) = m(x)ag \tag{40}$$

The total reaction moment at the root is quantified by Eq. (41) as the integration of the distributed inertial load along the beam length.

$$M = \int_0^L F(x)\,x\,dx = \int_0^L m(x)ag\,x\,dx \tag{41}$$

Assuming an evenly distributed mass, the root moment reduces to Eq. (42),
indicative of a constant distributed inertial load along the beam as expected for a
rectilinearly applied acceleration. Note that rotational root acceleration would yield a
linearly distributed inertial load varying from zero at the root to a maximum at the tip.

$$M = \frac{w(ag)L^2}{2} \tag{42}$$

This expression for the required moment on a single beam is expanded into
Eq.(43) for an arrangement of multiple clamped-free beams in parallel. The mass term,
w, from Eq. (42) represents the total array mass divided among the quantity of primary
booms. And the acceleration term, ag, represents to total array loading in Eq. (42)
therefore is divided by the boom quantity when expanded into Eq.(43). Each boom
carries an equal portion of the inertial mass loading. This leads to an important
application point—the acceleration loading is applied to the entire array model, but the
moment term represents the reaction at each individual primary boom.

$$M = \frac{1}{n}\left(nw_{pb} + \frac{\gamma_b A}{L_{pb}} + \frac{w_{sb} A}{L_{pb}^2} \right) \frac{agL_{pb}^2}{2} \tag{43}$$

This relation is used to represent the maximum design moment of each primary boom
used in the solar array architecture.
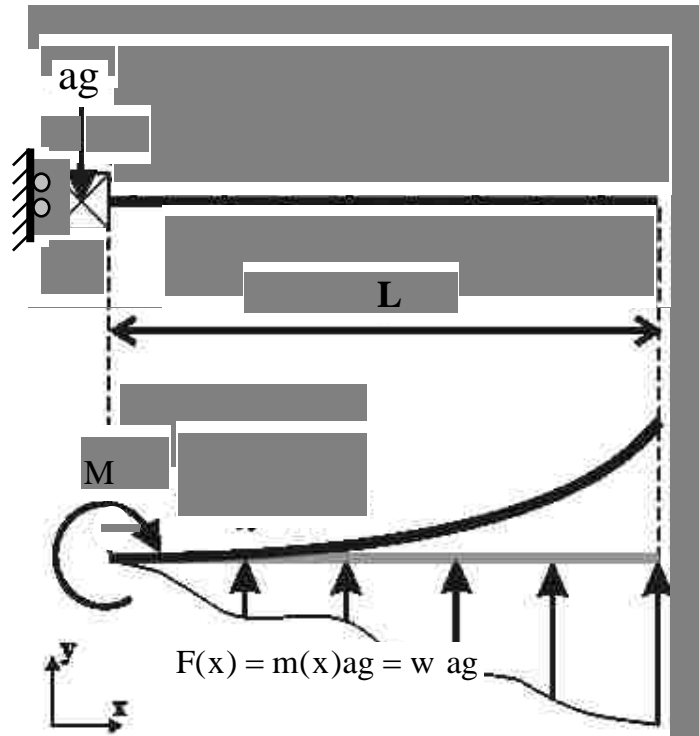
Figure 26. Free-body and kinetic diagrams of a beam with translational acceleration applied at the root.

4.5   Observations

The previous analytic development of cables and slender beams provides a logical framework to evaluate the tensioned blanket solar arrays parameters that affect the fundamental frequency of structural vibration in either bending or torsion modes. Three empirical cases substantiated this analytic framework.

For most practical applications blanket shear tension stiffness effects are secondary to extensional effects therefore a cable is sufficient to approximately represent an array blanket that has an aspect ratio of at least five with the realization that smaller aspect ratios may also be relevant provided the beam torsion stiffness is sufficiently greater than the bending stiffness.

A useful analytical tool is developed to provide a quick assessment of fundamental mode of structural vibration. The special case that does not hold true to this tool is that of a single support boom with a very low ratio of torsion stiffness to bending stiffness. This case is likely to be dominated by blanket shear effects. Nevertheless the present study neglects blanket shear-torsion effects based on the assumption that array designers will avoid torsion modes due to the spacecraft attitude determination and control challenges. Therefore the fundamental mode of vibration for a solar array winglet is approximately captured by the coupled out-of-plane motion of a beam-cable assembly for most practical column types and blanket aspect ratios.

Similarly a large array system of winglets supported by a substantial truss or a composite tube backbone boom is likely to also respond in a bending mode of natural vibration. On the other hand, if the backbone boom is a lightweight truss or if the array system has a very large aspect ratio, the fundamental mode of structural vibration is expected to be torsion.

This chapter also presented a new fundamental frequency solution for a beam-cable assembly that is demonstrated to adequately represent the coupled dynamic behavior of a long, narrow membrane blanket joined to a cantilever beam. Blanket fundamental frequency dynamics are adequately captured by this simple cable solution for tensioned blanket solar array architectures.

Furthermore the coupled beam-string fundamental frequency solution is insensitive to changes over the structural mass fraction range considered, $\beta = 0.01\ to\ 0.5$, but is highly sensitive to changes in the cable tension. This leads to a convenient

optimization of the cable tension with respect to the beam-column critical Euler load. The desired cable tension should be equivalent to 21% of the critical Euler load. The system fundamental frequency of vibration at this optimized tension level is always less than the closed-form clamped-free beam prediction by approximately 30%. This conclusion may be put into practice by applying a knockdown factor $\delta = 0.76$ to the closed-form solution. Further application of this observation is that if the blanket mass is distributed along the beam as is common practice, the fundamental frequency will always be over-predicted by, again, about 30%. Conversely, if the array blanket is, in fact, joined to the beam continuously along the beam length, the frequency will be increased by the same margin.

CHAPTER 5.   CONSTRAINT ANALYSIS SOLUTION

In this chapter the loading equations are combined with the beam efficiency index to form the array weight equation in terms of the requirement constraint terms and the array design terms. The first half of the chapter derives the weight equation, culminating at the apex of numerical complexity—a transcendental equation for array mass that is solved by numerical methods. Constraints are then imposed onto this solution, minimizing array mass and minimizing beam cost. Using these constraints the complex numerical solution of roots is simplified into an approximate symbolic expression for array mass. This simplification process leverages a design of experiments process along with linear and power function regression techniques. Appendix B is provided to supplement to this chapter with greater detail regarding this regression analysis.

5.1   Numerical Model Development

The relations for array frequency and strength, Eqs. (39) and (43) respectively, are first substituted into the beam efficiency index introduced earlier as Eq. (4). The result is Eq. (44), a complete expression for the linear mass density of a single primary boom, a transcendental equation due to the dual location of the beam mass term. Note that numerical values have been substituted for two known constants: the frequency knockdown factor and the gravitational acceleration constant.

$$w_{pb} = \frac{\left(M^2 EI\right)^{1/5}}{\mu}$$

$$w_{pb} = \frac{2.65352}{\mu}\left(\frac{a^2 f^2 L_{pb}{}^2 \left(L_{pb}{}^2 n w_{pb} + A w_{sb} + A L_{pb}\gamma_b\right)^3}{n^3}\right)^{1/5} \tag{44}$$

$$w_{pb} = w_{pb}(\mu, a, f, L, A, n, \gamma_b, w_{sb}, w_{pb})$$

Finally this expression for primary boom mass is substituted into the array weight

equation to form Eq. (45).

$$\gamma = \gamma_{pb} + \gamma_b + \gamma_{sb}$$

$$\gamma = \frac{n w_{pb} L_{pb}}{A} + \gamma_b + \frac{w_{sb}}{L_{pb}} \tag{45}$$

$$\gamma = w_{pb}(\mu, a, f, L, A, n, \gamma_b, w_{sb}, w_{pb})\frac{n L_{pb}}{A} + \gamma_b + \frac{w_{sb}}{L_{pb}}$$

This equation is solved symbolically using the numerical methods available in the

Mathematica$^{©}$ commercial software package.

5.2   Approximation Model Development

The purpose of developing the approximation model is to simplify the weight

equation solution into readily usable metrics that ultimately inform solar array structural

scaling behaviors. This is accomplished by first subjecting the equation to constraints,

minimizing array mass and beam cost. Once the approximation model is developed

symbolic expressions are derived by observing the relative influence of each design

parameter on the objective constraints through a regression analysis.

Table 7 lists each term discretized into a practical range for study. Notice that the

acceleration loading and fundamental frequency terms are combined to form a single

loading term, a simplifying step based on inspection of Eq. (44). Initial observations of the relative influence of parameters reveal that the array areal density term is highly sensitive to small changes in area and length. Therefore these terms were discretized into more steps than the others. A total of 2,430 unique design cases were investigated based on the unique combinations of the seven independent parameters listed in the table.

The relative influence of these terms was explored through an informal design of experiments study. For the seven independent parameters listed in Table 7, the maximum and minimum of each was first considered in constructing a reduced experiment set of 2^7 cases. Each is plotted against the dependent parameter, array areal mass density, using the weight equation previously expressed as Eq. (45).

One observation from these results is the consistent relationship between array mass density and the beam efficiency index. It is clear that a minimum desired value exists beyond which increasing beam efficiency has little effect on reducing areal mass density. Higher beam index values require greater structural hierarchy leading to more complex deployable boom assemblies and larger stowed volumes; therefore the minimum index is preferred. For example, a continuous longeron mast constructed with pultruded S2 glass rods has a moderate beam index of $\mu = 224\ N^{3/5}m^{9/5}/kg$ and has flown successfully many times on-orbit since the 1960's.[22,81] The ATK TriLok® boom is an example of greater hierarchy, a truss of tubes that has not yet been demonstrated on-orbit. The TriLok® has a high beam index of $\mu = 1268\ N^{3/5}m^{9/5}/kg$.[22] But the deployment mechanism is more complex, and the boom does not package as well as the continuous longeron masts. While beams of higher index values correlate to greater mass savings,

they are also typically more costly and may require larger packaged volumes. Array mass

must be minimized but not at the expense of excessive growth in beam efficiency (i.e.,

cost). Both must be simultaneously minimized.

Table 7. Discretized range of design parameters used to define 2,430 unique structural architectures.

		Discretized Range	Units
Objective Constraint			
Areal Mass Density	γ	0 - 10	kg/m^2
Array Performance Constraints			
Loading Term	af	[0.00001, 0.01, 1]	Hz 9.81 m/s^2
Area	A	[10, 60, 200, 600, 2000]	m^2
Primary Boom Properties			
Beam Efficiency Index	μ	1 - 5000	$N^{3/5}m^{9/5}/kg$
Length	L_{pb}	[5, 10, 15, 20, 25, 30]	m
Quantity	n	[1, 2, 10]	--
Blanket Properties			
Areal Mass Density	γ_b	[0.5, 1, 2]	kg/m^2
Spreader Bar Properties			
Linear Mass Density	w_{sb}	[1, 3, 5]	kg/m

A typical example of the relationship between the array areal mass density and the

beam efficiency index is shown in Figure 27. It is clear that minimizing array mass

quickly leads to the trivial solution of infinite beam efficiency. Array mass asymptotes

toward the blanket mass constant value. The minimum desired beam efficiency value is

readily identified in the figure at the "knee in the curve", a location identified where the

slope is negative unity as expressed by Eq. (46).

$$\frac{\gamma_{min} - \gamma_{max}}{\mu_{max} - \mu_{min}} = \frac{-10}{5000} \tag{46}$$

It is important to note that this slope is dependent upon the practical ranges

selected previously in Table 7. Namely the areal mass density range from 0 to 10 kg/m^2

and the beam efficiency index range from 1 to 5000 N$^{3/5}$m$^{9/5}$/kg.
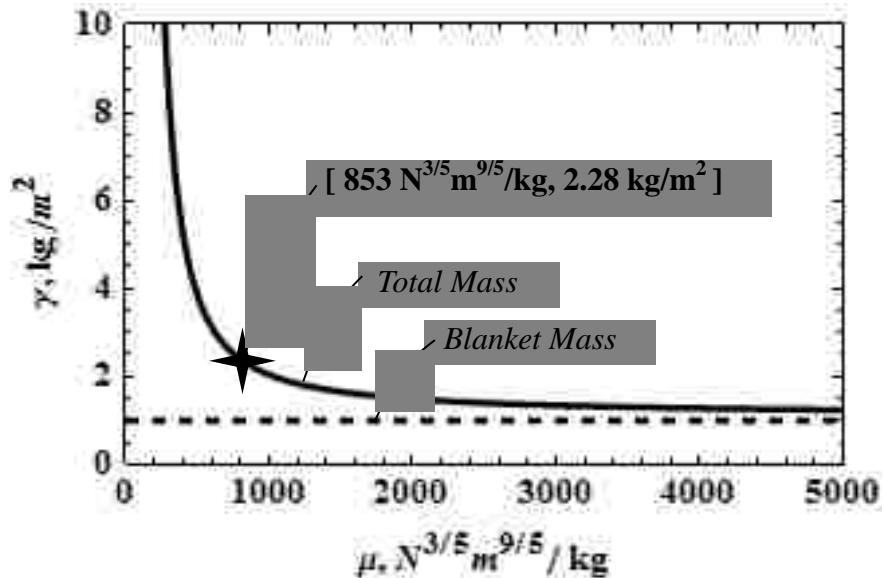
Figure 27. A typical response between the array areal mass density and the beam efficiency index.

This figure represents an example case of a medium sized array, 30 meters long

by 2 meters wide, supported by two booms subjected to a high combined loading,

af = 1 Hz-9.81 m/s^2, with a spreader bar density of *2 kg/m* and a blanket areal density of

1.0 kg/m^2. For this case the minimum desired beam efficiency is predicted to be *μ = 853*

N$^{3/5}$m$^{9/5}$/kg. If a beam of lower efficiency is used then the array performance

requirements may still be met, but a disproportionately large mass penalty will be paid.

On the other hand, choosing a beam with a higher efficiency than the desired will yield

only a small relative reduction in array mass. For example doubling the beam efficiency

92

index from *853 to 1706 N*$^{3/5}$*m*$^{9/5}$*/kg* reduces the total areal mass density by 30% from *2.28*

kg/m^2 to *1.58 kg/m*^{2}, but also increases the hierarchy of the truss leading to more complex

deployment approaches and larger stowed volumes. The minimum desired beam

efficiency index and areal mass density pairs are recorded for each of the 2,430 cases

using this minimization technique. This reduces the number of independent terms from

seven to six.

A summary of the regression analysis process and results is provided herein. A

more complete explanation of the process is provided as Appendix C. This process

explores the relationships between the six independent terms on the two dependent terms,

beam efficiency and array mass, as listed in Table 7. Each combination of variables is

explored and the sensitivity of interactions observed and recorded. Based on these

observations, the independent terms are rank ordered according to relative influence on

beam efficiency (and by association array mass). Reduced sets of the most sensitive

variable combinations are compared and approximately quantified. These relations are

then reassembled into an approximation model of the array architecture.

The sensitivity study begins with one area case, *A = 2000 m*^{2}. Through empirical

examination, a linear relationship is discovered between the terms μ and L_{pb}. This linear

relationship is highly sensitive to changes in the loading term, *af*, mildly sensitive to

blanket density, γ_b, and boom quantity, *n*, and mostly insensitive to changes in w_{sb}. This

relationship is conveniently approximated as Eq. (47) where the constants are further

defined by Eqns. (48) and (49). The coefficient of determination, R^2, between the

numerical model data and the regression fit is calculated as the measure of fit goodness.

The coefficient of determination is calculated as the average of the squared differences between the regression fit and the numerical model data.

$$\mu \approx c_1 L_{pb}; R^2 = 0.995 \tag{47}$$

$$c_1 \approx c_2 (af)^{0.215}; R^2 \geq 0.999 \tag{48}$$

$$c_2 \approx c_3 n^{0.231}; R^2 \geq 0.999 \tag{49}$$

$$c_3 \approx 9.823 \gamma_b^{0.176}; R^2 \geq 0.995 \tag{50}$$

Substitution of Eqns. (48), (49), (50) into (47) produces an approximate expression for the beam efficiency index for one array area, $A = 2000 \ m^2$.

$$\mu_{A=2000} \approx 9.823 L_{pb} (af)^{0.216} n^{0.231} \gamma_b^{0.176} \tag{51}$$

This expression is then expanded into a form that represents the behavior of all six array areas through further regression. The difference between the approximation model and the numerical model is captured by Eq. (52) followed by the regression fit for this expression as Eq. (53).

$$\mu_{numerical} \approx c_4 \mu_{approximation} \tag{52}$$

$$c_4 \approx \frac{6.450}{A^{0.245}}; R^2 \geq 0.98 \tag{53}$$

Equation (51) and (53) are substituted into Eq. (52) to form Eq. (54), a general form that approximately represents the minimum desired beam index value for all the solar array architectures considered within the full parametric space. It is noteworthy that the spreader bar mass term does not appear in this expression, indicating that the mass contribution of that component does not appreciably affect the primary boom mass scaling.

94

$$\mu \approx 63.358 \frac{(af)^{0.216}}{A^{0.245}} L_{pb} n^{0.231} \gamma_b^{0.176} \tag{54}$$

This expression for the beam index is also useful for approximating the array areal density since it is directly related to beam mass. Eq. (55) is readily developed by performing a power regression on the 2,430 data points between the analytic model and the approximation model.

$$\gamma_{pb} \approx 0.0024(\mu)^{0.923}; R^2 \geq 0.998 \tag{55}$$

This expression is then substituted into the weight equation to form Eq. (56), an approximate symbolic representation of the transcendental weight equation expressed previously as Eq. (45).

$$\gamma = \gamma_{pb} + \gamma_b + \gamma_{sb}$$

$$\gamma \approx 0.0024 \left(63.358 \frac{(af)^{0.216}}{A^{0.245}} L_{pb} n^{0.231} \gamma_b^{0.176} \right)^{0.923} + \gamma_b + \frac{w_{sb}}{L_{pb}} \tag{56}$$

This expression represents an approximation of the array areal mass density given that the beam(s) used to support the array are characterized by the minimum desired beam efficiency index described by Eq. (54).

This approximate relation for array mass is compared to the numerical model solution from Eq. (45) to provide a statistical evaluation of the goodness of fit. Figure 28 provides a visualization of the fit. The coefficient of determination between the two models is $R^2 = 0.00247 \ kg^2/m^4$; the standard deviation is $\sigma = 0.04883 \ kg/m^2$; the maximum deviation is $0.1809 \ kg/m^2$; and the minimum deviation is $-0.2161 \ kg/m^2$ as listed on the figure. This fit provides strong confidence that the approximation model adequately captures the structural behavior of a tensioned blanket solar array system with

similar minimization of array mass and beam efficiency (i.e., cost) as the objective

functions to be minimized. Only a lengthy root-based solution was available prior to

development of the approximation model, highlighting the value of a simple but

reasonably accurate approximate solution.

The chart contains the following annotations:

$R^2 = 0.00102\ kg^2/m^4$

$\sigma = 0.03194\ kg/m^2$

$Maximum\ Deviation = 0.1862\ kg/m^2$

$Minimum\ Deviation = -0.1335\ kg/m^2$

$Mean\ Deviation = 0.0040\ kg/m^2$

Y-axis: **Numerical Model Areal Mass Density, γ**

X-axis: **Approximation Model Areal Mass Density,**

$$\gamma \approx 0.0024\ [63.358\ (af)^{0.216}\ n^{0.231}\ L_{pb}/A^{0.245}\ \gamma_b^{0.176}]^{0.923} + \gamma_b + w_{sb}/L_{pb}$$
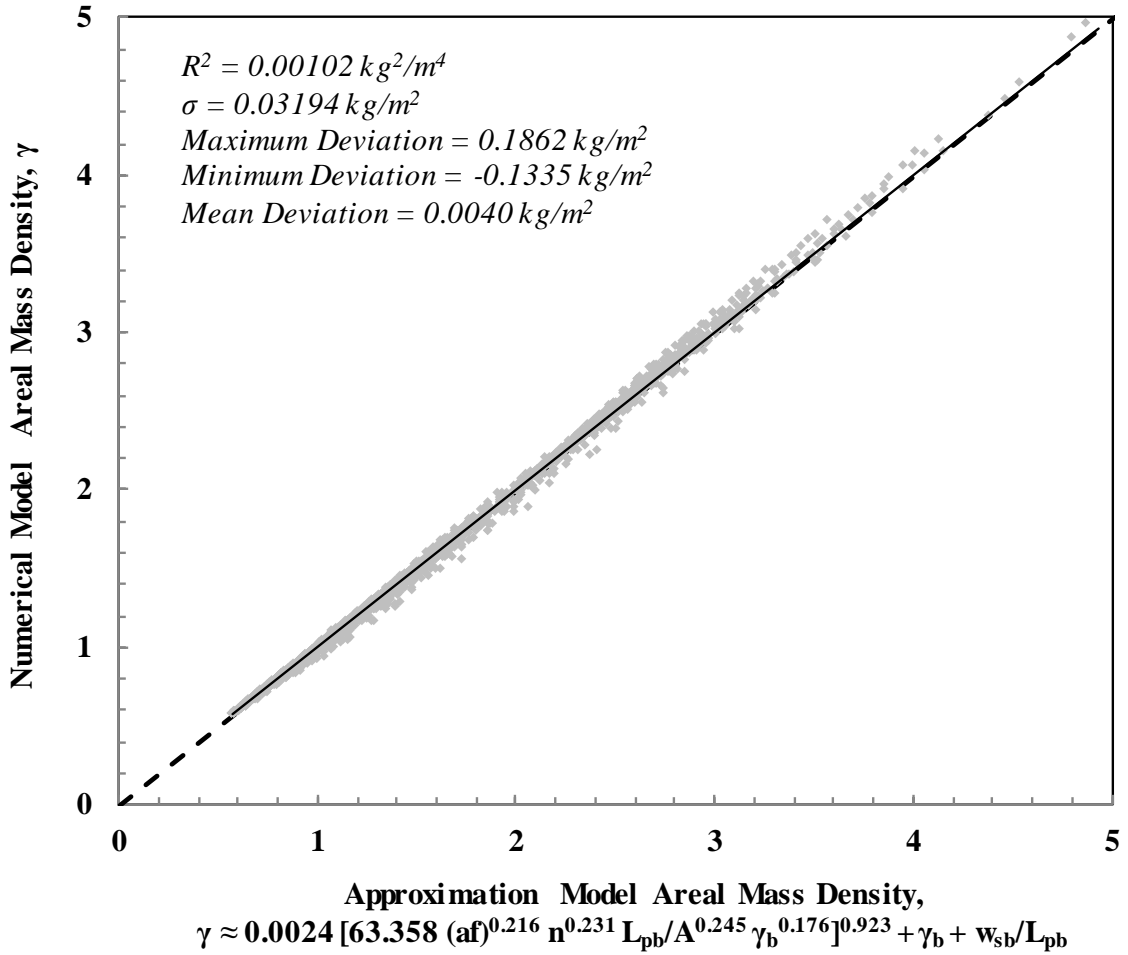
Figure 28. The approximation model areal mass density data is compared to the numerical model to show fit goodness.

5.3 Observations

The constraint analysis process used in this chapter successfully distills a complex numerical solution for solar array mass into an approximation model that is recognizable and of adequate accuracy and simplicity. The outcome is the ability to readily compare scaling effects of rectangular tensioned blanket solar array architectures.

CHAPTER 6.   RESULTS

6.1   Metrics Development

Now that the validity of the approximation model has been established, practical

metrics are extracted and used to enlighten the understanding of scaling rectangular

tensioned blanket solar arrays. First, the constant is dropped from Eq. (54) and the

expression is separated into two terms of influence: the requirements parameter and the

architecture parameter expressed as Eqns. (57) and (58) respectively.

$$\eta_r = \frac{(af)^{0.216}}{A^{0.245}} \qquad (57)$$

$$\eta_a = L_{pb} n^{0.231} \gamma_b^{0.176} \qquad (58)$$

The unusual powers related to these terms are a result of the regression techniques used

to generate this approximation model. The requirements parameter terms are grouped

according to what a mission planner would typically dictate to an array designer:

maximum acceleration loading, minimum fundamental frequency, and minimum power

production (i.e., deployed area). The architecture parameter includes terms usually

available for manipulation by the array designer: array length, quantity of beam-column

supports, and blanket areal mass density.

The requirements and architecture parameters are recombined to form the array

scaling parameter expressed as Eq. (59).

$$\eta = \eta_r \eta_a$$

$$\eta = \frac{(af)^{0.216}}{A^{0.245}} L_{pb} n^{0.231} \gamma_b^{0.176}$$

<div align="right">(59)</div>

The scaling parameter quantifies the relative penalty of scaling the array. When comparing two arrays with the same scaling parameter, by definition both require the same beam performance (i.e., beam efficiency index) to maintain a low areal mass density. As an example, increasing the acceleration loading and fundamental frequency requirements translates into the need for higher performance support columns. If the frequency or acceleration requirement doubles, the required beam efficiency index increases by a factor of 1.16. Similarly if the blanket density doubles, the required beam performance increases by a factor of 1.13.

The column affects array scaling as well. Doubling the length of the array for a given area requires doubling the beam efficiency index. Whereas doubling the number of primary booms increases the beam efficiency requirement of each boom by only a factor of 1.17. Therefore the shortest array with the fewest number of booms always provides the most mass efficient architecture, but if forced to choose between reducing length and reducing boom quantity, the length will have a much greater positive impact on array mass and cost.

It is also clear from this parameter that the most mass efficient means to grow the array area, and thus power production, is by increasing the blanket width rather than the length. In fact if all other terms are constant, increasing the array width actually decreases the overall areal mass density. This is explained by considering that only

blanket areal mass density is being added without the need for additional boom length (i.e., mass).

Of course, design practice informs us that as the blanket width grows so does the mass of the spreader bar and blanket storage box. But this additional mass growth is a secondary effect when compared to the mass and structural performance penalty of growing length of the primary support boom. Admittedly, the spreader bar has a considerable mass impact on extremely large aspect ratio arrays. However blankets with aspect ratios greater than one are not likely to be implemented in practice due to the practical challenges of construction. Even an aspect ratio of one provides the opportunity for assembling multiple long, narrow blankets to a pair of foldable, low mass spreader bars, joined to a single beam-column support. The principle holds true that short, wide array segments are always more mass efficient than those that are long and narrow.

Figure 29 provides a visualization of the relationship between the beam efficiency index and the array scaling parameter. As the array scaling parameter increases, beams of greater performance are needed to maintain a reasonably low areal mass density. As such the penalty parameter may be considered a measure of scaling penalty. As a specific design case moves upward and leftward on the figure, some array mass efficiencies will be realized but at an increasingly high beam efficiency growth. As the beam efficiency index grows, the structural hierarchy of that beam must also increase leading to more complex deployment mechanisms and larger stowed volume geometric forms and higher cost. For example, doubling the beam efficiency from this baseline yields a 30% reduction in array mass, and this relationship continues asymptotically such that as the

beam efficiency index approaches infinity as the beam mass approaches zero, leaving the array mass as only the sum of the blanket and spreader bar.
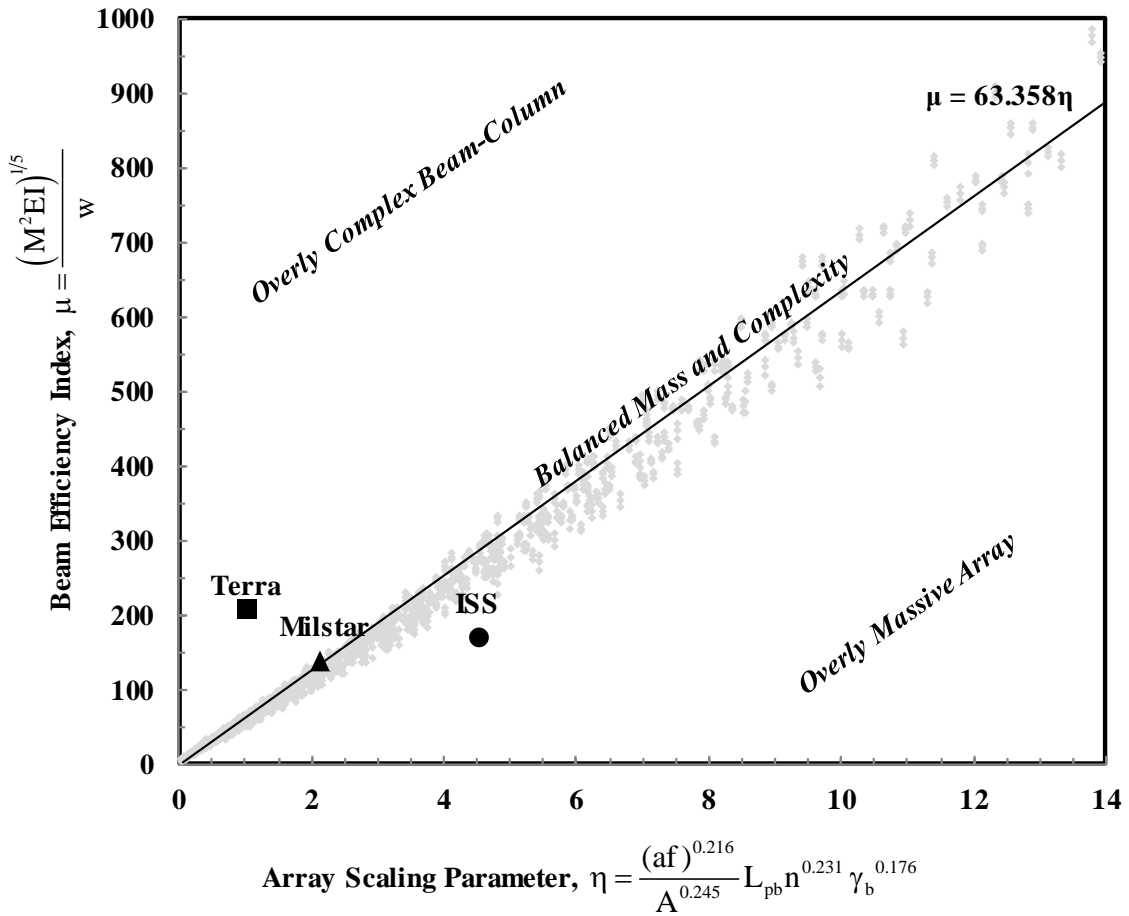
Figure 29. The beam efficiency index is related to the solar array scaling parameter.

The baseline curve represents simultaneous minimization of array mass and beam efficiency. Increases in beam efficiency into the upper left-hand quadrant yield minimal reductions in array mass. On the other hand, array designs that move downward and rightward in Figure 29 gain weight at an increasingly disproportionate pace when compared to the beam efficiency index. Designs in this quadrant will be very massive

but may have the opportunity to save some costs by implementing low-hierarchy beam architectures.

While the extreme corners of both quadrants of Figure 29 should be avoided, moving below the baseline is especially undesirable. Moving above the baseline may be preferred in unique cases where the gains in beam efficiency are achieved at a low monetary cost or if an array of extremely high mass efficiency is needed to meet unusual mission requirements.

Three heritage array systems are readily compared using this scaling parameter. Table 8 lists the specifications for each example considered: Terra, Milstar, and ISS. Figure 29 shows that the Milstar array lies closely to the baseline while the ISS array falls just below and Terra just above. Milstar uses a continuous longeron mast to meet a light loading requirement while the ISS uses an articulated truss to meet a relatively severe loading requirement. The ISS array also has the additional requirement of retractability, likely requiring additional design features that diminish structural performance. The Terra spacecraft array on the other hand pushes up into the very high mass efficiency range due to relatively short, 8.92 meters, but wide, 5.08 meters, aspect ratio and the efficient continuous longeron mast used $\mu = 189\ N^{3/5}m^{9/5}/\,kg$.

Two additional arrays are represented in Table 8, MegaROSA[10] (Roll Out Solar Array) and MegaFlex[14,15]. Both are ground prototype systems but are different in their geometric form. MegaROSA is a rectangular architecture that fits within the assumptions of the present study while MegaFlex is circular in form, constructed from a series of spars arranged radially with blanket gores attached continuously along the edges of these spars.

The MegaROSA prototype is included to show how an alternative dual-column architecture compares to a heritage single-column system. The Mega ROSA data is provided courtesy of Mr. Steve White, Deployable Space Systems, Inc., Goleta, CA. Notice the similarities and differences between MegaROSA and Milstar. Both have a similar boom length and loading requirement, but MegaROSA has twice the quantity of booms and almost twice the deployed area. The mass penalty for using two columns instead of one is evident by the higher scaling parameter: $\eta = 2.39$ for MegaROSA and $\eta = 2.14$ for Milstar. However the MegaROSA architecture makes up for that penalty with a lighter blanket and lighter spreader bar. And since the MegaROSA architecture is 70% wider than Milstar, more area is available for power conversion.

Recall that increasing area by growing the width is much more mass efficient than growing the length. Since no beam efficiency index is available for the MegaROSA columns, it is not possible to plot this example on Figure 29. However, Eq. (54) provides a means of estimating the minimum optimum beam efficiency to be $\mu = 151$. Ultimately ROSA shows close similarity to Milstar in areal mass density performance despite the use of two columns instead of one and despite almost twice the deployed area. Ultimate selection of one architecture over the other in practice would depend upon additional subjective considerations such as the projected cost, mechanical complexity, and reliability of the deployment as well as the packaged volume penalty and packaged form factor.

The MegaFlex array is listed to show the performance of an alternative geometric form. The MegaFlex data is provided courtesy of Mr. Mike McEachen, ATK Space

Systems, Goleta, CA. Since the scaling parameter has been developed for the rectangular

form it is not appropriately used to compare the MegaFlex prototype to MegaROSA.

Nevertheless, a comparison of performance specifications is informative. MegaROSA

and MegaFlex have both been sized for similar missions; the deployed area and loading

requirements are nearly identical. MegaFlex was sized with ten radial spars while

MegaRosa uses two primary booms.   The mass density of each architecture was

separated into a cantilevered mass and a root mass where the cantilever mass includes the

primary booms or spars, blanket or gores, and spreader bar or tip mandrel if used. This

cantilever mass was separated due to the high contribution toward structural sizing and

thus fundamental frequency and strength. The root mass on the other hand includes the

root structure known as the pallet or the panel in addition to the root mechanisms such as

deployment motors, hub assemblies, and restraint devices.

Notice that the mass density performance is very similar between the two

architectures. MegaROSA has a slightly higher cantilever mass density of $\gamma = 1.29 \ kg/m^2$

compared to $\gamma_r = 1.16 \ kg/m^2$ for MegaFlex. But MegaFlex has a higher root mass density

of $\gamma_r = 0.593 \ kg/m^2$ compared to $\gamma_r = 0.105 \ kg/m^2$ for MegaROSA. The root mass density

terms are normalized against the deployed area for ease of comparison.

Table 8. Design specifications and scaling metrics for three heritage and two ground prototypes.

		Terra	Milstar	ISS	MegaROSA prototype	MegaFlex prototype	Units
Rectangular (R) / Circular (C)		R	R	R	R	C	
Requirements							
Deployed PV Area	A	45.3	44.0	301	74.3	76.5	m²
Acceleration Load	a	0.015	0.050	–	0.060	0.100	9.81 m/s²
Fundamental Frequency	f	0.16	0.16	–	0.21	0.10	Hz
Loading Term	a f	0.0024	0.0081	0.0590	0.0126	0.0100	Hz 9.81 m/s²
Size							
Length	L_{pb}	8.95	14.8	32.9	14.9	5.70	m
Width	W	5.06	2.97	9.15	4.99	–	m
Boom Quantity	n	1	1	1	2	10	–
Beam Performance Index	μ	189	137	153	–	–	$N^{3/5} m^{9/5}/kg$
Cantilever Mass Density	γ	2.06	1.52	1.78	1.29	1.16	kg/m²
Primary Booms	γ_{pb}	0.077	0.102	0.463	0.135	0.191	kg/m²
Blanket	γ_b	1.66	1.22	1.20	1.07	0.967	kg/m²
Spreader Bar	γ_{sb}	0.323	0.203	0.121	0.083	0	kg/m²
Root Mass Density	γ_r	1.09	0.857	0.574	0.172	0.593	kg/m²
Metrics							
Predicted Cantilever Mass	γ	1.81	1.46	1.65	1.32	1.75	kg/m²
% Error	–	-12%	-4%	-7%	3%	–	–
Cantilever Mass Fraction	β	0.037	0.067	0.260	0.105	0.165	kg/kg
Array Scaling Parameter	η	1.04	2.14	4.55	2.39	–	$m^{0.374} kg^{0.176}/s^{0.648}$
Requirements Param.	η_r	0.107	0.140	0.134	0.135	–	$1/(m^{0.274} s^{0.648})$
Architecture Parameter	η_s	9.78	15.3	34.0	17.7	–	$m^{0.648} kg^{0.176}$
Array Scaling Index	κ	0.508	1.41	2.55	1.86	–	$m^{2.374}/(kg^{0.824} s^{0.648})$

A second metric is developed by dividing the array scaling parameter, Eq. (59), by the total areal mass density. The result is the array scaling index listed as Eq. (60).

$$\kappa = (af)^{0.216}\, n^{0.231} L_{pb}\, A^{0.755}\, \frac{\gamma_b^{0.176}}{m} \tag{60}$$

While the previously defined scaling parameter is useful for comparing structural architecture options on an even playing field, the scaling index serves a slightly different purpose as it informs mission planners how the array requirements—acceleration loading, fundamental frequency, and array area—affect the array mass. This index is useful during the early stages of mission planning when the array requirements are being traded against other subsystem requirements within the overall mission concept, and the array architecture is unknown.

The scaling index is separated into two indices for clarity. First the acceleration and fundamental frequency terms form the loading index given as Eqn (61).

$$\kappa_1 = n^{0.231} L_{pb}\, A^{0.755}\, \frac{\gamma_b^{0.176}}{m} \tag{61}$$

This index is plotted in Figure 30 for three loading requirement values. This figure shows that as the loading index grows, the support structure mass must grow proportionally in order to meet the growing strength and stiffness demand of a larger, longer, more massive array. This figure also shows that the rise in structural mass occurs more sharply for higher loaded arrays and more gradually for lesser loaded arrays. The scaling index is modified again, this time the area term removed to form the power index shown as Eq. (62).

$$\kappa_p = (af)^{0.216} \, n^{0.231} L_{pb} \frac{\gamma_b^{0.176}}{m} \qquad\qquad (62)$$

The power index is plotted in Figure 31 to show the relative mass penalty of five different array sizes. The effect is similar to that shown by the loading index where the larger the area, the steeper the growth in structural mass.
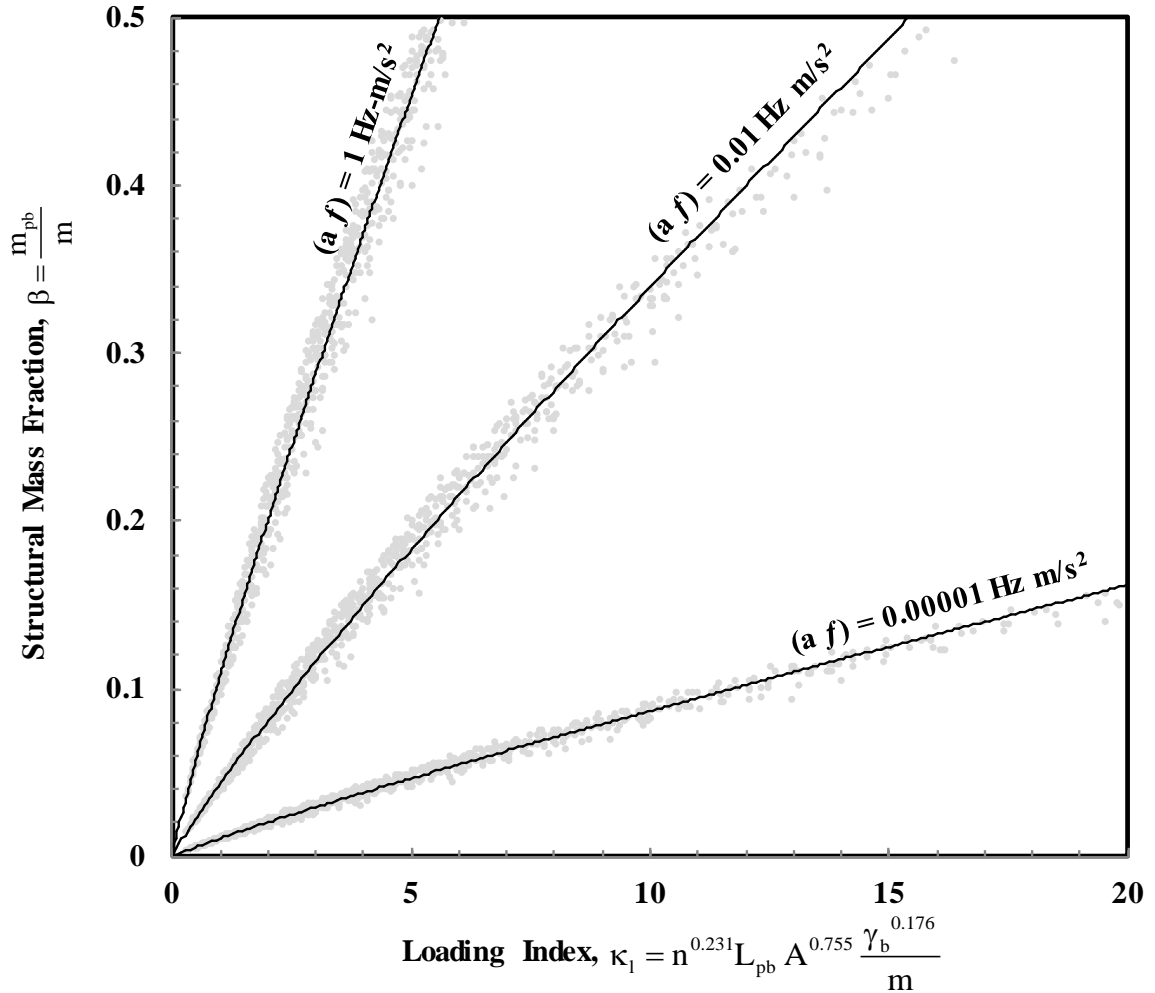
Figure 30. *Loading index related to array structural mass fraction for three acceleration and frequency values.*
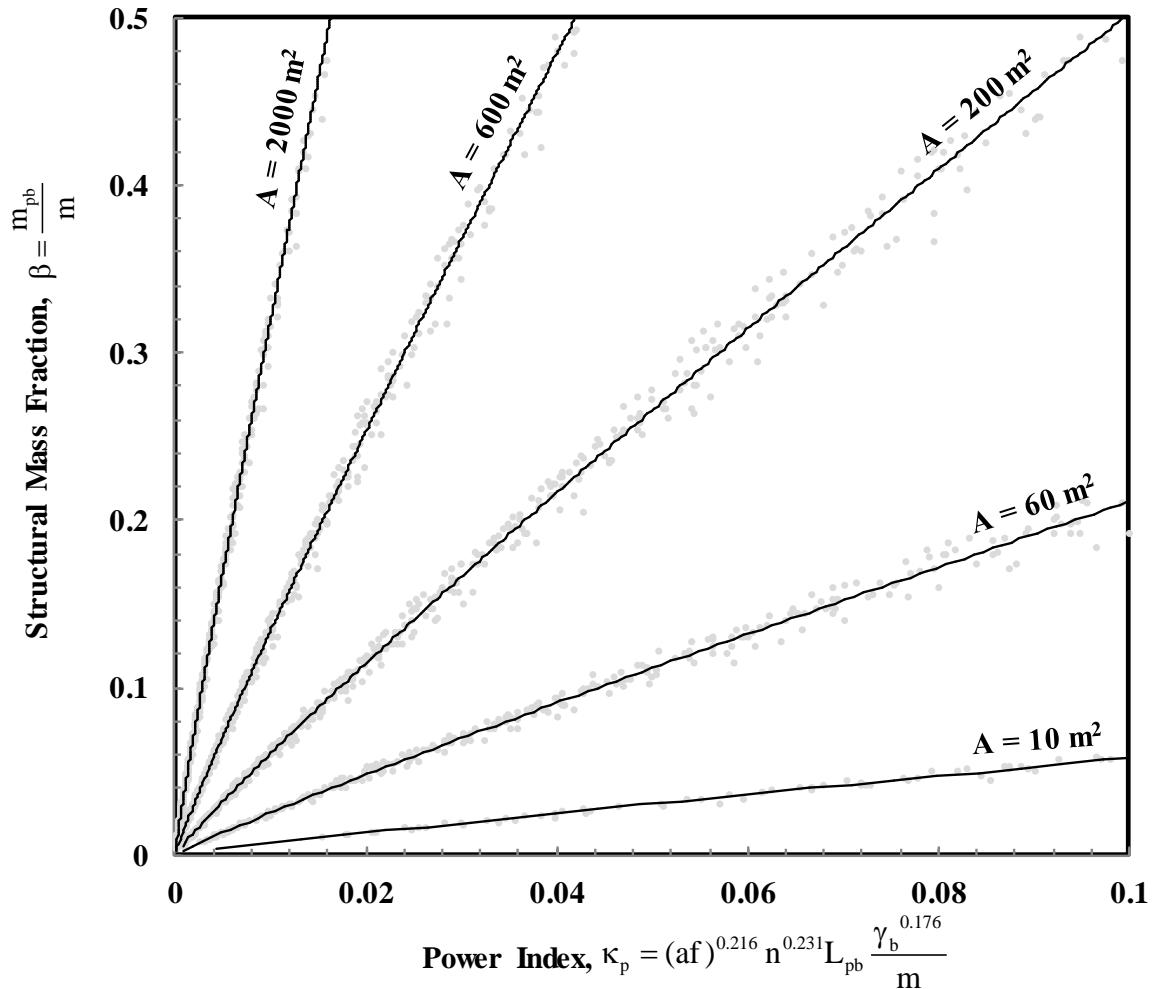
Figure 31. Power index related to structural mass fraction for a wide range of array areas to show the relative structural mass penalty of increasing the loading, length, blanket mass, and boom quantity.

One conclusion from these two figures is that the structural mass of very large, highly loaded arrays grows much more quickly than small area, lightly loaded arrays such as those currently in use today. The scaling index is a penalty quantity that must be minimized in order to minimize array mass. Boom length is the most influential variable in the scaling index that should be aggressively minimized.
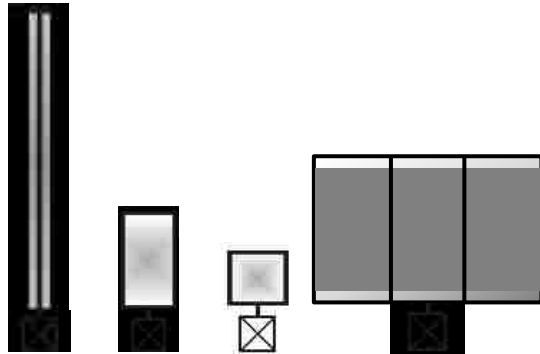
General conclusions may be drawn from the scaling parameter and the scaling index. Both metrics handsomely reward reductions in array length for a constantly held area, and these both prefer fewer primary booms. Short, wide arrays supported by a single column are always more mass efficient than long, narrow arrays supported by multiple columns for a given array area, strength, and frequency requirement. Three terms have a similar inverse effect on beam efficiency: array loading, boom quantity, and blanket areal mass density. Each term scales according to a factor of about two-fifths.

Reducing the blanket areal density has a direct additive effect on solar array mass according to Eq. (59). In fact the blanket mass remains the single most significant contributor to the total mass of the array (i.e., for this study, the mass of non-cantilevered components were neglected: boom deployment mechanism, blanket containment pallet, yoke structure, and Solar Array Drive Assembly). When considering methods to reduce this mass, it is important to remember that the vast majority of this mass comes from the photovoltaic cell. The blanket substrate is typically a low-mass, thin membrane polymer or high-strength, open weave fabric. The past 30 years of advancements in blanket construction techniques and materials have yielded little improvement in total blanket areal mass density, and the future does not currently show much promise in this area. However, small reductions in cell mass would yield a sizable reduction in array mass. Perhaps advancements in cell construction techniques will yield mass improvements in the years to come.

6.2 Practical Application

Four practical example cases are presented to further demonstrate the utility of the scaling metrics. Table 9 lists the array requirements, design parameters, and resulting metrics for each case.

Table 9. Example cases to represent solar array scaling effects.

		Case 1	Case 2	Case 3	Case 4	Units
Requirements Input						
Wing Power (BOL)	–	15	15	15	100	kW
PV Cell Efficiency	–	29.5	29.5	33	33	%
Wing Area	A	60	60	52	345	m^2
Acceleration Load	a	0.1	0.1	0.1	0.1	$9.81 \ m/s^2$
Fundamental Frequency	f	0.2	0.2	0.2	0.2	Hz
Size Input						
Length	L_{pb}	30	10	8.7	15	m
Width	W	2	6	6	23	m
Boom Quantity	n	1	2	2	4	–
Blanket Mass Density	γ_b	1.5	1.5	1.5	1.5	kg/m^2
Spreader Bar Mass	w_{sb}	1	1	1	3	kg/m
Results						
Array Scaling Parameter	η	5.08	1.99	1.79	2.28	$m^{0.374} \ kg^{0.176} / s^{0.648}$
Requirements Parameter	η_r	0.158	0.158	0.163	0.103	$1 / (m^{0.274} \ s^{0.648})$
Architecture Parameter	η_s	32.2	12.6	11.0	22.2	$m^{0.648} \ kg^{0.176}$
Array Scaling Index	κ	2.50	1.10	0.99	1.18	$m^{2.374} / (kg^{0.824} \ s^{0.648})$
Minimum Beam Efficiency	μ	322	126	113	144	$N^{3/5} m^{9/5} / kg$
Wing Mass	m	122	108	94	668	kg
Mass Reduction from Case 1	–	–	11%	23%	–	–

The first three cases represent a communications spacecraft that requires 30 kW of power at the beginning of service life. State of practice triple junction PV cells will be used. According to Table 2 these cells generate 250 W/m^2; therefore the total required deployed area is 120 m^2, 60 m^2 for each of two wings. The maximum acceleration load expected on the deployed array is 0.1 g, and the minimum required fundamental frequency is 0.2 Hz. From these terms, the requirements parameter is calculated using Eq. (57) to be $\eta_r = 0.158$.

Now that requirements have been established, four different structural architectures are considered. The first case is constructed with a single blanket 30 meters long by 2 meters wide, supported by a single beam-column. From Table 2, blanket mass density is taken to be $\gamma_b = 1.5 \ kg/m^2$. The architecture parameter is then calculated from Eq. (58) to be $\eta_s = 32.2$. The product of the requirements and architecture parameters becomes the scaling parameter, $\eta = 5.08$. This value, when plotted on Figure 29, correlates to a beam efficiency index of $\mu = 322$. The array mass is estimated from Eq. (56) to be $m = 122 \ kg$.

The second case consists of the same blanket area as the first but is shorter, 10 meters long by 6 meters wide, and is supported by two beam-columns instead of one. Again, the blanket mass is 1.5 kg/m^2. The architecture parameter for this case is $\eta_s = 12.6$, and the scaling parameter is $\eta = 1.99$. The beam efficiency index is less than half that of the first case, $\mu = 126$, and the total mass is reduced to $m = 108 \ kg$. Interestingly, the penalty paid for using two columns is easily overcome by the benefits of a shorter,

wider aspect ratio. The payoff of the reduced beam index is reduced structural hierarchy and reduced cost.

The third case considers upgraded PV cells from the XTJ/ZTJ state of practice to an IMM cell type, yielding a boost in conversion efficiency from 29.5% to 33%. This upgrade allows a smaller deployed area, 52 m^2, per wing since the areal power density has increased to 290 W/m^2. The requirements parameter is recalculated to be $\eta_r = 0.163$. Keeping the width and boom quantities as defined previously as case 2 but reducing the array length to 8.7 meters, the architecture parameter reduces to $\eta_s = 11.0$, and the scaling parameter reduces to $\eta = 1.79$. The beam efficiency index for case 3 is $\mu = 113$ and the total mass is $m = 94$ kg; both are slightly lower than those of case 2 by 10% and 13% respectively. The beam efficiency index reduction is a direct result of reducing the array area length from 10 meters to 8.7 meters, and the mass reduction is a result of reducing the area from 60 m^2 to 52 m^2.

A fourth case examines the mass and cost penalties of scaling to higher power arrays. Consider a 400 kW array where each wing is split into two 100 kW winglets, joined by a backbone boom. Assuming 33% efficient IMM cells, the area of each winglet needs to be 345 m^2. The strength and frequency requirements are 0.1 g's and 0.2 Hz respectively, yielding a requirements parameter of $\eta_r = 0.103$. Blanket mass is again assumed to be $\gamma_b = 1.5$ kg/m^2. The length of each winglet is 15 meters and the width is 23 meters. Four primary booms are used to support the blanket therefore the architecture parameter is $\eta_s = 22.2$. The scaling parameter is $\eta = 2.28$, and the minimum beam efficiency index is $\mu = 144$. The winglet mass is estimated to be 668 kg. Estimating the

200 kW wing mass requires an estimation of backbone boom mass, primary boom

deployment mechanisms mass, and blanket box mass. Each of these is lumped into a

conservative backbone mass of 10 kg/m. The total wing mass is 1566 kg, and the total

effective areal mass density is $\gamma = 2.27\ kg/m^2$. Note that for this example, the blanket

mass comprises 66% of the total and the structure and mechanism is 34% of the total. It

would be difficult to improve this mass performance. For an array of this size, the

packaged volume performance and deployment reliability are likely to be far more

important considerations than mass efficiency.

The scaling index is useful when power or loading requirements are not well

defined, but perhaps the array mass limit is known such as during mission concept

planning. Figure 30 and Figure 31 show the relative mass scaling of different array

architectures given a constant total mass requirement.

Before concluding, some comments are offered regarding packaging performance.

Packaging is an important consideration for evaluation of solar array architectures, but it

is difficult to quantify generally and fairly across multiple architectures. The boom

quantity and efficiency index both likely have a direct relation to packaged volume, but

detailed design information of deployment mechanisms is needed in order to quantify

these effects. Blanket packaged volume on the other hand is readily quantified with

knowledge of deployed area. Additional work is needed to quantify the relationship

between structural performance and packaging performance.

CHAPTER 7.   CONCLUSIONS

7.1   Summary

Simplified structural metrics have been successfully established for rectangular flexible blanket photovoltaic solar array architectures. This approach considers the solar array structure as a *system* of beam and tensioned blanket components rather than as a beam *component* with a distributed mass. A structural model was developed using constraint analysis methods, solved using numerical root finding algorithms, and simplified into an approximation model using regression techniques. From this process, an array scaling parameter and an array scaling index emerged.

To support the scaling parameter development, a relation was developed to approximate the fundamental frequency of a clamped-free, beam-cable assembly. It was discovered that the well-known beam-only fundamental frequency of vibration solutions will always over predict the frequency of a distributed mass blanket system by 30%. A more accurate solution is to couple the frequency knockdown factor, $\delta = 0.76$, with the beam-only solution in order to account for the combined effects of the beam and the string. It was established through on-orbit examples and comparison of beam torsion stiffness to bending stiffness ratios that this beam-string relation adequately represents a beam-blanket assembly for the purposes of architecture comparison.

Both the scaling parameter and the scaling index are useful tools for comparing tensioned blanket solar array structural architectures. Both are developed on the basis of minimum array mass and minimum beam efficiency (i.e., cost).

The scaling parameter is useful for comparing structural architecture options on an even playing field. It provides perspective into the source of mass efficiency differences by quantifying the mass effects of different boom architectures. One significant conclusions drawn from this parameter is that short, wide arrays that are supported by a single column are always more mass efficient that long, narrow arrays supported by multiple columns for a given array deployed area, strength and frequency.

The scaling index serves a slightly different purpose as it informs mission planners how the array requirements—acceleration loading, fundamental frequency, and array area—affect the array mass. This index is useful during the early stages of mission planning when the array requirements are being traded against other subsystem requirements within the overall mission concept.

Practical application of the scaling parameter and scaling index were demonstrated. The latest heritage flexible blanket solar array systems were compared using the array scaling parameter and the array scaling index: Terra (EOS-AM) launched in 1999, Milstar constellation first launched in 1994, and the ISS arrays first launched in 2000. A practical range of photovoltaic cell types and corresponding areal power densities were presented to provide a straightforward translation of deployed area to the actual array power production on-orbit. Two prototype array concepts were listed and compared, MegaROSA and MegaFlex.

While these metrics developed herein quantify the mass penalty of scaling a variety of solar array architectures, additional subjective factors must be considered in parallel. For example, the packaged volume and geometric form of the folded array has

strong bearing on the launch vehicle cost and space mission flexibility. Other important

factors include the ease by which the array can be tested on the ground in a simulated

space environment and the ease by which the array structural behavior can be analytically

predicted. The time and manpower required to assemble an array is another important

consideration that requires subjective assessment. Each of these factors ultimately

influences monetary cost.

In closing, these metrics provide practical tools aimed at helping those comparing

structural architectures, those considering mission concepts, and those crafting

technology investment strategies. The ultimate purpose is to help set investment

trajectories on paths that are well-founded on solid structures principles.

7.2 Limitations

It is important to note the intended use of the metrics by also specifying the

limitations for application. The focus of this work is photovoltaic arrays where

dimensional stability is not a driving requirement. Dimensional stability was not

considered as a constraint thus these metrics are not appropriate for precision structural

applications such as antennas and optical apertures. Furthermore, these models are not

intended to serve detailed structural design activities. Detailed part sizing is not

considered. Instead these models represent trends in structural scaling behavior and

should be used early in the concept design process.

7.3 Future Work

A discussion of the limitations of the current work is naturally followed by an

exploration of future possibilities. The present study presents a method for developing

structural scaling metrics for a structural *system*, whereas previous approaches have primarily focused on the structural *component*. Additional system level scaling metrics are needed for other classes of tensioned architectures such as tensioned precision planar antennas and precision transmission optical apertures for both rectangular and radial configurations.

Packaging performance of solar arrays is not considered directly herein but remains an important consideration. It is difficult to quantify generally and fairly across multiple architectures without knowledge of detailed design information of deployment mechanisms. Additional work is needed to quantify the relationship between structural performance and packaging performance for all types of large structural platforms.

Another field ripe for study is the quantification of deployable structures complexity. Structural architecture selection is currently heavily influenced by the *perception* of design complexity. Yet this factor has a profound impact on the monetary cost of analyzing, building, testing, and operating a spacecraft payload. This link between design complexity and cost demands that mechanical complexity be better quantified and tracked especially during the conceptual design phase of the acquisition process. Yet it is at this phase when complexity is most difficult to quantify since no detailed drawings, master equipment lists, or labor estimates are available. Design complexity metrics are needed for deployable structures designers and for the spacecraft design community as a whole.

APPENDICES

APPENDIX A. BEAM-CABLE FINITE ELEMENT ANALYSIS

APPENDIX B. NUMERICAL MODEL MATHEMATICA© CODE

APPENDIX C. REGRESSION TECHNIQUES FOR METRIC DEVELOPMENT

APPENDIX A. BEAM-CABLE FINITE ELEMENT ANALYSIS

A finite element model is created to predict the coupled fundamental frequency response of a beam-cable assembly and is used to develop a relation that approximately represents this response given practical design ranges. The presumption is that the dynamic response of the suspended cable is affected by the motion of the beam to which it is attached and vice versa.

The ABAQUS/Standard[80] commercial finite element analysis code is used to model the beam-cable assembly. Figure 32 shows the model components, illustrating that the tension load in the cable is equivalent to the compressive load in the beam. The beam is constrained in a clamped-free condition where the root is fixed in all 6 degrees-of-freedom (3 rotation and 3 displacement), and the tip is free to rotate and translate in all 6 degrees-of-freedom. The cable is joined to the two opposing beam ends. The tip of the cable follows the displacement motions of the beam tip, and the root of the cable is not allowed to displace due to the fixity of the beam root. While the figure shows the cable deformed for illustrative clarity, the model considers the beam and the cable to be collinear in the unperturbed state.

The structural element options are evaluated based on accuracy in predicting the fundamental frequency and critical buckling load. Six different beam elements and four truss elements are compared to represent the column and the blanket respectively. The FE model predictions of fundamental frequency were compared to closed form solutions for both the beam and blanket shown as Eqs.(63) and (64) respectively.

$$f = \frac{3.516}{2\pi}\left(\frac{EI}{wL^4}\right)^{1/2} \tag{63}$$

$$f = \frac{1}{2L}\left(\frac{T}{w}\right)^{1/2} \tag{64}$$
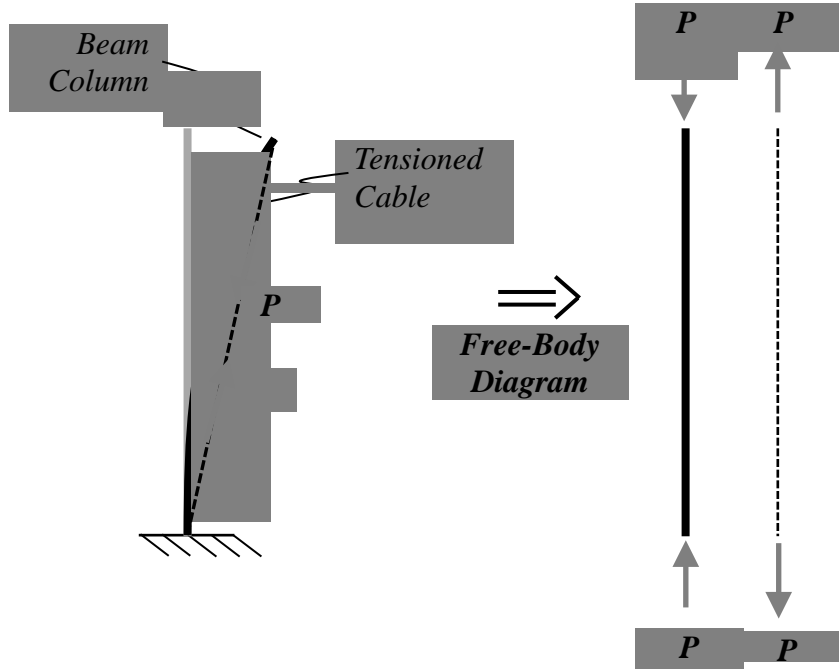
Figure 32. An illustration of the beam-cable assembly shows that the cable tension load, P, is reacted as an equivalent beam compression load, P.

Table 10 lists each element type and the error when compared to the closed form beam fundamental frequency solution from Eq. (63). The first beam element type listed in the table is the linear Timoshenko beam, linear because the shape function and thus stress distribution is linearly interpolated between the two nodes at a single integration point. The quadratic and cubic elements use two and three integration points between nodes respectively, allowing more accurate stress predictions for a given element but at a

computation penalty. Similarly, elements that use three-nodes yield more accurate displacement predictions than two-node elements because the interpolation function is raised to second order. The hybrid formulation adds an additional axial force variable that does not seem to make a difference for the loading scenarios in this study where axial displacement is not substantial.

Euler-Bernoulli is a simpler version of the more general Timoshenko formulation. Timoshenko includes shear deformation effects that cause these elements to be more compliant and thus predict a lower fundamental frequency of vibration than Euler-Bernoulli. This is the reason that the table shows a 4% lower frequency by the Timoshenko beams. The Timoshenko formulation is best used to approximate short, stout beams with appreciable shear deformation. The Euler-Bernoulli formulation on the other hand is best for slender beams where the ratio of diameter to length is less than 1/15 as expected for this space structures application. Furthermore additional integration points are appropriate in this case because transverse loading is expected to cause large bending deformations but not shear deformations. Thus the Cubic Euler-Bernoulli beam element, B33, is selected to be the most suitable for this application.

Table 10. Beam element type comparison reveled B33 to be the most accurate.

Element Type	FEA f, Hz	Closed Form f, Hz	% Error	Element Description
B31	0.53403	0.55959	-4.568%	2-node Linear Timoshenko beam, transverse shear stiffness, stout
B31H	0.53403	0.55959	-4.568%	2-node Linear hybrid Timoshenko beam, transverse shear stiffness and deformation, stout
B32	0.53409	0.55959	-4.557%	3-node Quadratic Timoshenko beam, transverse shear stiffness, stout
B32H	0.53409	0.55959	-4.557%	3-node Quadratic hybrid Timoshenko beam, transverse shear stiffness and deformation allowed, stout
B33	***0.55959***	***0.55959***	***0.000%***	***2-node Cubic Euler-Bernoulli beam, no transverse shear deformation, no warping, slender--dia/length < 1/15, transversely loaded***
B33H	0.55959	0.55959	0.000%	2-node Cubic hybrid Euler-Bernoulli beam, no transverse shear deformation, no warping, slender--dia/length < 1/15, transversely loaded

For the elements that represent the cable, fewer options are available. Four elements are tested in the same manner as previously—linear and quadratic truss elements, each with a standard and hybrid formulation. The fundamental frequency results were compared from a typical tensioned cable model. There was no difference between the four elements therefore the most computationally efficient element was selected, the two-node truss element T3D2. The compressive stiffness was set to zero.

Next a convergence study involving mesh refinement is performed on the coupled beam-cable model using the B33 beam elements and T3D2 truss elements. Fundamental frequency is again used as the figure of merit. Five element lengths were compared on a 1-meter long typical model: 4 cm, 2 cm, 1 cm, 0.5 cm, 0.25 cm. Figure 33 shows that the frequency drops as element length is shortened—finer mesh densities generate more compliant models as expected. The frequency changed by less than one hundredth of a percent from the 1 cm to the 0.5 cm size; therefore 1 cm length is selected. The beam and cable components are therefore each represented by one hundred, equal-length elements.
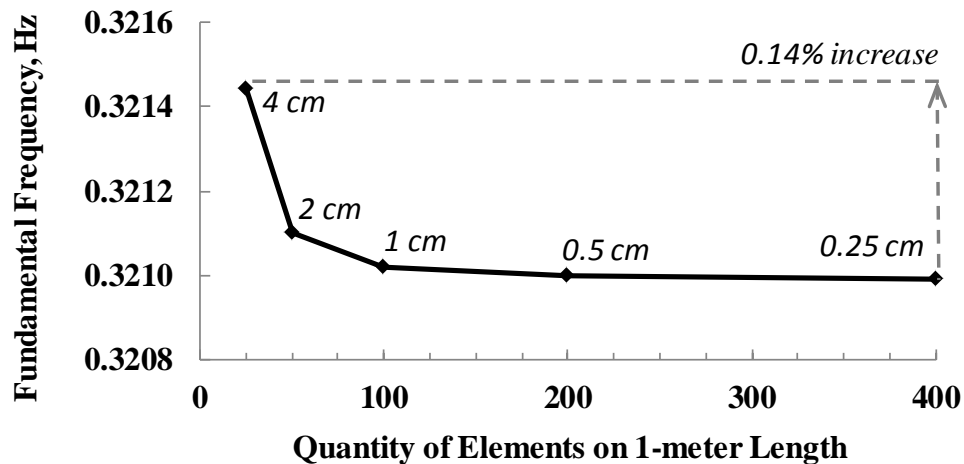
Figure 33. Mesh density analysis shows the 1 cm element size to be more than sufficiently accurate.

The model construction details are shown in Figure 34. The length and material properties are arbitrarily selected for convenience; this is allowable since the model outputs of interest—fundamental frequency, mass, and column compression—are normalized against known baseline values. Absolute values are not important.
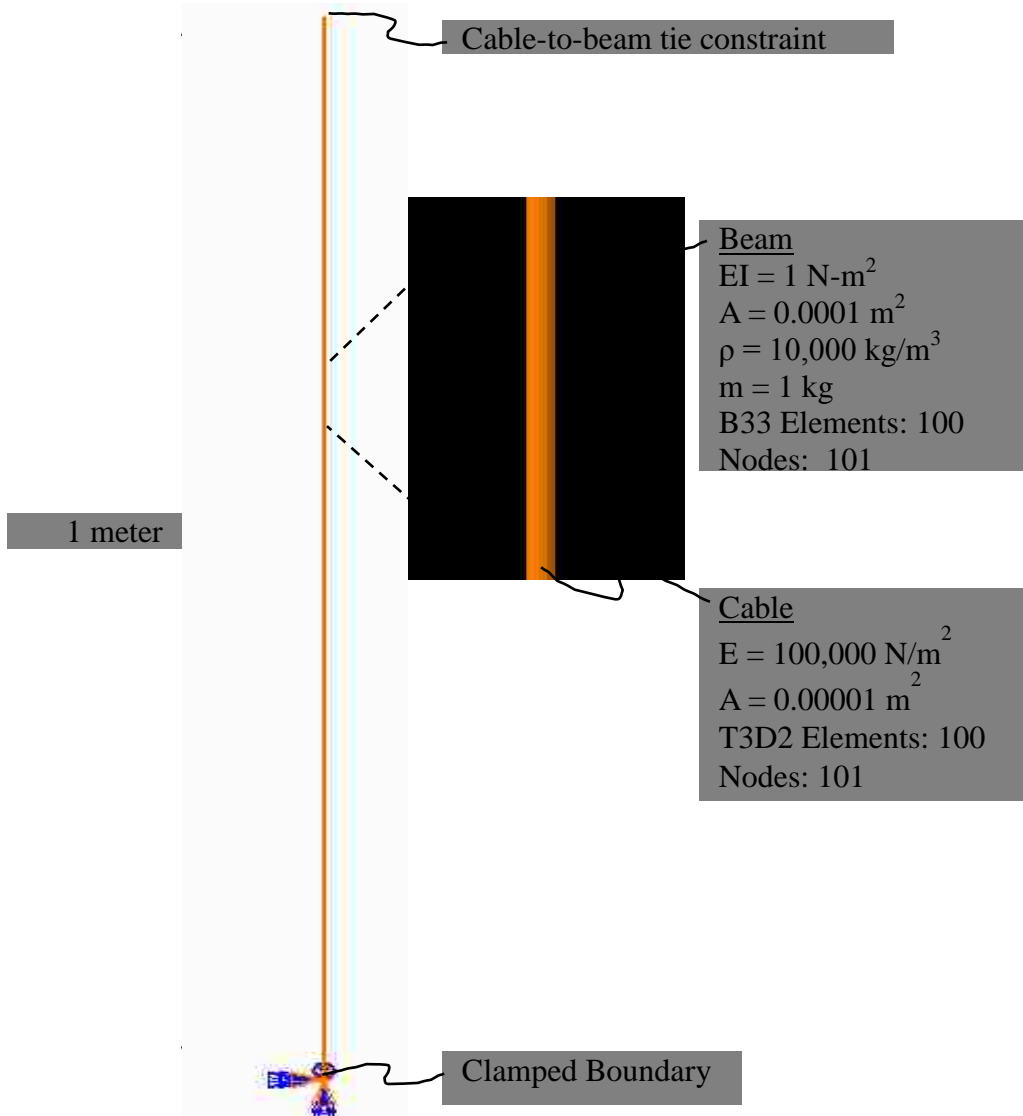
Figure 34. The finite element model represents a beam and a cable joined at two opposing ends.

The model was subjected to a series of parametric cases in order to understand the impact of cable tension and cable mass on the system fundamental frequency. The cable tension is varied over a range from zero to the critical Euler load, shown as Eq. (65).

$$P_{cr} = \pi^2 \frac{EI}{L^2} \qquad (65)$$

The structural mass fraction is varied over a range from 0.01 to 0.5. Structural mass fraction is defined as the ratio of the boom (column) mass to the total mass that includes mass of both the boom and the cable. Changes to the mass fraction in the model were accomplished by changing the cable mass density while holding the beam mass constant.

The cable tension is controlled in the structural model using a temperature gradient applied as an initial condition. In the first analysis step, the cable tensile strain directly transfers into the beam column as a compressive load through a rigid tie constraint. The geometric non-linear solver is used in the first step in order to ensure the cable tension and beam compression loads are carried over into the second step as pre-conditions, a linear perturbation dynamic analysis.

The system fundamental frequency output is recorded as the first non-zero eigenvalue frequency regardless of whether the motion is dominated by the beam or by the cable. Figure 35 shows a plot of all results normalized in the ordinate against Equation 1, and normalized in the abscissa against Equation 3. Table 11 documents the results of all analysis cases and the frequency of fundamental structural vibration for each case.

Table 12 shows the mode shape of vibration for the two extreme mass ratio cases, $\beta = 0.5$ and $\beta = 0.01$. The images show the un-deformed and deformed shape of the coupled beam-cable; the beam is distinguishable from the cable by the larger cross-section diameter. Notice by comparing the two rows in Table 12 that the mass ratio has no distinguishable effect on the mode shapes. The load ratio, on the other hand has a sizable effect. When the beam compressive load and cable tension load is small, the

cable deforms past the beam in a sinusoidal shape that is largely independent of the beam. However, when the axial loads approach Euler buckling, the tightened cable has almost no motion independent of the beam. The straight cable closely follows the motion of the beam.
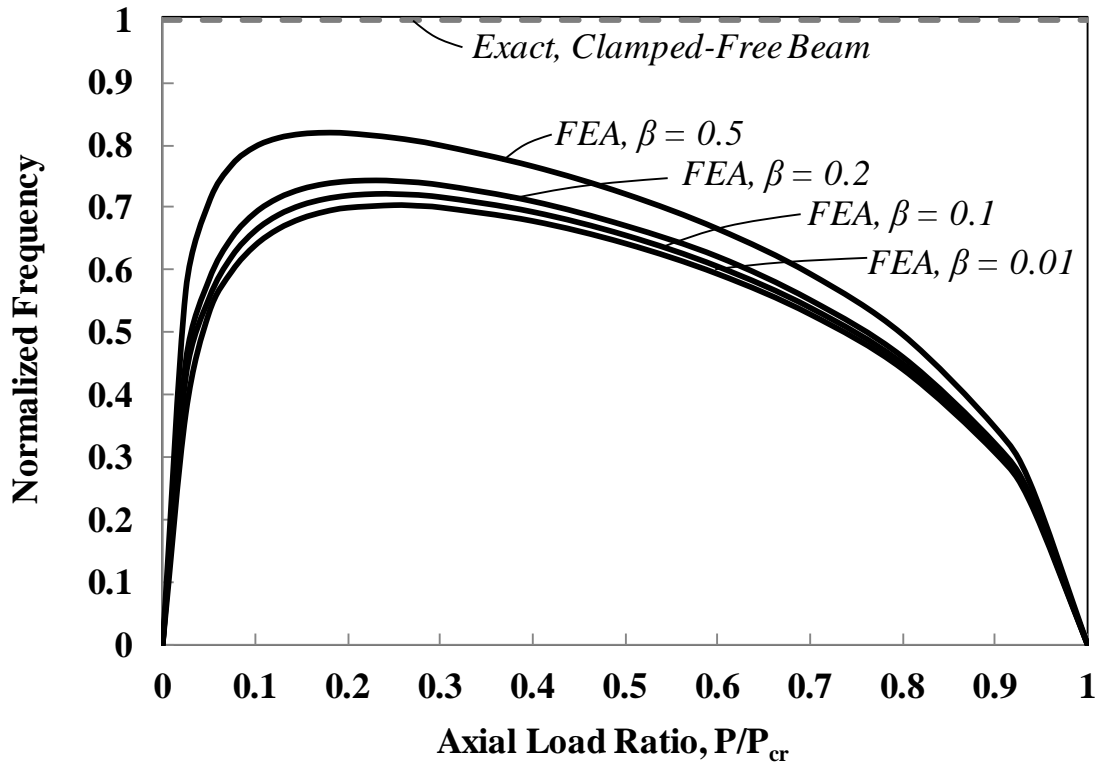
Figure 35. Beam-cable FEA results shown normalized against exact frequency and buckling solutions.

Table 11. FEA analysis cases and frequency results.

Mass Ratio	Load Ratio	Fundamental Frequency		Normalized frequency
$m_{beam}/(m_{beam} + m_{cable})$	P/P_{cr}	FEA, Hz	Beam-Only Exact, Hz	f_{FEA}/f_{Exact}
0.5	0	0.000000	0.395697	0.00000
0.5	0.025	0.224310	0.395697	0.56688
0.5	0.05	0.280170	0.395697	0.70805
0.5	0.075	0.304140	0.395697	0.76863
0.5	0.1	0.315460	0.395697	0.79724
0.5	0.125	0.321020	0.395697	0.81129
0.5	0.15	0.323560	0.395697	0.81771
0.5	0.175	0.324340	0.395697	0.81968
0.5	0.2	0.323980	0.395697	0.81877
0.5	0.25	0.321100	0.395697	0.81149
0.5	0.3	0.316340	0.395697	0.79946
0.5	0.4	0.303060	0.395697	0.76590
0.5	0.5	0.285570	0.395697	0.72170
0.5	0.6	0.263420	0.395697	0.66572
0.5	0.7	0.234970	0.395697	0.59382
0.5	0.8	0.196520	0.395697	0.49665
0.5	0.9	0.137640	0.395697	0.34785
0.5	0.9375	0.102870	0.395697	0.25998
0.5	1	0.000000	0.395697	0.00000
0.2	0	0.000000	0.250261	0.00000
0.2	0.025	0.113570	0.250261	0.45381
0.2	0.05	0.146080	0.250261	0.58371
0.2	0.075	0.163200	0.250261	0.65212
0.2	0.1	0.173050	0.250261	0.69148
0.2	0.125	0.178960	0.250261	0.71510
0.2	0.15	0.182530	0.250261	0.72936
0.2	0.175	0.184600	0.250261	0.73763
0.2	0.2	0.185660	0.250261	0.74187
0.2	0.25	0.185790	0.250261	0.74239
0.2	0.3	0.184180	0.250261	0.73595
0.2	0.4	0.177680	0.250261	0.70998
0.2	0.5	0.167920	0.250261	0.67098
0.2	0.6	0.155500	0.250261	0.62135
0.2	0.7	0.138150	0.250261	0.55203
0.2	0.8	0.115300	0.250261	0.46072
0.2	0.9	0.080502	0.250261	0.32167
0.2	0.9375	0.060074	0.250261	0.24005
0.2	1	0.000000	0.250261	0.00000

Table 11. (continued)

$m_{beam}/(m_{beam} + m_{cable})$	P/P_{cr}	FEA, Hz	Beam-Only Exact, Hz	f_{FEA}/f_{Exact}
0.1	0	0.000000	0.176961	0.00000
0.1	0.025	0.075868	0.176961	0.42873
0.1	0.05	0.098048	0.176961	0.55407
0.1	0.075	0.110110	0.176961	0.62223
0.1	0.1	0.117280	0.176961	0.66275
0.1	0.125	0.121740	0.176961	0.68795
0.1	0.15	0.124540	0.176961	0.70377
0.1	0.175	0.126250	0.176961	0.71344
0.1	0.2	0.127220	0.176961	0.71892
0.1	0.25	0.127670	0.176961	0.72146
0.1	0.3	0.126810	0.176961	0.71660
0.1	0.4	0.122620	0.176961	0.69292
0.1	0.5	0.116020	0.176961	0.65563
0.1	0.6	0.107150	0.176961	0.60550
0.1	0.7	0.095498	0.176961	0.53966
0.1	0.8	0.079674	0.176961	0.45023
0.1	0.9	0.055589	0.176961	0.31413
0.1	0.9375	0.041469	0.176961	0.23434
0.1	1	0.000000	0.176961	0.00000
0.05	0	0.000000	0.125130	0.00000
0.05	0.025	0.052260	0.125130	0.41764
0.05	0.05	0.067668	0.125130	0.54078
0.05	0.075	0.076152	0.125130	0.60859
0.05	0.1	0.081274	0.125130	0.64951
0.05	0.125	0.084498	0.125130	0.67528
0.05	0.15	0.086554	0.125130	0.69171
0.05	0.175	0.087841	0.125130	0.70200
0.05	0.2	0.088594	0.125130	0.70801
0.05	0.25	0.089026	0.125130	0.71147
0.05	0.3	0.088507	0.125130	0.70732
0.05	0.4	0.085681	0.125130	0.68473
0.05	0.5	0.081115	0.125130	0.64824
0.05	0.6	0.074931	0.125130	0.59882
0.05	0.7	0.066786	0.125130	0.53373
0.05	0.8	0.055711	0.125130	0.44523
0.05	0.9	0.038859	0.125130	0.31055
0.05	0.9375	0.028984	0.125130	0.23163
0.05	1	0.000000	0.125130	0.00000

Table 11. (continued)

$m_{beam}/(m_{beam} + m_{cable})$	P/P_{cr}	FEA, Hz	Beam-Only Exact, Hz	f_{FEA}/f_{Exact}
0.02	0.025	0.032557	0.079139	0.41139
0.02	0.05	0.042200	0.079139	0.53324
0.02	0.075	0.047547	0.079139	0.60081
0.02	0.1	0.050798	0.079139	0.64189
0.02	0.125	0.052861	0.079139	0.66796
0.02	0.15	0.054188	0.079139	0.68472
0.02	0.175	0.055027	0.079139	0.69533
0.02	0.2	0.055527	0.079139	0.70164
0.02	0.25	0.055840	0.079139	0.70561
0.02	0.3	0.055545	0.079139	0.70188
0.02	0.4	0.053808	0.079139	0.67992
0.02	0.5	0.050958	0.079139	0.64391
0.02	0.6	0.047081	0.079139	0.59492
0.02	0.7	0.041964	0.079139	0.53026
0.02	0.8	0.035003	0.079139	0.44230
0.02	0.9	0.024411	0.079139	0.30846
0.02	0.9375	0.018206	0.079139	0.23005
0.02	1	0.000000	0.079139	0.00000
0.01	0	0.000000	0.055960	0.00000
0.01	0.025	0.020717	0.055960	0.37022
0.01	0.05	0.029703	0.055960	0.53079
0.01	0.075	0.033479	0.055960	0.59827
0.01	0.1	0.035780	0.055960	0.63940
0.01	0.125	0.037244	0.055960	0.66556
0.01	0.15	0.038188	0.055960	0.68243
0.01	0.175	0.038787	0.055960	0.69314
0.01	0.2	0.039146	0.055960	0.69954
0.01	0.25	0.039377	0.055960	0.70367
0.01	0.3	0.039176	0.055960	0.70008
0.01	0.4	0.037959	0.055960	0.67833
0.01	0.5	0.035953	0.055960	0.64248
0.01	0.6	0.033219	0.055960	0.59362
0.01	0.7	0.029609	0.055960	0.52912
0.01	0.8	0.024697	0.055960	0.44133
0.01	0.9	0.017222	0.055960	0.30777
0.01	0.9375	0.012845	0.055960	0.22954
0.01	1	0.000000	0.055960	0.00000

Table 12. Sample mode shapes of fundamental structural vibration.
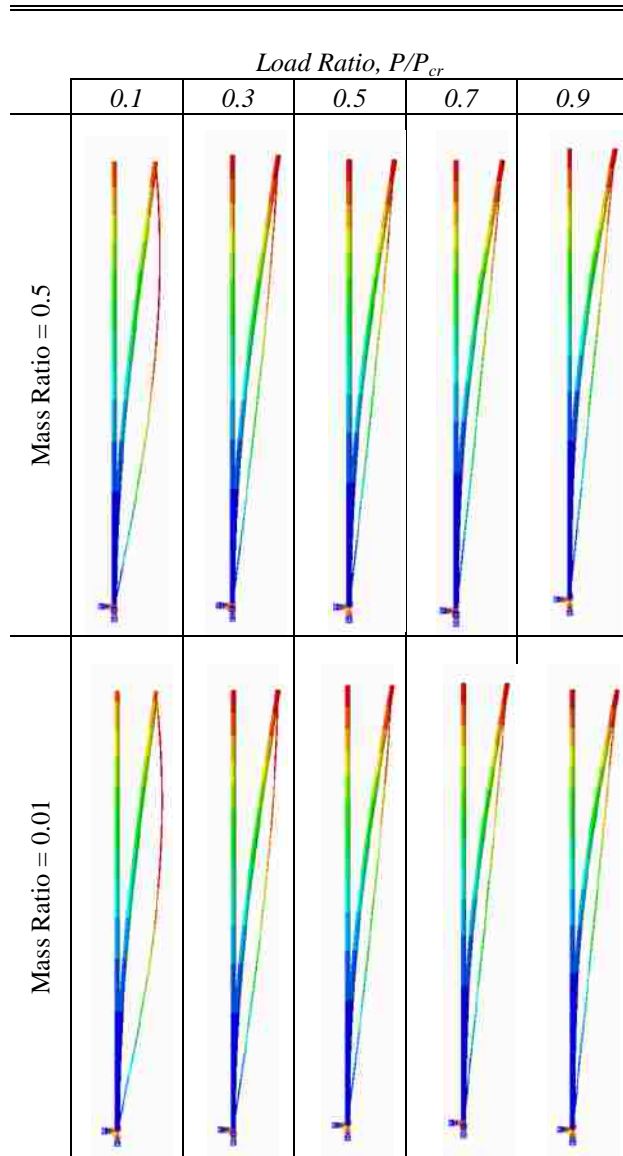
APPENDIX B. NUMERICAL MODEL MATHEMATICA© CODE

Flexible Blanket Solar Array Mass Solution

`Mathematica version 8.0`
Created by Jeremy A. Banik
24 January 2014

`m = Total mass of solar array, kg`

`A = Total power collecting area of solar arary, `m^2

`Lpb = Length of primary boom (s) supporting an`
`   array winglet cantilevered from spacecraft bus or from a`
`   rigid backbone boom in the case of multiple winglets, m`

`Lsb = Length of the rigid spreader bar, m`

`npb = Quantity of primary booms arranged in parallel`

`wpb = Primary boom mass per unit length, kg / m`

`wsb = Spreader bar mass per unit length, kg / m`

γ`b = Photovoltaic blanket areal mass density, `kg / m^2

`M = Primary boom failure moment, Nm`

`EI = Primary boom bending stiffness, `Nm^2

μ`pb = Primary boom beam index, `$N^{3/5}\, m^{9/5} / kg$

`f = Solar array fundamental frequency, Hz`

`a = Applied acceleration as a fraction of Earth's grav constant; a * 9.81 m / `s^2

Constraint Requirements Equations

Total array area :
`     A = Lsb Lpb;`

Primary boom mass per unit length is generically related to the critical
**   moment and bending stiffness through a beam structural efficiency rating :**

$$\mu\text{pb} \geq \mu\text{pb req} = \frac{\left(M^2\, EI\right)^{1/5}}{\text{wpb}} \; -->\; \text{wpb} = \frac{\left(M^2\, EI\right)^{1/5}}{\mu\text{pb}} \;;$$

Primary boom moment load requirement
**   due to lateral inertial loads from a bus translation acceleration :**

$$M \geq \text{Mreq} = \left(\text{npb wpb} + \gamma\text{b A / Lpb} + \frac{\text{wsb A / Lpb}}{\text{Lpb}}\right) \frac{a\, g\, \text{Lpb}^2}{2}$$

$$\text{npb} = \frac{1}{\text{wpb}}\left(\frac{2\,M}{a\,g\,\text{Lpb}^2} - \frac{\gamma\text{b A}}{\text{Lpb}} + \frac{\text{wsb A}}{\text{Lpb}^2}\right);$$

Primary boom bending stiffness requirement due to minimum
**   fundamental frequency of a series of clamped – free beams in parallel :**
**   No tip mass effects –– Energy Methods Approx. for clamped – free, multi – beam**

$$\text{EI} \geq \text{EIreq} = \left(f\,\frac{2\,\pi}{3.5355\,\eta}\right)^2 \frac{\text{Lpb}^4}{\text{npb}} \left(\text{npb wpb} + \gamma\text{b A / Lpb} + \frac{\text{wsb A / Lpb}}{\text{Lpb}}\right);$$

$$\text{wpb} = \frac{1}{\text{npb}}\left(\left(\frac{\eta\,3.5355}{f\,2\,\pi}\right)^2 \frac{\text{npb EI}}{\text{Lpb}^4} - \frac{\gamma\text{b A}}{\text{Lpb}} - \frac{\text{wsb A}}{\text{Lpb}^2}\right);$$

Weight Equation Solution;

(∗ Objective Function, Array Weight Equation; ∗)
γt[γb_, npb_, wpb_, Lpb_, A_, wsb_] := γb + npb wpb Lpb / A + wsb / Lpb;

(∗ Constraint Equations based on acceleration,frequency and beam efficiency ∗)
g = 9.81;
η = 0.76;
(∗ Array (system) Frequency ∗)
EI[npb_, f_, Lpb_, γb_, A_, wsb_, wpb_] :=

$$\left(f\,\frac{2\,\pi}{3.5355\,\eta}\right)^2\frac{Lpb^4}{npb}\left(npb\,wpb + \gamma b\,A\,/\,Lpb + \frac{wsb\,A\,/\,Lpb}{Lpb}\right);$$

(∗ Array (system) Acceleration Load ∗)
M[wpb_, npb_, a_, Lpb_, γb_, A_, wsb_] :=

$$\left(\frac{1}{npb}\right)\left(npb\,wpb + \gamma b\,A\,/\,Lpb + \frac{wsb\,A\,/\,Lpb}{Lpb}\right)\frac{a\,g\,Lpb^2}{2}$$

(∗ Beam (component) Efficiency ∗)

$$wpb[M\_,\ EI\_,\ \mu pb\_] := \frac{\left(M^2\,EI\right)^{1/5}}{\mu pb};$$

NOTE : Form transcendental equation for wpb by substituting frequency and
    strength equations into beam efficiency equation and solve symbolically
    using numerical methods to isolate wpb since wpb appears on both sides ∗)
(∗ First check the transcendental equation for wpb ∗)
Print["Transcendental Equation for wpb = ", FullSimplify[
    wpb[M[wpb, npb, a, Lpb, γb, A, wsb], EI[npb, f, Lpb, γb, A, wsb, wpb], μpb]]];
(∗ Solve the wpb transendental equation ∗)
wpbsol[npb_, f_, μpb_, a_, Lpb_, γb_, A_, wsb_] :=
 Solve[wpb[M[wpb, npb, a, Lpb, γb, A, wsb],
        EI[npb, f, Lpb, γb, A, wsb, wpb], μpb] == wpb, {wpb}]$_{[\![1]\!]}$ // FullSimplify
Print["First Root, Numerical Solution, of wpb Transcendental Equation = ",
  wpbsol[npb, f, μpb, a, Lpb, γb, A, wsb]];
(∗ Substitute wpb solution into weight equation and solve for γt ∗)
Print["Polynomial Equation for γt = ",
  FullSimplify[
    γt[γb, npb, wpbsol[npb, f, μpb, a, Lpb, γb, A, wsb], Lpb, A, wsb]]];
γtsol[npb_, f_, μpb_, a_, Lpb_, γb_, A_, wsb_] := FullSimplify[
    γt[γb, npb, wpbsol[npb, f, μpb, a, Lpb, γb, A, wsb]$_{[\![1,-1]\!]}$, Lpb, A, wsb]];
(∗ [[1,-1]] refers to the first part, 1, of the last part, -1,
in the list, thus the numerical value for wpb in the numerical
 solution for wpb once all variables have been defined numerically ∗)

Transcendental Equation for wpb = $\dfrac{404.201\left((1.33333 + 2\,\text{wpb})^3\right)^{1/5}}{\mu\text{pb}}$

First Root, Numerical Solution, of wpb Transcendental Equation =

$\Big\{\text{wpb} \rightarrow \text{Root}\Big[-\dfrac{2.4415117612351574948801638846377 \times 10^{47}}{\mu\text{pb}^5} -$

$\dfrac{1.0986802925558208726960737480870 \times 10^{48}\,\#1}{\mu\text{pb}^5} -$

$\dfrac{1.6480204388337313090441106221304 \times 10^{48}\,\#1^2}{\mu\text{pb}^5} -$

$\dfrac{8.2401021941686565452205531106 52 \times 10^{47}\,\#1^3}{\mu\text{pb}^5} +$

$9.5467086254273317028871430191 45 \times 10^{33}\,\#1^5\ \&,\ 1\Big]\Big\}$

Polynomial Equation for γt =

$\Big\{0.666667 + \Big(\text{wpb} \rightarrow \text{Root}\Big[-\dfrac{2.4415117612351574948801638846377 \times 10^{47}}{\mu\text{pb}^5} -$

$\dfrac{1.0986802925558208726960737480870 \times 10^{48}\,\#1}{\mu\text{pb}^5} -$

$\dfrac{1.6480204388337313090441106221304 \times 10^{48}\,\#1^2}{\mu\text{pb}^5} -$

$\dfrac{8.2401021941686565452205531106 52 \times 10^{47}\,\#1^3}{\mu\text{pb}^5} +$

$9.5467086254273317028871430191 45 \times 10^{33}\,\#1^5\ \&,\ 1\Big]\Big)\Big\}$

Minimum Optimum μpb Solution;

Baseline Definitions of Variables

```
f = 1;
γb = 1;
wsb = 3;
npb = 2;
μpb =.; μpbmin = 0; μpbmax = 5000;
Lpb = 30;
a = 1;
A = 60;
(**)
```

(∗ Solve for the minimum optimum μpb and the corresponding γt for one case∗)

```
γtsolp[npb_, f_, μpb_, a_, Lpb_, γb_, A_, wsb_] := D[FullSimplify[γt[γb, npb,
    wpbsol[npb, f, μpb, a, Lpb, γb, A, wsb]⟦1,-1⟧, Lpb, A, wsb]], {μpb, 1}];
(* Minimum optimum μpb occurs when the slope of d(γt)/d(μpb) = -10/5000 *)
μpbtemp = NSolve[{γtsolp[npb, 1, μpb, a, Lpb, γb, A, wsb]} == -1 / 500, μpb]⟦1,1,-1⟧;
```

```
γtsoltemp = γtsol[npb, 1, μpbtemp, a, Lpb, γb, A, wsb];
Print["Minimum Optimum μpb = ", μpbtemp, "; where γt = ", γtsoltemp];
Print["      npb = ", npb, "; af = ", af, "; μpb = ", μpb,
  "; Lpb = ", Lpb, "; γb = ", γb, "; A = ", A, "; wsb = ", wsb]
```

(∗ **Solve for minimum optimum μpb and γt for 2430 discrete cases:**
   1. Define INPUT as discrete value ranges (162 cases):
     γb=[0.5,1,2]; , wsb=[1,3,5], npb=[1,2,10], Lpb=5,10,15,20,25,30]
    2. Solve [dγt / dμpb = −1/500, for μpb]
    print the 168 μpb numerical solutions. This
    derivative locates the "knee in the curve" for the plot of
    γt versus μpb over the range of interest: γt=[0:10], μpb=[0:5000].
    3. Print the corresponding
    γt values for the minimum optimum μpb from step 2
   4. Copy the two lists, γt and μpb, to Excel
   5. Repeat steps 2−4 for the 15 unique requirements cases:
     A=[10, 60,200,600,2000], af=[0.00001,0.01,1]
    6. Curve fit the unique cases
     in Excel to find common relationships: ∗)

```
Table[
 Print[NSolve[{γtsolp[npb, 1, μpb, a, Lpb, γb, A, wsb]} == -1 / 500, μpb]⟦1,1,-1⟧],
 {γb, {0.5, 1, 2}}, {wsb, {1, 3, 5}},
 {npb, {1, 2, 10}}, {Lpb, {5, 10, 15, 20, 25, 30}}]
```
(∗ γt ∗)
```
Table[Print[γtsol[npb, 1,
    NSolve[{γtsolp[npb, 1, μpb, a, Lpb, γb, A, wsb]} == -1 / 500, μpb]⟦1,1,-1⟧,
    a, Lpb, γb, A, wsb]], {γb, {0.5, 1, 2}}, {wsb, {1, 3, 5}},
 {npb, {1, 2, 10}}, {Lpb, {5, 10, 15, 20, 25, 30}}] ∗)
```
(∗ **Plot γt vs μpb** ∗)
```
Print["Black=γt, Blue=γb, Red=γsb, Brown=γpb"]
Plot[{γtsol[npb, 1, μpb, a, Lpb, γb, A, wsb], γb},
 {μpb, μpbmin, μpbmax}, PlotRange → {{0, 5000}, {0, 10}}, Frame → True,
 Axes → False, FrameLabel -> {"μ, N^{3/5}m^{9/5}/ kg", "γ, kg/m^2"},
 ImageSize → 260, PlotStyle → {{Black, Thick}, {Dashed, Black, Thick}},
 BaseStyle → {FontSize → 10, FontWeight → Bold}]
```
```
(∗ Plot[{γtsol[npb,1,μpb,a,Lpb,γb,A,wsb],γb,wsb/Lpb,
  npb Lpb/A wpbsol[npb,1,μpb,a,Lpb,γb,A,wsb]⟦1,-1⟧},
 {μpb,μpbmin,μpbmax},PlotRange→{{0,5000},{0,10}},Frame→True,
 Axes→False,FrameLabel->{"μpb","γt, kg/m^2"},ImageSize→500,
 PlotStyle→{{Black,Thick},{Blue,Thick},{Red,Thick},{Brown,Thick}},
 BaseStyle→{FontSize→12,FontWeight→Bold}] ∗)
```
(∗ **Plot γt' vs μpb** ∗)
```
γtsolp[npb_, f_, μpb_, a_, Lpb_, γb_, A_, wsb_] = D[FullSimplify[γt[γb, npb,
     wpbsol[npb, f, μpb, a, Lpb, γb, A, wsb]⟦1,-1⟧, Lpb, A, wsb]], {μpb, 1}];
Plot[{γtsolp[npb, 1, μpb, a, Lpb, γb, A, wsb]} * 500, {μpb, μpbmin, μpbmax},
```

```
PlotRange → {{0, 5000}, {-1.00001, -0.99999}}, Frame → True,
Axes → False, FrameLabel -> {"μpb", "γt'"}, ImageSize → 500,
PlotStyle → {Black, Thick}, BaseStyle → {FontSize → 10, FontWeight → Bold}]
```

Minimum Optimum μpb = 852.91292925130628243361486550480; where γt = 2.27681

npb = 2; af = 1; μpb = μpb; Lpb = 30; γb = 1; A = 60; wsb = 3

Black=γt, Blue=γb, Red=γsb, Brown=γpb
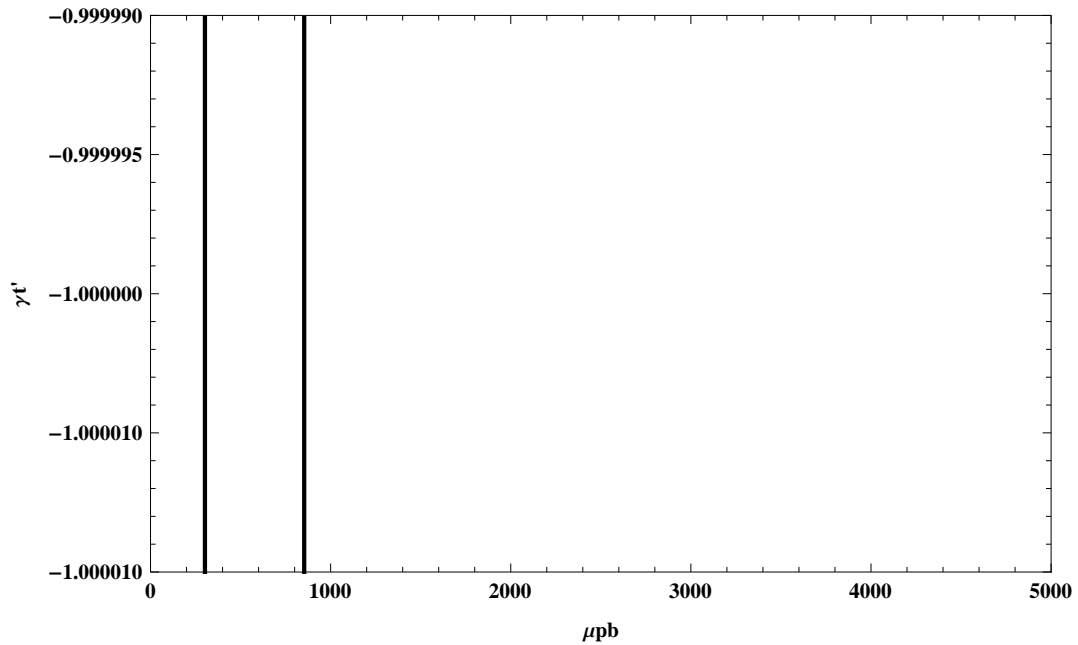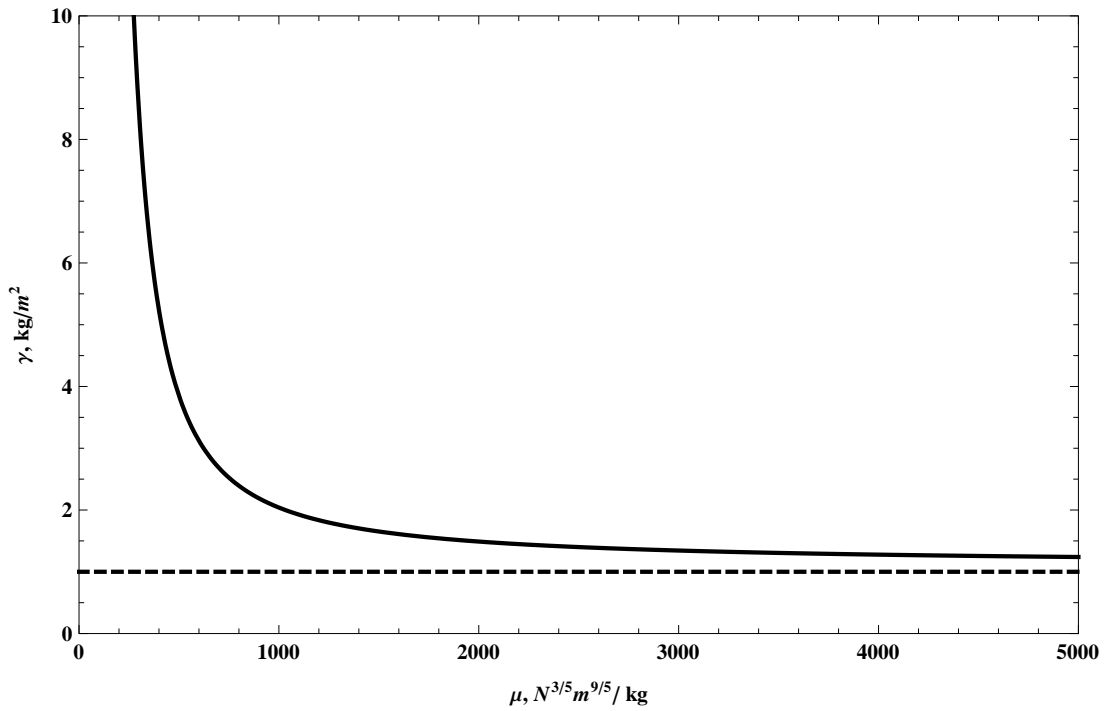
(∗ Solve γt using Minimum Optimum μpb Approximation∗)

(∗ **Variable Definitions** ∗)

```
f = 1; (* Hz, f = 1 always *)
μpb =.; (* N^(3/5)m^(9/5)/kg *)
(* μpb=6.911/A^0.255 Lpb (a f)^0.22 (2.085 npb+2.386 γb+6.03); *)
γb = 0.5; (* kg/m^2 *) γbmin = 0.5; γbmax = 2;
wsb = 5; (* kg/m *) wsbmin = 1; wsbmax = 5;
npb = 10; npbmin = 1; npbmax = 10;
Lpb =.; (* m *) Lpbmin = 5; Lpbmax = 30;
(* if Lpb<5 then γpb→f(wsb) else γpb≠f(wsb)*)
a = 1; (* m/s^2 *) amin = 0.00001; amax = 1;
A = 10; (* m^2 *) Amin = 10; Amax = 2000;
```

(∗ **Define minimum optimum μpb approximation**∗)

```
μpbOpt[npb_, f_, a_, Lpb_, γb_, A_] :=
   6.911 / A^0.255 Lpb (a f)^0.22 (2.085 npb + 2.386 γb + 6.03);
```

(∗ **Plot the γt results with μpb minimum optimum approximation** ∗)

```
Print["Black=γt, Gray=γt(γb=wsb=0), Blue=γb, Red=γsb, Brown=γpb"]
Print["     npb = ", npb, "; af = ", a f, "; μpb = ", μpb,
 "; Lpb = ", Lpb, "; γb = ", γb, "; A = ", A, "; wsb = ", wsb]
Plot[{γtsol[npb, f, μpbOpt[npb, f, a, Lpb, γb, A], a, Lpb, γb, A, wsb],
  γtsol[npb, f, μpbOpt, a, Lpb, 0, A, 0], γb, wsb / Lpb,
  npb Lpb / A wpbsol[npb, f, μpbOpt, a, Lpb, γb, A, wsb][[1,-1]]},
 {Lpb, Lpbmin, Lpbmax}, PlotRange → {{5, 30}, {0, 10}}, Frame → True,
 Axes → False, FrameLabel -> {"Lpb", "γt, kg/m^2"}, ImageSize → 500,
 PlotStyle → {{Black, Thick}, {Gray, Thick, Dashed}, {Blue, Thick}, {Red, Thick},
   {Brown, Thick}}, BaseStyle → {FontSize → 12, FontWeight → Bold}]
```

```
Black=γt, Gray=γt(γb=wsb=0), Blue=γb, Red=γsb, Brown=γpb

    npb = 10; af = 1; μpb = μpb; Lpb = Lpb; γb = 0.5; A = 10; wsb = 5
```
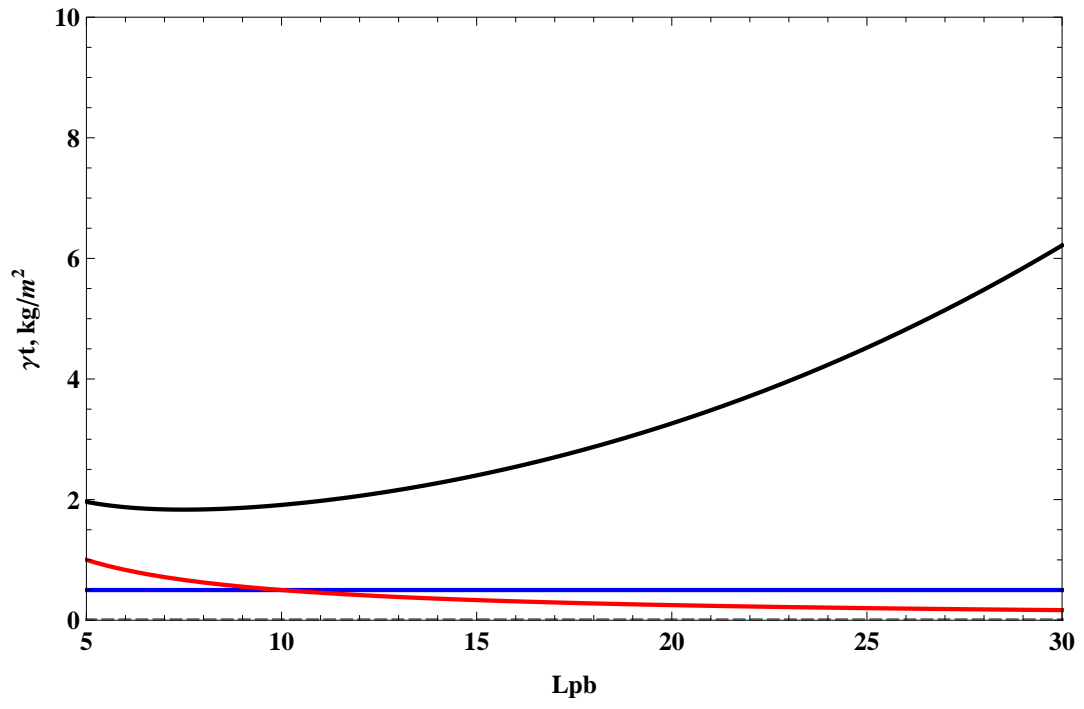
APPENDIX C. REGRESSION TECHNIQUES FOR METRIC

DEVELOPMENT

Regression is an error minimization technique that is used here to develop an approximation model from the more complex numerical model of solar array mass. The approximation model is necessary because out of this model, simplified metrics are developed that represent solar array structural scaling effects in a form that is easy to understand and implement for structural architecture comparisons. The approximation model is not as accurate as the numerical model but is well within an acceptable error for the purposes of architecture comparison.

Before detailing the approximation model, a brief review of the numerical model is provided. It is developed using the constraint analysis process that minimizes solar array mass based on mechanics principles for fundamental frequency and beam strength. A single transcendental equation for array mass is developed that is solved using numerical methods.

It is necessary to discretize the structural design variables in order to form structural design cases. These discretized parameters are listed in Table 13. Unique combinations of this set total 2,430 unique solar array structural architecture cases.

The array mass is predicted for a range of array design cases in order to understand the conditions by which mass is minimized. It was discovered that minimizing array mass simultaneously maximizes the beam efficiency index; therefore no local minima or maxima exists for array mass. To avoid the trivial solution of zero mass and infinite beam efficiency, the "knee in the curve" between array mass and beam

efficiency is calculated for each design case, effectively minimizing both terms

simultaneously. For each unique design case, a pair of array mass and beam efficiency

values exist. Table 13 lists the six design parameters that are discretized to form a total of

2,430 design cases.

Table 13. Discretized range of design parameters used to define 2,430 unique structural architectures

		[Discrete] Range	Units
Objective Constraint			
Areal Mass Density	γ	0 - 10	kg/m^2
Array Design Requirements			
Loading Term	af	[0.00001, 0.01, 1]	Hz 9.71 m/s^2
Area	A	[10, 60, 200, 600, 2000]	m^2
Primary Boom Properties			
Beam Efficiency Index	μ	1 - 5000	$N^{3/5}m^{9/5}/kg$
Length	L_{pb}	[5, 10, 15, 20, 25, 30]	m
Quantity	n	[1, 2, 10]	--
Blanket Properties			
Areal Mass Density	γ_b	[0.5, 1, 2]	kg/m^2
Spreader Bar Properties			
Linear Mass Density	w_{sb}	[1, 3, 5]	kg/m

The first step in developing the approximation model is to evaluate the

sensitivities of each design parameter to the array mass and beam efficiency terms.

Strictly speaking the array mass is a function of beam, blanket, and spreader bar mass.

However, all but the beam mass have only a linear additive effect on array mass. This

reality coupled with the minimized solution for array mass and beam efficiency allows

the approximation modeling to be focused on the six design parameters from Table 13

and the effect on beam efficiency.

The relative sensitivity of these seven variables is accomplished through an informal design of experiments process culminating in regression analysis. Each step in this regression analysis process is shown in Figure 36. Each combination of variables is explored and the sensitivity of interactions is observed and recorded. Based on these observations, the parameters are ranked according to relative influence on beam efficiency. Reduced sets of the most sensitive variable combinations were compared and approximately quantified through regression techniques in the order of relative sensitivity. These relations were then reassembled into an approximation model of the array architecture. Observations and conclusions from each of these steps are provided in the following.

Simultaneously minimize array mass and beam efficiency, γ and μ, producing 2,430 design cases, each related to a unique numerical value pair, μ and γ.

$\gamma = \gamma_{pb} + \gamma_b + \gamma_{sb}$

$\gamma_{pb} = \mu(af, L, A, n, \gamma_b, w_{sb})$

Rank the design parameters according to relative sensitivity to changes in μ.

1) A
2) L
3) af
4) n
5) γ_b
6) w_{sb}

Approximate the functional relationship between each parameter and the beam efficiency index, μ, in rank order. $\mu(A, L_{pb}, af, n, \gamma_b, w_{sb})$

~~w_{sb} [1:5] kg/m²~~   (eliminated due to trivial effect on μ)

$A = [10:2000]$ m²

| $A = 2000$m² | $A = 600$m² | $A = 200$m² | $A = 60$m² | $A = 10$m² |

$\mu [f(A, L_{pb}, af, n, \gamma_b)]$ L_{pb} [5, 10, 15, 20, 25, 30] m

$$\frac{\mu}{L_{pb}} \approx c1[f(A, af, n, \gamma_b)]$$ af [0.00001, 0.01, 1] Hz 9.71 m/s²

$$\frac{\mu}{L_{pb}} \approx c2\left[f(A, n, \gamma_b)\right](af)^{0.216}$$ n [1, 2, 10]

$$\frac{\mu}{L_{pb}} \approx c4\left[f(A, \gamma_b)\right] n^{0.231} (af)^{0.216}$$ γ_b [0.5, 1, 2] kg/m²

$$\frac{\mu}{L_{pb}} \approx c6\left[f(A)\right] 9.823\, \gamma_b^{0.176}\, n^{0.231}\, (af)^{0.216}$$

$$\frac{\mu}{L_{pb}} \approx \frac{63.357}{A^{0.245}}\, \gamma_b^{0.176}\, n^{0.231}\, (af)^{0.216}$$

Figure 36.   Regression analysis process flow.

C.1   Parameter Sensitivities

The first data set to be examined was that of the largest area, $A = 2000\ m^2$. Focusing on a single area data set to begin helps to make the analysis more manageable since the number of unique design cases is reduced from 2,430 to 486. The first observation from this set was that the beam efficiency index, μ, and the primary boom length, L_{pb}, are linearly related, and the slope of this relationship is affected by all remaining terms. The slope is highly sensitive to changes in the loading term, af. It is mildly sensitive to changes blanket areal mass density, γ_b, and boom quantity, n. And the slope is mostly insensitive to changes in the spreader bar linear mass density, w_{sb}. Conveniently, the remaining four area cases proved to respond similarly in trend to this large area case so it is investigated further as a representative set.

Changing the spreader bar mass density proved inconsequential to all the parametric cases except for those of the most extreme aspect ratio. For example, large area arrays that are very short tend to be measurably affected by spreader bar density. These cases include those with a length of no more than 5 meters and an area of 200 m^2 or greater and a spreader bar density of 3 kg/m or greater. The practical challenges of building a 5 meter long by 60 meter wide (or wider) array are likely to prevent such a structure from every being seriously considered. Therefore since the mass of the spreader bar has a small effect on practical array sizes, this term is neglected in the approximation model. This reduces the number of design cases from 2,430 to 810.

C.2 Parameter Relations

Now that the sensitivities of the parameters have been established, relationships between parameters are quantified. The largest area cases are again investigated first, reducing the number of design cases from 810 to 162. The beam efficiency index is related to the array length term due to the previously observed approximately linear relationship. Since the slope of this relation is determined to be highly sensitive to the loading term, the results are separated into three respective data sets illustrated in Figure 37, Figure 38, and Figure 39 by *af = 0.00001 9.81-Hz-m/s², 0.01 9.81-Hz-m/s², and 1.0 9.81-Hz-m/s²*.

af = 0.00001, A = 2000
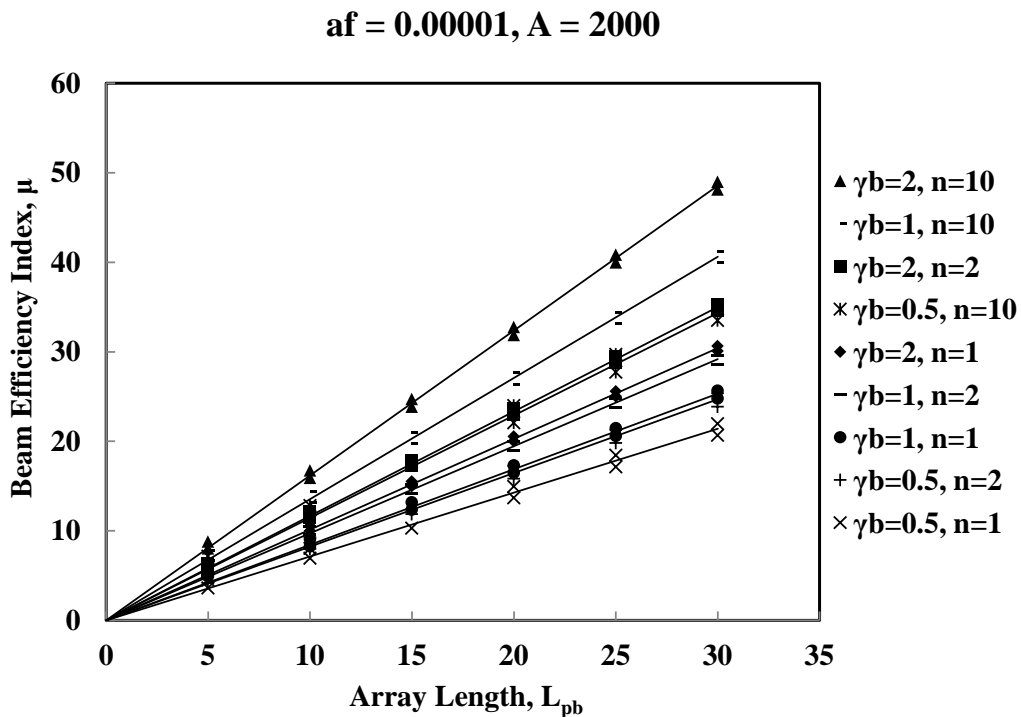
Figure 37. The smallest loading term and largest area cases.

af = 0.01, A = 2000
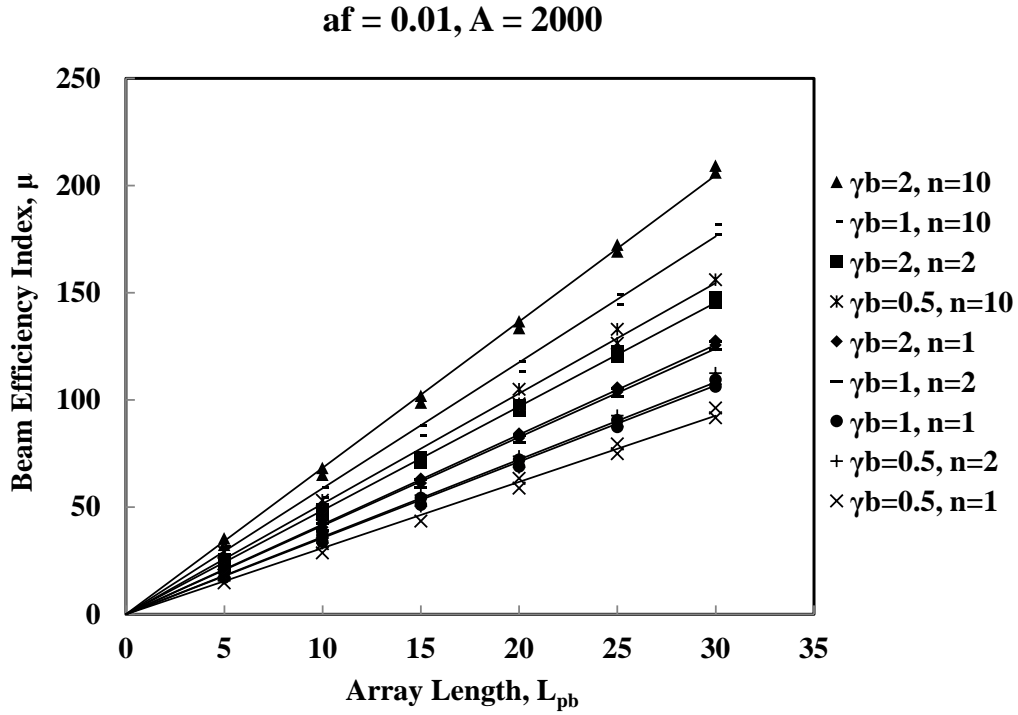
Figure 38. The mid-level loading term and largest area cases.

af = 1, A = 2000
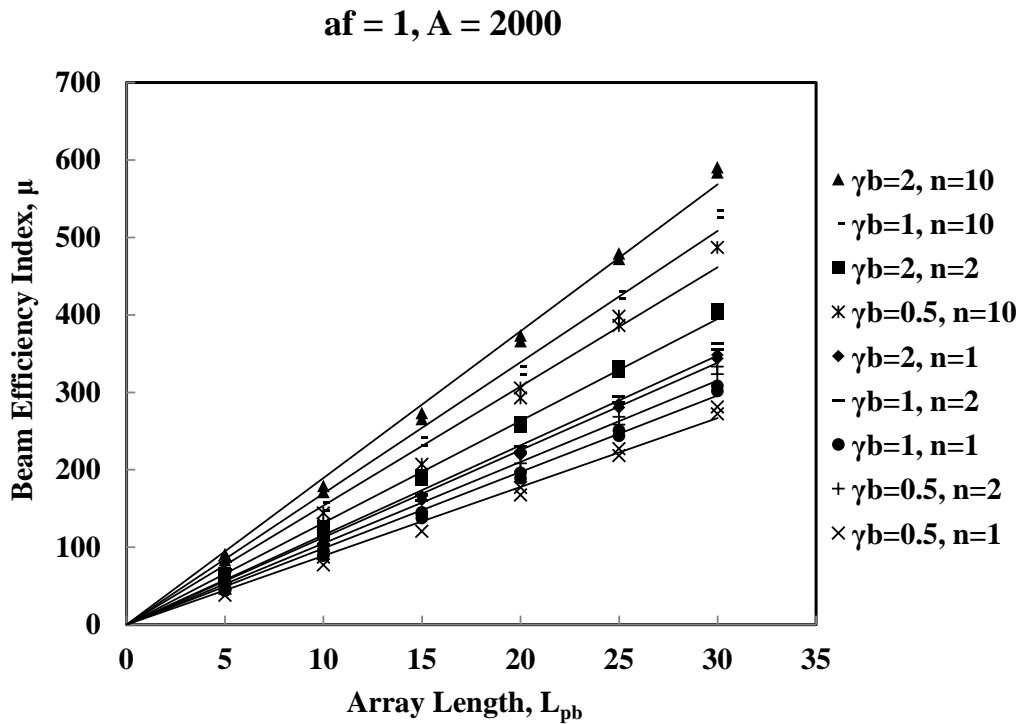
Figure 39. The largest loading term and largest area cases.

145

Each of these three plots is separated into nine data sets representing the nine unique combinations of blanket density and boom quantity. The data set labels on the plot are ordered in the same sequence as they appear. This sequence remains unchanged for all three plots, but the spread between the plots, i.e., slope, is strongly affected by the loading term of the given figure. Notice the difference in ordinate scale between the three. The cases that require the highest beam efficiency are those with the most massive blankets and the greatest number of booms used to support those blankets. Conversely as the blanket mass shrinks and the quantity of booms approaches unity, the required beam efficiency index is minimized.

A linear regression fit is applied to each of 27 data sets in these three figures. The coefficient c_1 and coefficient of determination, R^2, are recorded in Table 14. The R^2 value is the squared correlation between the numerical model data and the regression fit. It is a measure of fit goodness where a value of 1.0 indicates a perfect fit, and a value of less than one indicates a less than perfect fit.

From Figure 37, Figure 38, and Figure 39 notice the direct correlation between the beam efficiency index magnitudes and the respective loading term. Greater loading term values drive toward the need for more efficient beam columns.

In the first step, the beam efficiency term and the array length term are combined into a ratio due to the observed direct proportionality. This ratio is represented by the coefficient c_1, a value that is unique for each of the 27 cases and is listed in Table 14.

Table 14. The linear regression fit between beam efficiency index and array length for A = 2000 m².

A	γ_b	af	n	Regression: $c_1 \approx \mu / L_{pb}$	
				c_1	R^2
m²	kg/m²	9.81-Hz-m/s²	–	–	–
2000	2	0.00001	10	1.619	0.9989
2000	2	0.01	10	6.832	0.9985
2000	2	1	10	18.959	0.9943
2000	2	0.00001	2	1.167	0.9989
2000	2	0.01	2	4.851	0.9989
2000	2	1	2	13.162	0.9965
2000	2	0.00001	1	1.014	0.9988
2000	2	0.01	1	4.192	0.9989
2000	2	1	1	11.281	0.9971
2000	1	0.00001	10	1.355	0.9964
2000	1	0.01	10	5.877	0.9965
2000	1	1	10	16.945	0.9902
2000	1	0.00001	2	0.973	0.9961
2000	1	0.01	2	4.134	0.9970
2000	1	1	2	11.586	0.9934
2000	1	0.00001	1	0.845	0.9950
2000	1	0.01	1	3.561	0.9970
2000	1	1	1	9.871	0.9944
2000	0.5	0.00001	10	1.145	0.9898
2000	0.5	0.01	10	5.153	0.9950
2000	0.5	1	10	15.389	0.9869
2000	0.5	0.00001	2	0.823	0.9898
2000	0.5	0.01	2	3.610	0.9928
2000	0.5	1	2	10.516	0.9892
2000	0.5	0.00001	1	0.713	0.9894
2000	0.5	0.01	1	3.091	0.9928
2000	0.5	1	1	8.897	0.9904
				MEAN	*0.9946*
				STD DEV	*0.0036*
				MAX	*0.9989*
				MIN	*0.9869*

Next, this coefficient is related to the loading term illustrated in Figure 40. The three loading term cases are shown on the abscissa. Again the unique array blanket and boom quantity parameters are represented by nine data sets for a total of 27 set cases. The relationships between the ordinate and abscissa in this figure are related through a power regression quantified by a linear coefficient c_2 and a raised power c_3. The values for these coefficients are listed in Table 15 along with the regression equation to which they are assigned. Closer inspection of the coefficient c_3 shows a relatively constant value for all nine cases. Therefore the mean of c^3 is calculated and used as the raised power coefficient for the loading term.
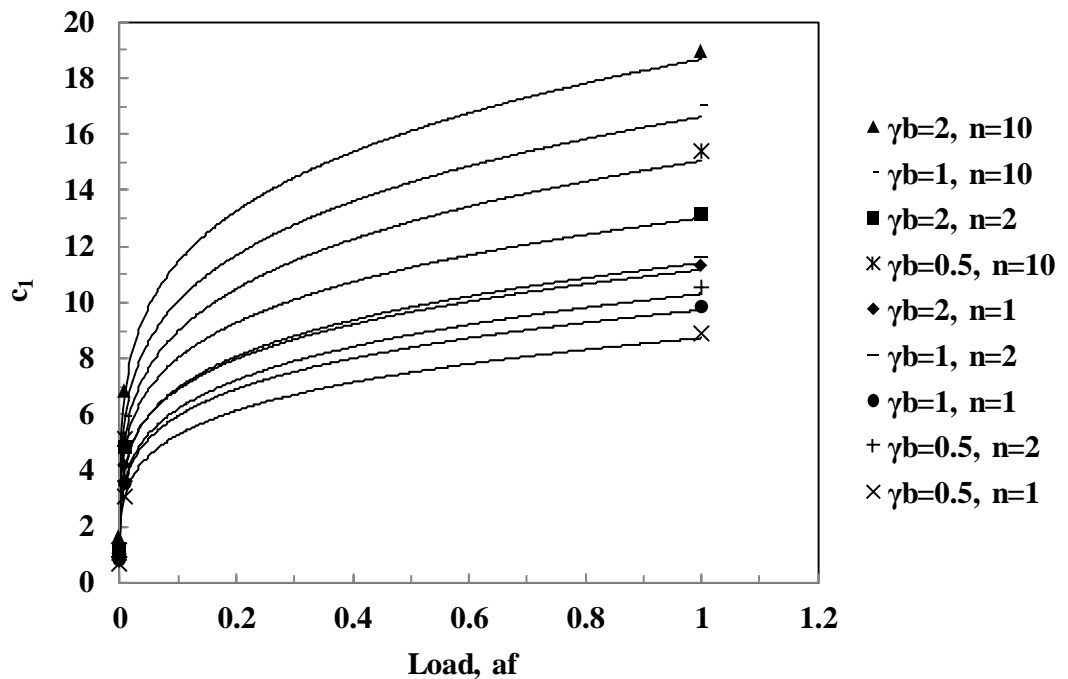
Figure 40. The coefficient c1 is related to the loading term through a power regression.

Table 15. The power regression between beam efficiency index, length, and loading term.

| A | γ_b | n | Regression: $\mu / L_{pb} \approx c_2 (af)^{c3}$ | | |
| | | | c_2 | c_3 | R^2 |
m^2	kg/m^2				
2000	2	10	18.687	0.213	0.9997
2000	2	2	13.012	0.210	0.9998
2000	2	1	11.166	0.209	0.9998
2000	1	10	16.625	0.219	0.9995
2000	1	2	11.406	0.215	0.9997
2000	1	1	9.731	0.213	0.9997
2000	0.5	10	15.059	0.225	0.9994
2000	0.5	2	10.309	0.221	0.9995
2000	0.5	1	8.731	0.219	0.9995
			MEAN	***0.216***	*0.9996*
			STD DEV	*0.005*	*0.0001*
			MAX	*0.225*	*0.9998*
			MIN	*0.209*	*0.9994*

Next, the coefficient c_2 is further examined as it relates to the remaining variables, blanket density and boom quantity. A power regression between n and c_2 is illustrated in Figure 41. This fit introduces two new coefficients c_4 and c_5 as listed in Table 16. The coefficient of determination is also listed along with the regression relation. The mean of the coefficient c_5 is used as the raised power coefficient for the boom quantity parameter.
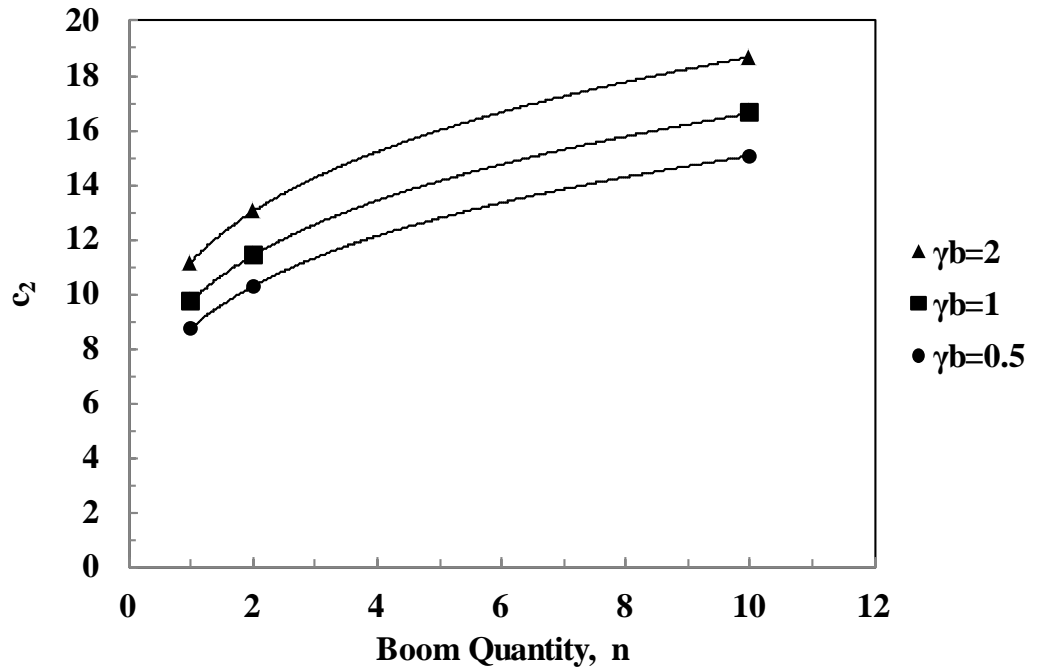
Figure 41. The coefficient c2 is related to the boom quantity parameter through a power regression.

Table 16. The power regression between the beam efficiency index, length, boom quantity, and loading term.

		Regression: $\mu / L_{pb} \approx c_4\, n^{c5}\, (af)^{0.216}$		
A	γ_b	c_4	c_5	R^2
m^2	kg/m^2			
2000	2	11.156	0.224	1.0000
2000	1	9.721	0.233	1.0000
2000	0.5	8.739	0.237	1.0000
		MEAN	**0.231**	*1.0000*

The next step is to examine the relationship between blanket density and the coefficient c_4. Figure 42 illustrates the power regression fit for this relationship, and Table 17 lists the coefficient of determination and the regression relation.
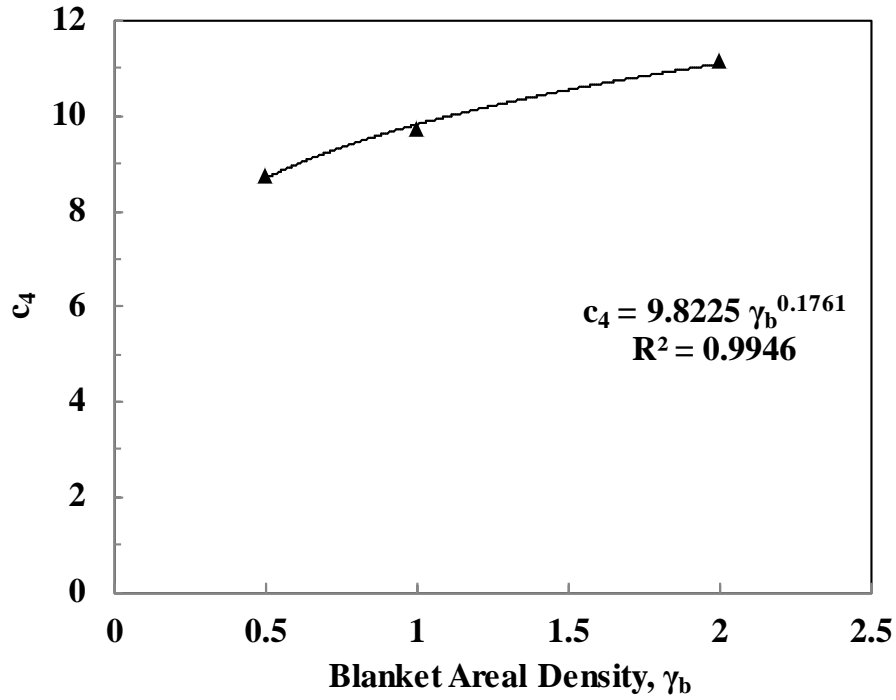
Figure 42. The coefficient c4 is related to blanket density through a power regression.

Table 17. The power regression between all parameters except array area.

	Regression: $\mu / L_{pb} \approx c_4\, n^{0.231}\, (af)^{0.216}$	
A	c_4	R^2
m^2		
2000	$9.823\,\gamma b^{0.176}$	0.9946

The relation presented in Table 17 is rearranged to form Eq. (66), the approximation model for all array architectures of the size *A = 2000 m²*.

$$\mu_{A=2000} \approx 9.823 L_{pb}(af)^{0.216}\, n^{0.231}\, \gamma_b^{0.176} \tag{66}$$

151

The final step in this approximation model development is to incorporate the array area, A. First, Eq. (66) is used to predict the beam efficiency index for all 2,430 design cases. These results are compared to the numerical model predictions of the beam efficiency index, and the results are grouped according to array area. The comparison is expected to produce no error for the largest area set and measurable error for the other data sets. For each area data set, a linear regression fit is used to generate a coefficient, c_6, that represents the ratio of numerical to approximate. A c_6 value of one would indicate a perfect fit between the numerical model and approximate model. The coefficients are listed in Table 18. Notice that the coefficient for the largest area data set is $c_6 = 1.000$ as expected since the approximation equation was developed using that data set. The values for c_6 are plotted in Figure 43 against the respective array area values. A power regression is shown to fit the data, approximating the relationship between c_6 and A.

Table 18. **The linear regression fit results between the beam efficiency index from the numerical model and that from the large area approximation model.**

| A | Regression: μ-numerical $\approx c_6$ μ-approximate | |
m^2	c_6	R^2
2000	1.000	0.9966
600	1.342	0.9943
200	1.749	0.9916
60	2.352	0.9877
10	3.698	0.9807
	MEAN	*0.9902*
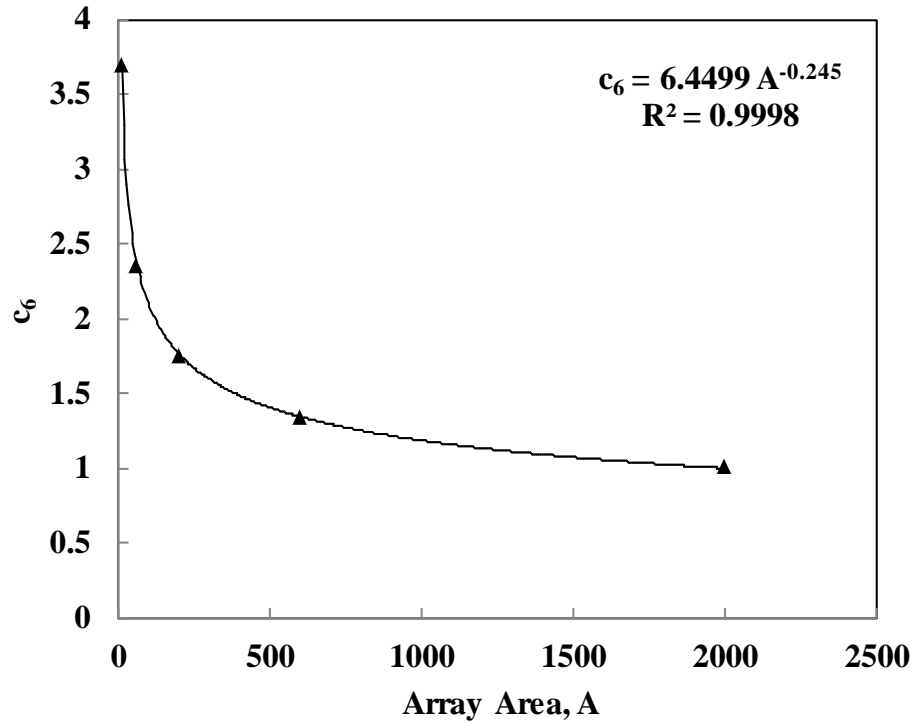
Figure 43. The coefficient c6 is related to array area.

The regression expression defining c_6 is then substituted into Eq. (67) to complete

the approximation model. Therefore Eq. (67) approximately represents the structural

scaling behavior of the full range of solar array architectures represented in this study.

$$\mu \approx c_6 \; 9.823 L_{pb} (af)^{0.216} \, n^{0.231} \, \gamma_b^{\,0.176}$$

$$\mu \approx 63.358 \frac{(af)^{0.216}}{A^{0.245}} L_{pb} n^{0.231} \gamma_b^{\,0.176} \tag{67}$$

This approximation model is checked for accuracy by comparing to the numerical

model predictions of beam efficiency index for all 2,430 design cases. Figure 44 shows

the comparison. A data point above the line represents the case where the approximation

model under-predicts the beam efficiency index, and a point above the line represents an

over-prediction. The statistical analysis listed on the figure shows relatively good

agreement across the full range. A closer inspection of the figure reveals especially good agreement for the lower beam efficiency values which is where the majority of design cases are represented.

The plot shows data points with the following annotations:

$\sigma = 32.277\,N^{3/5}\,m^{9/5}\,/\,kg$

$Maximum\ Deviation = 131.999\,N^{3/5}\,m^{9/5}\,/\,kg$

$Minimum\ Deviation = -411.967\,N^{3/5}\,m^{9/5}\,/\,kg$

$Mean\ Deviation = 8.660\,N^{3/5}\,m^{9/5}\,/\,kg$

y-axis: Numerical Model Beam Index, μ (0 to 2500)

x-axis: Approximation Model Beam Index, μ (0 to 2500)
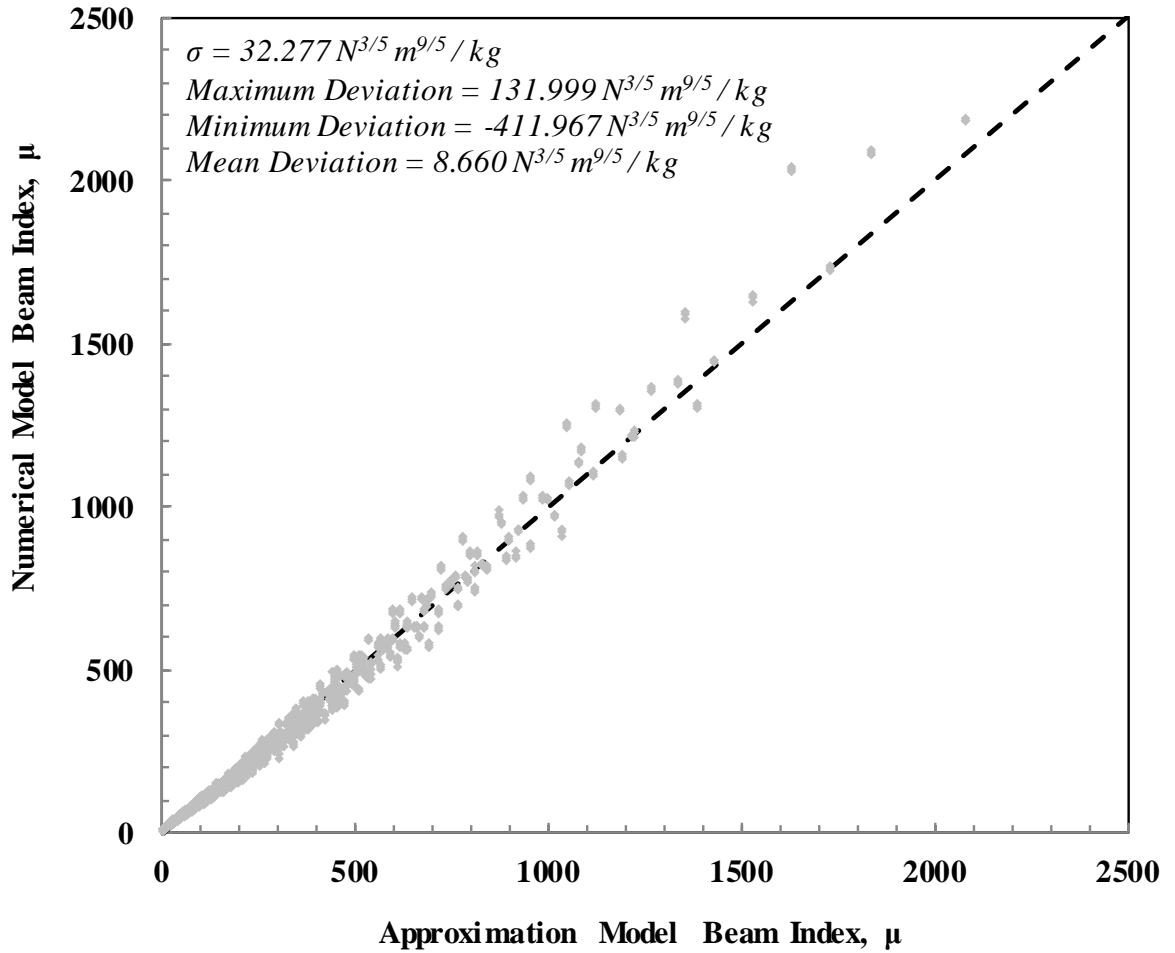
Figure 44. Fit goodness between the approximation model and the numerical model.

APPENDIX D. USER'S GUIDE

Metrics have recently been developed to quantify the structural scaling effects of rectangular flexible blanket solar arrays. The purpose of this guide is to define the practical usage of these metrics.

One challenge in the conceptual design of spacecraft is that thousands of structural design configurations are possible in meeting power generation, structural strength and fundamental frequency needs. It is not practical to analyze each solar array architecture variation in detail. The scaling metrics herein provide a means to evaluate all rectangular flexible blanket array architectures in a manner that is readily understandable and quickly usable for conceptual design purposes.

These metrics are intended to serve those comparing structural solar array architectures, those considering mission concepts, and those crafting technology investment strategies. These practical analytical tools should help to set investment trajectories on paths that are well-founded on structural mechanics principles. These early decisions represent large R&D investment commitments and thus must be guided toward concepts and technology components that promise only the highest payoff for the least cost.

Figure 45 provides a physical description of the generic solar array model used as the basis for developing these scaling metrics. The number of structural components and performance terms was selected in order to balance model accuracy and user simplicity. This model is defined by the unique assemblage of three structural components:

      1) Tensioned flexible blanket(s) to collect or transmit radiation energy,

2) Primary boom column(s) to react the tension, and

3) Spreader bar(s) to transfer load from the blanket to the column.

The array size is defined by the blanket area such that the length is equivalent to the primary boom length and the width is equivalent to the spreader bar length. The structural architecture is further defined by the quantity of primary booms used to deploy the blanket(s) and achieve system stiffness and strength. Primary booms are defined only by the structural performance they demonstrate: flexural stiffness, moment strength, and mass density. Neglecting the boom construction details allows direct comparison of drastically different boom types such as a truss of tubes to a rollable slit tube. The photovoltaic blanket is defined by an areal mass density and an areal power density—two terms dependent on the photovoltaic cell type chosen to populate the blanket. The spreader bar is characterized by linear mass density. The array performance is quantified by three terms:

1) Deployed area (e.g., power produced),

2) Acceleration load limit, and

3) Fundamental frequency of structural vibration.

The scaling parameters and scaling indices developed to characterize this array structural model are listed in Table 19 along with select related equations. To demonstrate the accuracy of these scaling metrics, the sprung mass is predicted of four heritage flexible blanket arrays: Terra, Milstar, International Space Station, and the MegaROSA ground prototype. The results of this comparison are summarized in Table 20.

156

a) General solar array model

Spreader Bar
[w_{sb}]

Primary Booms
[EI, M, w_{pb}, L, n]

Array Requirements
[f, a, A]

Photovoltaic Blanket
[γ_b]

Rigid Spacecraft Interface or
Backbone Boom

Scaling metrics represent the wings—backbones booms are considered separately

L_{pb}

Backbone Booms

2000 m^2

Yoke

Solar Array Drive Assy.

2000 m^2

2000 m^2

b) Small array, 10 m^2

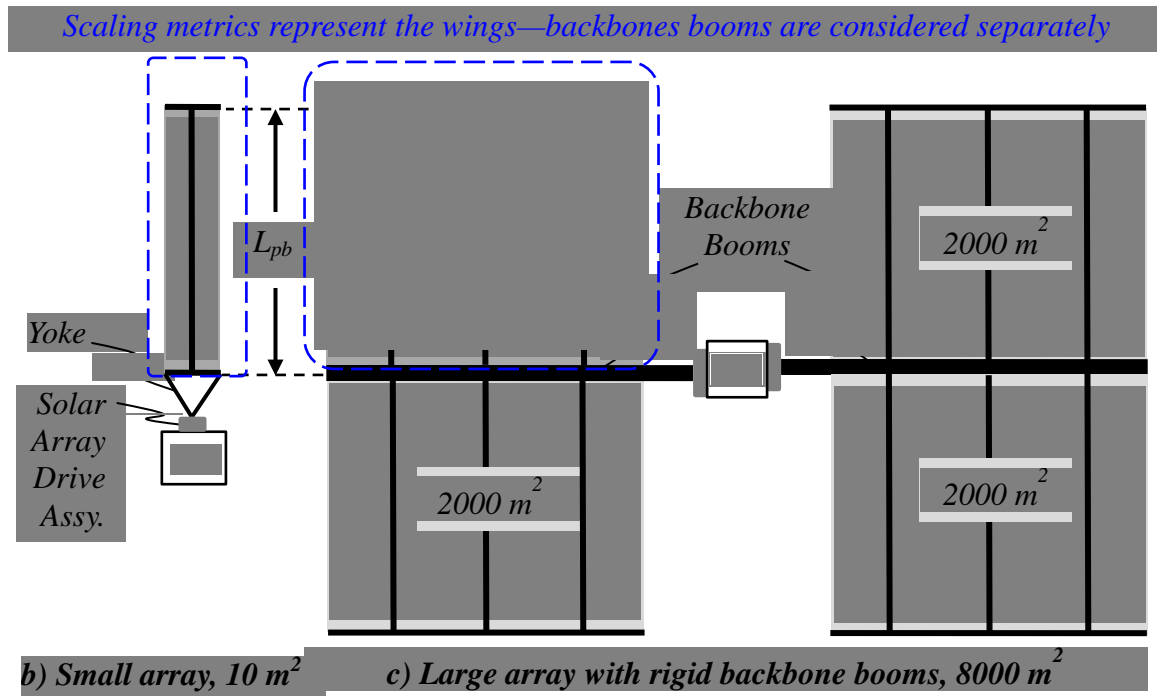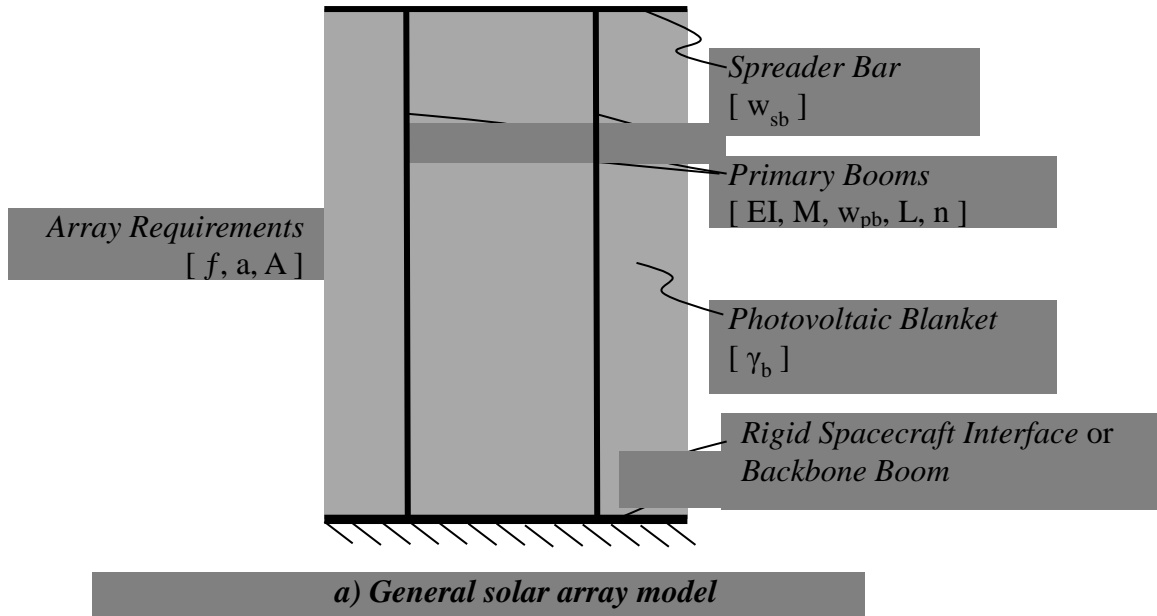*c) Large array with rigid backbone booms, 8000 m^2*

Figure 45. The general solar array model (a) assumes the root is fixed so that the array wing is treated independent of the root support whether it be a yoke (b) or backbone boom (c).

Table 19. Relevant equations and metrics.

Strength and Frequency		Units
Clamped-Free Beam-Cable Frequency	$f = \delta \dfrac{3.516}{2\pi}\left(\dfrac{EI}{wL^4}\right)^{1/2} \; ; \; \delta = 0.76$	Hz
Torsion/Bending Freqency Ratio	$\dfrac{f_{torsion}}{f_{bending}} = 1.5476\left(\dfrac{GJ}{EI}\right)^{1/2} AR$	Hz / Hz
Critical Euler Load (with cable follower)	$P_{cr} = \pi^2 \dfrac{EI}{L^2}$	N
Beam Moment from Rectilinear Accel.	$M = \dfrac{w(ag)L^2}{2}$	$N\text{-}m$
Beam Efficiency Index*	$\mu = \dfrac{\left(M^2 EI\right)^{1/5}}{w}$	$N^{3/5} m^{9/} / kg$
Cost and Mass		
Approximate Beam Efficiency Index	$\mu \approx 63.358 \dfrac{(af)^{0.216}}{A^{0.245}} L_{pb} n^{0.231} \gamma_b^{0.176}$	$N^{3/5} m^{9/5} / kg$
Approximate Sprung Areal Mass Density	$\gamma \approx 0.0024\left(63.358 \dfrac{(af)^{0.216}}{A^{0.245}} L_{pb} n^{0.231} \gamma_b^{0.176}\right)^{0.923} + \gamma_b + \dfrac{w_{sb}}{L_{pb}}$	kg / m^2
Scaling Parameters		
Scaling Parameter	$\eta = \dfrac{(af)^{0.216}}{A^{0.245}} L_{pb} n^{0.231} \gamma_b^{0.176}$	$m^{0.374} kg^{0.176} / s^{0.648}$
Requirements Scaling Parameter	$\eta_r = \dfrac{(af)^{0.216}}{A^{0.245}}$	$1 / (m^{0.274} s^{0.648})$
Architecture Scaling Parameter	$\eta_a = L_{pb} n^{0.231} \gamma_b^{0.176}$	$m^{0.648} kg^{0.176}$
Scaling Indices		
Scaling Index	$\kappa = (af)^{0.216} n^{0.231} L_{pb} A^{0.755} \dfrac{\gamma_b^{0.176}}{m}$	$m^{2.374} / (kg^{0.824} s^{0.648})$
Load Scaling Index	$\kappa_l = n^{0.231} L_{pb} A^{0.755} \dfrac{\gamma_b^{0.176}}{m}$	$m^{2.158} / kg^{0.824}$
Power Scaling Index	$\kappa_p = (af)^{0.216} n^{0.231} L_{pb} \dfrac{\gamma_b^{0.176}}{m}$	$m^{0.864} / (kg^{0.824} s^{0.648})$

*Murphey, T., "Booms and Trusses," Recent Advances in Gossamer Spacecraft, edited by
C. H. M. Jenkins, Progress in Astronautics and Aeronautics, Vol. 212, AIAA, Reston, VA, 2006, pp. 1–43.

Table 20. Metrics accuracy is demonstrated by predicting sprung mass of existing arrays.

		Terra	Milstar	ISS	Mega ROSA prototype	Units
Deployed PV Area	A	45.3	44.0	301	74.3	m^2
Root Mass Density	γ_r	1.09	0.857	0.574	0.172	kg/m^2
Boom Mass Density	γ_{pb}	0.077	0.102	0.463	0.135	kg/m^2
Blanket Mass Density	γ_b	1.66	1.22	1.20	1.07	kg/m^2
Spreader Mass Density	γ_{sb}	0.323	0.203	0.121	0.083	kg/m^2
Total Cantilever Mass Density	γ	*2.06*	*1.52*	*1.78*	*1.29*	*kg/m^2*
Predicted Cantilever Mass Density	γ	*1.81*	*1.46*	*1.65*	*1.32*	*kg/m^2*
% Error		**-12%**	**-4%**	**-7%**	**3%**	

D.1   Assumptions and Limitations

To provide the user with the proper context for application, major assumptions surrounding the development of these scaling metrics are listed as follows:

1) The array geometry is rectangular and the columns are arranged in parallel.

2) The photovoltaic blanket(s) is represented dynamically as a cable(s).

3) The array limit loading is a rectilinear acceleration applied at the spacecraft bus in the direction normal to the plane of the array. Example sources of this load: thruster impulse or docking maneuver. Rotational acceleration loads are not considered due to their lesser magnitude.

4) The array failure load occurs as an identical maximum moment at the base of each beam-column under the combined axial compression and moment

loading. The maximum beam strength is therefore the maximum moment the beam can endure (including any design margin) while subjected to an axial compressive load from the blanket.

5) The axial compression load in each column is assumed to be a constant 21% of the critical Euler buckling load.

6) The array fundamental frequency of structural vibration oscillates in an out-of-plane motion similar to that of a cantilever beam. This mode shape is assumed to be preferred over a torsion mode due to spacecraft control challenges of the latter.

7) Array fundamental frequency considers the mass of the spreader bar to be distributed along the column length. This is justified as long as the spreader bar mass is less than 10% the total array mass.

8) Array mass equation accounts for only the sprung mass—blanket(s), compression column(s), and spreader bar(s).

9) The root boundary is assumed rigid. Practically, the root boundary is the yoke, Solar Array Drive Assembly, or backbone boom.

10) Dimensional stability is not considered as a performance constraint thus these metrics are not appropriate to characterize precision structures such as antenna and optical apertures.

11) The metrics are relevant over the parameter space listed in Table 21.

Table 21. Practical array design ranges that bound the validity of the metrics.

		Range	Units
Objective Constraint			
Areal Mass Density	γ	0 - 10	kg/m^2
Array Performance Parameters			
Fundamental Frequency	f	0.001 - 5	Hz
Lateral Acceleration Load	a	0.001 - 0.2	$9.81\ m/s^2$
Deployed Area	A	10 - 2000	m^2
Primary Boom Properties			
Beam Efficiency Index	μ	1 - 5000	$N^{3/5}m^{9/5}/\ kg$
(Flexural Stiffness)	EI	--	$N\ m^2$
(Moment Strength)	M	--	$N\ m$
Structural Mass Fraction	β	0.01 - 0.5	kg/kg
(Linear Mass Density)	w_{pb}	--	kg/m
Length	L_{pb}	5 - 30	m
Boom Quantity	n	1 - 10	--
Blanket Properties			
Areal Mass Density	γ_b	0.5 - 2.0	kg/m^2
Spreader Bar Properties			
Linear Mass Density	w_{sb}	1 - 5	kg/m

D.2   Array Requirements Trade

One practical use of these metrics is to compare the effects of different

architectures on array performance. This is helpful when requirements are in flux, and an

understanding of the array mass and cost penalties may help influence the definition of

power production, acceleration load limit, and fundamental frequency requirements.

The array scaling parameter provides a single numerical value by which array

structural architectures may be compared on the basis of minimum mass and minimum

beam efficiency. Beam efficiency in this case is synonymous with beam cost—monetary

cost, packaged volume cost, and mechanism complexity cost. The scaling parameter is

related to the beam efficiency in Figure 46 showing the parameter to essentially be a penalty parameter. As each term in the parameter grows, the beam efficiency must grow proportionally to maintain minimum array mass. If specific array architectures reside in the upper left-hand quadrant of this figure, the beam efficiency is unnecessarily high; the array mass savings gained are comparatively low. On the other hand, architectures that fall in the lower right-hand quadrant have low beam efficiency, and the array mass is severely penalized as a result. Neither extreme quadrant is desirable.

Each term in the scaling parameter has a unique influence on this balance between array mass and beam cost. The scaling proportionalities shown at the top of Figure 46 illustrate the relative influence of each on beam efficiency. For example, cutting array length in half while maintaining all other terms equal, cuts the beam index by one half due to the direct proportionality. On the contrary, cutting the blanket density in half yields only a 0.11 reduction in beam efficiency. Surprisingly, cutting the array area in half while maintaining constant length raises the required beam efficiency index by 1.18. The conclusion is that long, narrow arrays are not as mass efficient as short, wide arrays.

The scaling index shows a similar trend as the scaling parameter except it is shown with respect to structural mass fraction rather than to beam efficiency. This index is separated for convenience into the load scaling index and the power scaling index, differentiated only by the respective loading and area terms removed. Figure 47 and Figure 48 illustrate these two indices with respect to mass fraction showing that as array loading and area grow, the structural mass fraction grows in proportion. Larger, higher loaded arrays require greater structural mass than the counter scenario.

$$0.5\,L \sim 0.50\,\mu$$
$$0.5\,n \sim 0.85\,\mu$$
$$0.5\,(af) \sim 0.86\,\mu$$
$$0.5\,\gamma_b \sim 0.89\,\mu$$
$$0.5\,A \sim 1.18\,\mu$$

Beam Efficiency Index, $\mu = \dfrac{(M^2 EI)^{1/5}}{w}$

$\mu = 63.358\eta$

Overly Costly Beam-Column

Balanced Mass and Complexity

Overly Massive Array

Terra

Milstar ISS

a)

b)

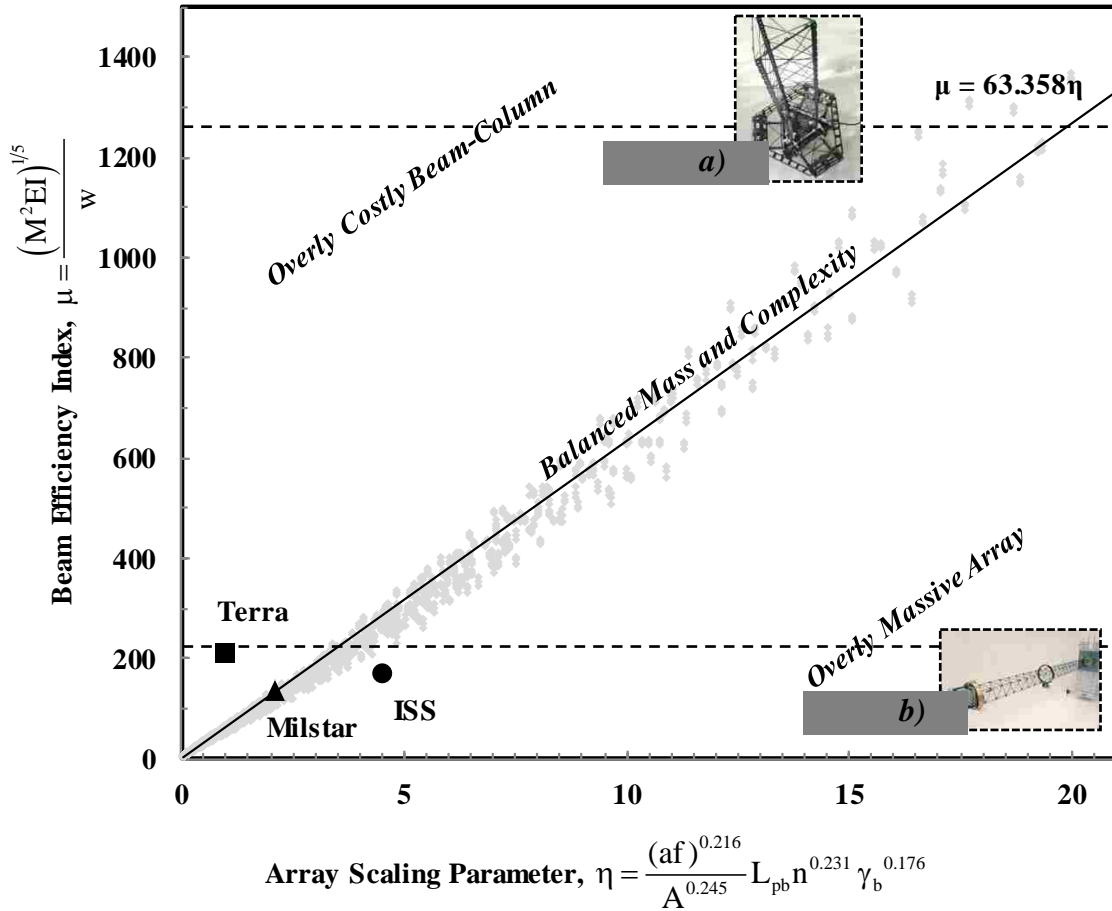Array Scaling Parameter, $\eta = \dfrac{(af)^{0.216}}{A^{0.245}} L_{pb} n^{0.231} \gamma_b^{0.176}$

Figure 46. The beam efficiency index is related to the solar array scaling parameter. The (a) ATK Trilok®, $\mu = 1268\ N^{3/5} m^{9/5}/kg$, and (b) S2 Coilable, $\mu = 224\ N^{3/5} m^{9/5}/kg$, booms are shown as examples.

Figure box content:

$$0.5\,L \sim 0.50\,\beta$$
$$0.5\,A \sim 0.59\,\beta$$
$$0.5\,n \sim 0.85\,\beta$$
$$0.5\,(af) \sim 0.86\,\beta$$
$$0.5\,\gamma_b \sim 0.89\,\beta$$

Y-axis: **Structural Mass Fraction**, $\beta = \dfrac{m_{pb}}{m}$

X-axis: **Load Scaling Index**, $\kappa_1 = n^{0.231} L_{pb}\, A^{0.755}\, \dfrac{\gamma_b^{0.176}}{m}$

Labels within plot:
- $(a\,f) = 1$ Hz-m/s^2
- $(a\,f) = 0.01$ Hz m/s^2
- $(a\,f) = 0.00001$ Hz m/s^2
- 20% CIGS, 400 m^2
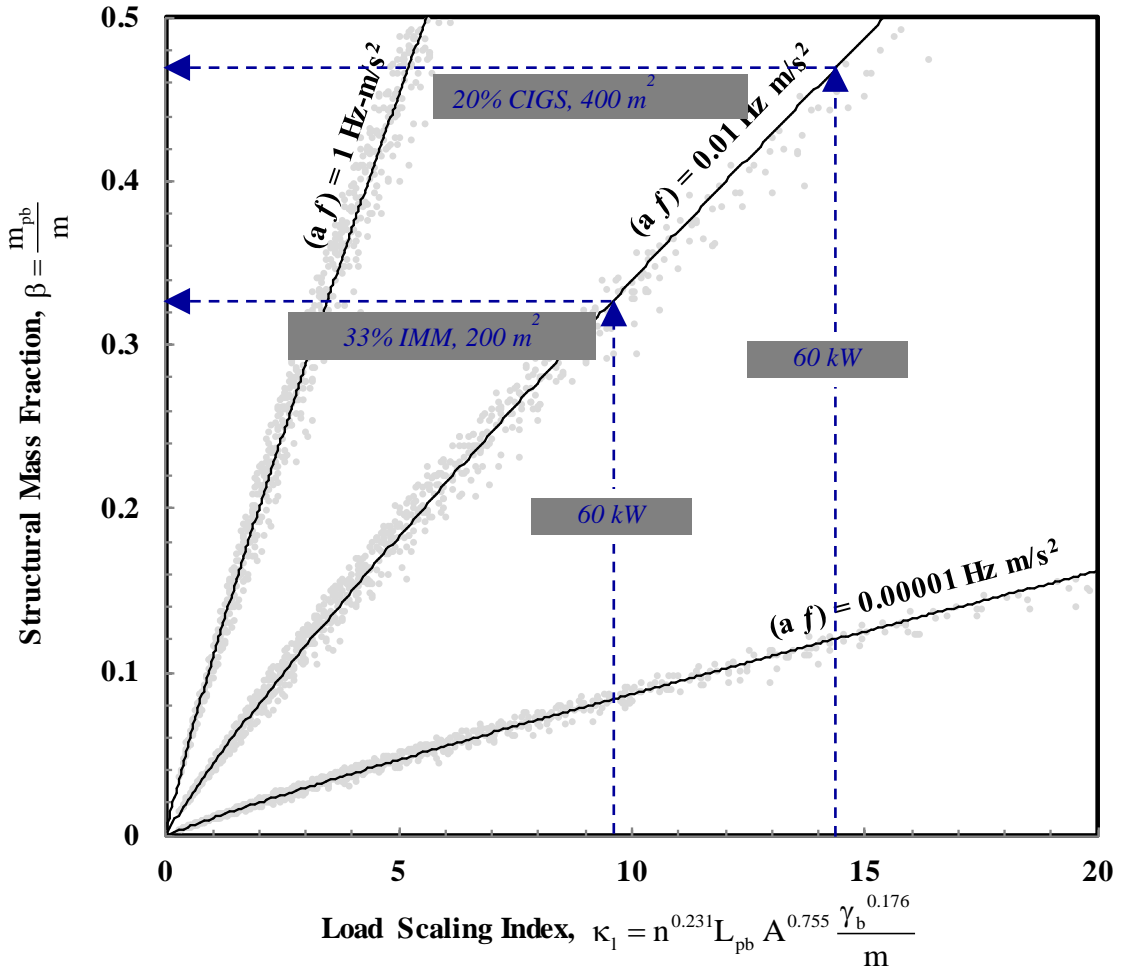- 33% IMM, 200 m^2
- 60 kW
- 60 kW

Figure 47. Load scaling index related to array structural mass fraction for three acceleration and frequency values. Two example 60kW cases illustrate the structural mass fraction difference between a blanket of 20% thin film CIG cells and one with 33% IMM cells, all other design parameters being equal.
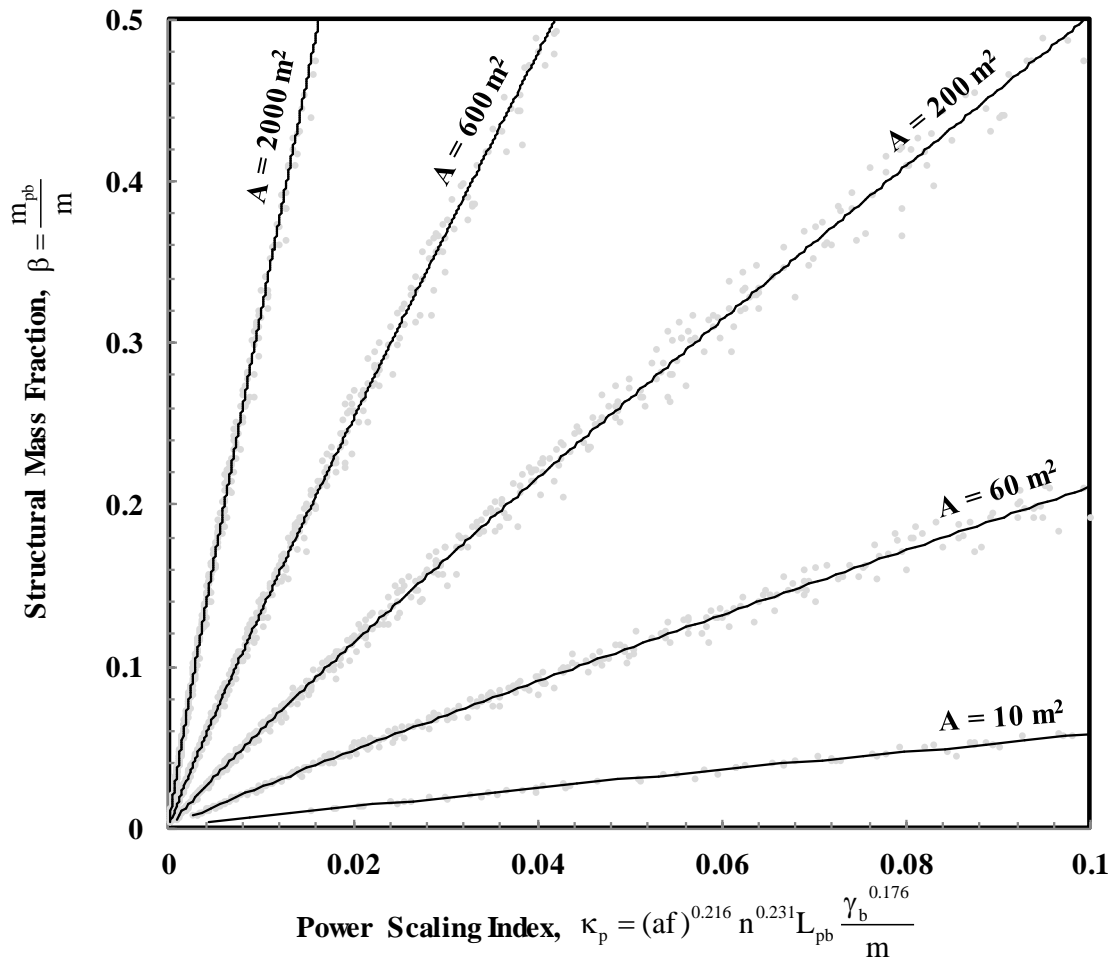
Figure 48. Power index related to structural mass fraction for a wide range of array areas to show the relative structural mass penalty of increasing the loading, length, blanket mass, and boom quantity.

D.3   Array Architecture Trade

A second practical use of these metrics is to compare and in some cases create

conceptual solar array structural architectures. Using the metrics for this purpose

requires knowledge of the three primary requirements: beginning of life (BOL) power

production, fundamental frequency of structural vibration, and maximum on-orbit

acceleration load.

As an example, consider a communications spacecraft in geosynchronous orbit.

The power required at the beginning of service life is 30 kW. The expected acceleration

load is relatively high, *ag = 0.1 gees (0.981 m/s^2)*, and the minimum fundamental

frequency required is *f = 0.1 Hz.* Two different photovoltaic cells are being considered.

The first is state-of-practice triple junction XTJ/UTJ cells with 29.5% BOL efficiency

(AM0) as documented in Table 22. The second cell type is a four-junction Inverted

Metamorphic cell that operates at 33% efficiency. These two cell types generate

approximately 250 W/m^2 and 290 W/m^2 respectively. Therefore the total required

deployed area for each 15 kW wing is 60 m^2 and 52 m^2 respectively. The areal mass

density of the blanket when populated with these cells strung together at a nominal

operating voltage of 70 V is γ_b = *1.5 kg/m^2.*

Now that the performance requirements have been established, four different

structural architecture cases are considered. The first case uses the 29.5% efficient cells

and is constructed with a single blanket 30 meters long by 2 meters wide, supported by a

single beam-column. The scaling parameter for this case is calculated to be *η = 5.08*

from the equation in Table 19. This value, when plotted on Figure 46 or multiplied by the

constant 63.358, correlates to a minimum required beam efficiency index of $\mu = 322$. The array sprung mass is estimated from the equation in Table 19 to be $m = 122\ kg$.

The second case uses the same 29.5% efficient cells but is shorter, 10 meters long by 6 meters wide, and is supported by two beam-columns instead of one. The scaling parameter for this case is less than half that of the first case, $\eta = 1.99$. The required beam efficiency index is also less than half, $\mu = 126$, and the total mass is reduced to $m = 108\ kg$. One conclusion to be drawn is that the penalty paid for using two columns is easily overcome by the benefits of the shorter, wider aspect ratio of case 2 over case 1. The payoff of the reduced beam index is reduced beam structural hierarchy and thus reduced cost.

The third case considers the upgraded cells, 33% efficient IMM type, yielding a boost in conversion efficiency from 29.5% to 33%. The same width and boom quantities as case 2 are maintained but the array length is reduced to 8.7 meters because of the lesser area. The scaling parameter then reduces to $\eta = 1.79$. The minimum required beam efficiency index is $\mu = 113$, and the total mass is $m = 94\ kg$. Both terms are lower than those of case 2 by 10% and 13% respectively and are much lower than those of case 1 by 65% and 23% respectively. The beam efficiency index (i.e., beam cost) reduction is a direct result of reducing the array area length from 10 meters to 8.7 meters, and the mass reduction is a result of reducing the area from 60 m^2 to 52 m^2.

Case 3 emerges as the lightest weight, lowest cost structural architecture given the communications mission requirements. Of course, these quantitative results are not taken simply at face value. They are deliberated alongside other subjective design

considerations such as the added cost of higher efficiency IMM cells. But even if these cells are cost prohibitive, case 2 remains the better structural architecture than case 1. Other considerations also enter the decision process such as beam packaged volume and mechanism complexity. But case 2 requires a lesser beam efficiency than case 1, meaning the structural hierarchy may be relaxed from perhaps a truss of solid rods to a rollable slit tube.

These array concepts must also be checked for the fundamental mode of structural vibration. Bending modes are preferred over torsion modes due to the associated spacecraft control challenges of a torsion mode over bending. Figure 49 is consulted. Case 1 uses a single column but has a large aspect ratio, *AR = 15*, so the GJ/EI ratio required to ensure a bending mode is relatively low *GJ/EI = 0.002*. If the aspect ratio of this single column architecture drops below the threshold indicated on this figure, the fundamental mode becomes torsion not bending. For cases 2 and 3, the torsion mode is possible due to the small aspect ratio but is not likely to dominate due to the shear-frame effect of having two columns joined at the tip by a spreader bar.

This same comparison approach may be used to compare arrays with backbone booms. Case 4 is provided in Table 23 as an example. Once the conceptual array architecture(s) have been selected, the aspect ratio is plotted on Figure 49 to determine the minimum required backbone boom GJ/EI ratio to maintain a bending vibration mode rather than torsion. For case 4, this minimum ratio is *GJ/EI = 0.982*. Further sizing of the backbone boom may be accomplished by lumping the array mass onto the backbone and selecting a bending stiffness such that the fundamental frequency is less than ½ the

wing fundamental frequency. A lower backbone frequency helps to ensure the spacecraft does not have to deal with symmetric modes of vibration caused by multiple, identical array winglets vibrating at similar frequencies—a scenario that is very difficult to sense and control using typical spacecraft determination and control actuators such as torque rods, momentum wheels, and control moment gyroscopes.

One cautionary note is that the array mass predicted herein accounts for the sprung mass of the array only. The sprung mass includes all components that contribute to frequency and strength calculations such as the primary booms, blankets, spreader bars, and anything fixed to the spreader bars. If the user desires to approximate the total array mass, the un-sprung components must be considered separately. Examples of un-sprung mass include blanket boxes, deployment mechanisms, and restraint devices.

Table 22. Survey of flexible blanket areal mass density and areal power density.

Cell Efficiency and Type	γ (kg/m^2)	ε (W/m^2)	measured, m projected, p
13% Thin Film, a-Si	0.5-2.5	95-113	m
15% Thin Film, 1J CIGS	0.5-2.5	110-130	p
20% Thin Film, 2J CIGS	0.5-2.5	147-173	p
29.5% 3J XTJ/ZTJ**	1.0-2.0	250-280	m
33% 3J IMM	1.0-2.0	290-320	m
35% 4J IMM	1.0-2.0	307-340	p
38% 6J IMM	1.0-2.0	334-368	p
29.5% XTJ/ZTJ, 8x Stretched Lens Array	0.6-1.4	350-420	p
38% 6J IMM, 8x Stretched Lens Array	0.6-1.4	450-540	p

Table 23. 30kW communications satellite array architecture comparison and a larger backbone boom architecture example.

|		Case 1	Case 2	Case 3	Case 4	Units
Requirements Input						
Wing Power (BOL)	–	15	15	15	100	kW
PV Cell Efficiency	–	29.5	29.5	33	33	%
Wing Area	A	60	60	52	345	m^2
Acceleration Load	a	0.1	0.1	0.1	0.1	9.81 m/s^2
Fundamental Frequency	f	0.2	0.2	0.2	0.2	Hz
Size Input						
Length	L_{pb}	30	10	8.7	15	m
Width	W	2	6	6	23	m
Boom Quantity	n	1	2	2	5	–
Blanket Mass Density	γ_b	1.5	1.5	1.5	1.5	kg/m^2
Spreader Bar Mass	w_{sb}	1	1	1	3	kg/m
Results						
Array Scaling Parameter	η	5.08	1.99	1.79	2.40	$m^{0.374} kg^{0.176} / s^{0.648}$
Requirements Parameter	η_r	0.158	0.158	0.163	0.103	$1 / (m^{0.274} s^{0.648})$
Architecture Parameter	η_s	32.2	12.6	11.0	23.4	$m^{0.648} kg^{0.176}$
Array Scaling Index	κ	2.50	1.10	0.99	1.23	$m^{2.374} / (kg^{0.824} s^{0.648})$
Minimum Beam Efficiency	μ	322	126	113	152	$N^{3/5} m^{9/5} / kg$
Wing Mass	m	122	108	94	672	kg
Mass Reduction from Case 1	–	–	11%	23%	–	–
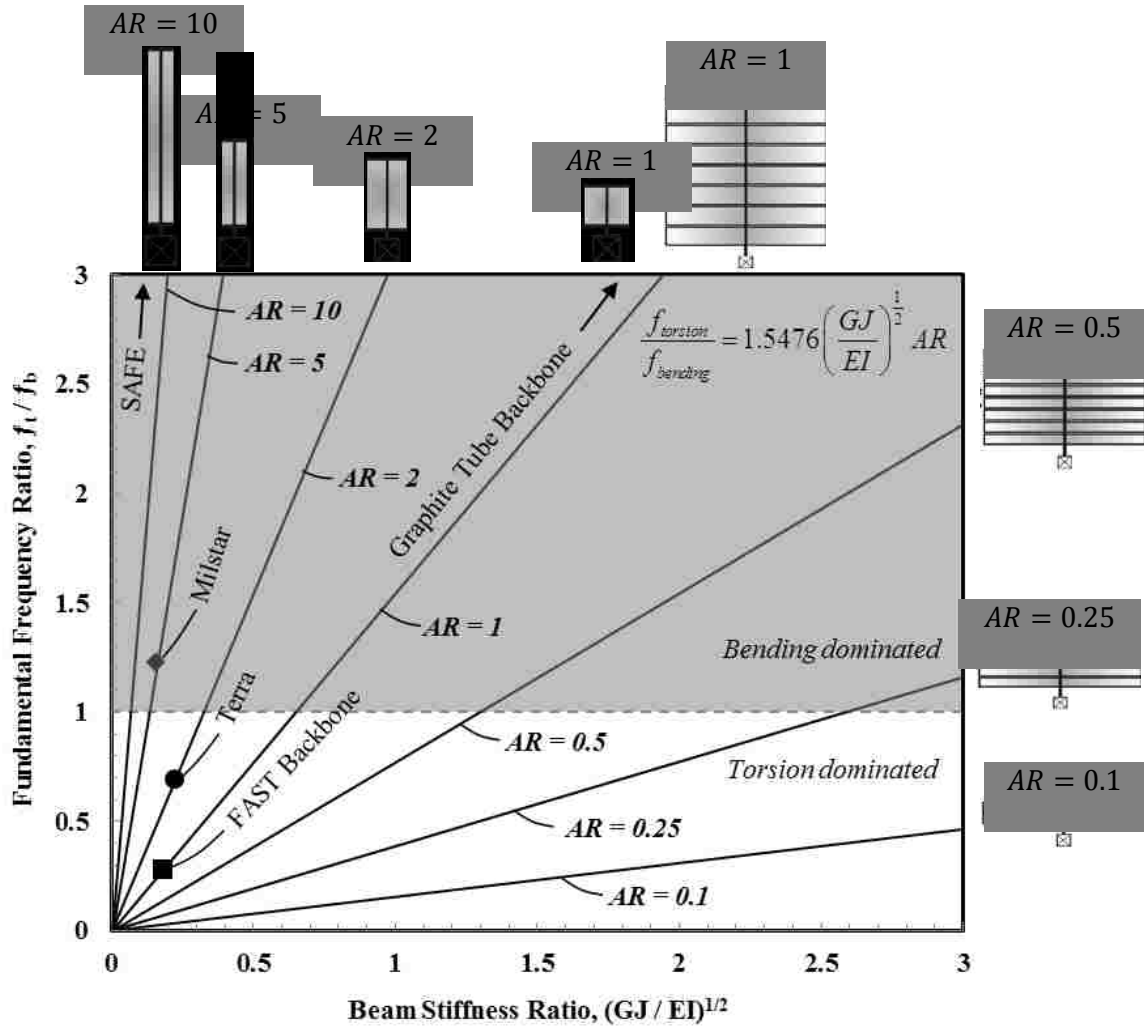
Figure 49. Array aspect ratio and the support beam stiffness ratio related to the fundamental mode of structural vibration—bending or torsion.

REFERENCES

[1] Green, M. A., "Solar Cells: Operating Principles, Technology and System Applications." Kensington: The University of New South Wales, 1992. pp. 2.

[2] Jones, P., Spence, B., "Spacecraft Solar Array Technology Trends," *Proceedings of the IEEE Aerospace Conference*, Vol. 1, Aspen, Colorado, 21-28 March 1998, pp. 141-152.

[3] Felkel, E., Wolff, G., "Flexible Rolled-Up Solar Array," Air Force Aero Propulsion Laboratory, Technical Report AFAPL-TR-72-61, Wright Patterson AFB, OH, 30 June 1972.

[4] Thornton, E., Kim, Y., "Thermally Induced Bending Vibrations of a Flexible Rolled-Up Solar Array," *AIAA Journal of Spacecraft and Rockets*, Vol. 30, No. 24, 1993, pp. 438-448.

[5] Thornton, E., Chini G., Gulick, D., "Thermally Induced Vibrations of a Self-Shadowed Split-Blanket Solar Array," *35th AIAA Structures Structural Dynamics and Materials Conference,* AIAA-94-1379, Hilton Head, SC, 18-20 April 1994.

[6] Kurland, R., Schurig, H., Rosenfeld, M., Herriage M., Gaddy, E., Keys, D., Faust, C., Andiario, W., Kurtz, M., Moyer, E., "Terra Flexible Blanket Solar Array Deployment, On-Orbit Performance and Future Applications," *28th IEEE Photovoltaic Specialists Conference*, 22 September 2000, Anchorage, AK.

[7] Gibb, J., "MILSTAR's Flexible Substrate Solar Array—Lessons Learned." *26th Aerospace Mechanisms Symposium*, Goddard Space Flight Center, 1992.

[8] Lindberg, D., "A 928-m^2 (10,000 ft^2) Solar Array," *7th Aerospace Mechanisms Symposium*, Manned Spacecraft Center, Houston, Texas, 7-8 September 1972.

[9] Beidleman, N., Freebury, G., Francis, W., Lake, M., Barrett, R., Kellar, P., Taylor, R., "Large-Scale Deployable Solar Array. United States Patent 7806370. 5 October 2010.

[10] Davis, G., Gohardani, A., Murphy, D., White, S., "Quest for Electricity Helps Power Space Structures Work," *AIAA Aerospace America,* Vol. 15, No. 11, December 2013, pp. 8.

[11] Stribling, R., Schwartz, J., "Deployable Solar Array Assembly." United States Patent 6983914. 10 June 2006.

[12] Crawford, R., Hedgepeth, J., Preiswerk, P., "Spoked Wheels to Deploy Large Surfaces in Space" Final Report NASA CR-2347, Contract NAS2-6731, ARC-R-1004, January, 1975.

[13] Harvey, J., Jones, A., "Lightweight Stowable and Deployable Solar Cell Array." U.S. Patent 5296044. 22 March 1994.

[14] White, S. Douglas, M., Takeda, R., Spence, B., Gregory, N., Schmidt, J., Sorensen, P., "Solar Arrays." United States Patent Application 11/944061. 21 May 2009.

[15] Murphy, D., "MegaFlex – The Scaling Potential of UltraFlex Technology." *53rd AIAA Structures, Structural Dynamics and Materials Conference*, AIAA-2012-1581, Honolulu, Hawaii, 23-26 April 2012.

[16] Wagner, H., "Remarks on Airplane Struts and Girders Under Compressive and Bending Stresses, Index Values." National Advisory Committee for Aeronautics (NACA), TM No. 500, June 1929.

[17] Goodier, J., Thomson, W., "Applicability of Similarity Principles to Structural Models." National Advisory Committee for Aeronautics (NACA), TN No. 933, July 1944.

[18] Shanley, F. R., "Weight-Strength Analysis of Aircraft Structures." New York: McGraw-Hill, 1952.

[19] Hedgepeth, J., "Critical Requirements for the Design of Large Space Structures." NASA Final Report, No. 3484, Contract NAS1-15347. November 1981.

[20] Mikulas, M., "Structural Efficiency of Long Lightly Loaded Truss and Isogrid Columns for Space Applications." NASA, TM No. 78687,July 1978.

[21] Mikulas, M., Collins, T., Doggett, W., Dorsey, J., Watson, J., "Truss Performance and Packaging Metrics." *American Institute of Physics (AIP) Space Technology and Applications International Forum (STAIF),* 12-16 February 2006. AIP Conference Proceedings, Vol. 813. pp. 1000-1009.

[22] Murphey, T., "Booms and Trusses," Recent Advances in Gossamer Spacecraft, edited by C. H. M. Jenkins, *Progress in Astronautics and Aeronautics*, Vol. 212, AIAA, Reston, VA, 2006, pp. 1–43.

[23] Murphey, T., "Symbolic Equations for the Stiffness and Strength of Straight Longeron Trusses." *47ᵗʰ AIAA Structures, Structural Dynamics and Materials Conference*, AIAA 2006-2123, Newport, Rhode Island, 1-4 May 2006.

[24] Williams, J., Mikulas, M., "Analytical and Experimental Study of Structurally Efficient Composite Hat-Stiffened Panels Loaded in Axial Compression." *16ᵗʰ AIAA Structures, Structural Dynamics, and Materials Conference*, AIAA 1975-754, Denver, Colorado, 27-29 May 1975.

[25] Anderson, M., Bohon, H., Mikulas, M., "A Structural Merit Function for Aerodynamic Decelerators", NASA TN-5535, November 1969.

[26] Kaplan, R., "Deployable Reflector Structure." United States Patent 4030102. 14 June 1977.

[27] Crawford, R., Hedgepeth, J., Preiswerk, P., "Spoked Wheels to Deploy Large Surfaces in Space" Final Report NASA CR-2347, Contract NAS2-6731, ARC-R-1004, January, 1975.

[28] Harvey, J., Jones, A., "Lightweight Stowable and Deployable Solar Cell Array." United States Patent 5296044. 22 March 1994.

[29] White, S. Douglas, M., Takeda, R., Spence, B., Gregory, N., Schmidt, J., Sorensen, P., "Solar Arrays." United States Patent Application 11/944061. 21 May 2009.

[30] Murphy, D., "MegaFlex – The Scaling Potential of UltraFlex Technology." *53rd AIAA Structures, Structural Dynamics and Materials Conference*, AIAA-2012-1581, Honolulu, Hawaii, 23-26 April 2012.

[31] Rauschenbach, H., Bashin, S., Smith, B., "Ultra Lightweight Folding Panel Structure." United States Patent 4384163. 17 May 1983.

[32] Kurland, R., Stella, P., "Advanced Photovoltaic Solar Array Program Status." *Proceedings of the 24th Intersociety Energy Conversion Engineering Conference*, August 6-11, 1989, Washington DC, Vol. 2, pp. 829-834.

[33] Kimber, R., Regalado, O., Wu, C., "The EOS-AM Solar Array—A Flexible GaAs/Ge Array." *23rd IEEE Photovoltaic Specialists Conference*, Louisville, KY, 10-14 May 1993, pp 1375-1380.

[34] Gerlach, L., Marks, G.W., Quittner, E., Renshall, J., Zwanenburg, R., "The Design of the L-SAT (Olympus) Solar Array," *Proceedings of the 3rd European Symposium on Photovoltaic Generators in Space*, Bath, 4-6 May 1982. pp. 241-248.

[35] National Aeronautics and Space Administration Marshall Space Flight Center, "Solar Array Flight Experiment Final Report." Contract NAS-8-31352 April 1986.

[36] Benton, M., Jones, A., Spence, B., McCutcheon, E., Devillier, C., "Solar Array for Satellite Vehicles." United States Patent 5961738. 5 Oct 1999.

[37] Murphy, D., Foster, M., "Solar Array for Satellite Vehicles." United States Patent 6423895. 23 July 2002.

[38] Murphey, T., Dumm, H.P., "Blanket Solar Array with Z-Folded Truss." United States Patent Application 12/55012. 3 Sept 2009.

[39] Mejia-Ariza, J., Murphey, T., Dumm, H.P., "Deployable Trusses Based on Large Rotation Flexure Hinges," *AIAA Journal of Spacecraft and Rockets*, Vol. 47, No. 6, November-December 2010, pp. 1053-1062.

[40] Beidleman, N., Freebury, G., Francis, W., Lake, M., Barrett, R., Kellar, P., Taylor, R., "Large-Scale Deployable Solar Array." United States Patent 7806370. 5 Oct 2010.

[41] Foster, C., Tinker, M., Nurre, G., Till, W., "Solar-Array-Induced Disturbance of the Hubble Space Telescope Pointing System." *AIAA Journal of Spacecraft and Rockets*, Vol. 32. No. 4. July-August 1995, pp. 634-644.

[42] United States Air Force Small Business Innovative Research Website "Ultra-Lightweight Elastically Self-Deployable Roll-Out Solar Array (ROSA) for Responsive Space." 2010 Award 93287, Contract FA9453-10-C-0040, [URL: http://www.sbir.gov/sbirsearch/detail/3721]

[43] Stribling, R., Schwartz, J., "Deployable Solar Array Assembly." United States Patent 6983914. 10 June 2006.

[44] Stribling, R., Dommell, C., Streett, A., Cokin, D., Larson, B., "Boeing Advanced Modular Power Systems." *29th Space Power Workshop*, Los Angeles, California, 18-21 April 2011.

[45] Murphy, D., "Structures Including Synchronously Deployable Frame Members and Methods of Deploying the Same." United States Patent 7211722. 1 May 2007.

[46] Rimrott, F.P.J, "Storable Tubular Extendable Member - A Unique Machine Element," *Journal of Machine Design*, Vol. 37, 1965. pp. 156-165.

[47] Hazelton, C.S., Gall, K.R., Abrahamson, E.R., Denis, R.J., Lake, M.S., "Development of a Prototype Elastic Memory Composite (STEM) for Large Space Structures," *44th AIAA Structures, Structural Dynamics and Materials Conference*, AIAA 2003-1977, Norfolk, Virgina, 7-10 April 2003.

[48] Aguirre, M., "Collapsible Tube Mast," *Proceedings of the 2nd European Space Mechanisms & Tribology Symposium*, Meersburg, Germany, 9-11 October 1985, pp. 75.

[49] Unda, J., Weisz, J., Rivacoba, J., Ruiz Urien, I., "Family of Deployable Retractable Structures for Space Applications," *Acta Astronautica* Vol. 32, No. 12, 1994, pp. 767-784.

[50] Herbeck, L., Eiden, M., Leipold, M., Sickinger, C., Unckenbold, W., "Development and Test of Deployable Ultra-Lightweight CFRP-Booms for a Solar Sail." *European Conference on Spacecraft Structures, Materials and Mechanical Testing*, ESASP-468, Noordwijk, The Netherlands, 29 November – 1 December 2001, pp.107.

[51] Banik, J., Murphey, T., "Performance Validation of the Triangular Rollable and Collapsible Mast," *24th AIAA/USU Conference on Small Satellites*, SSC10-II-1. Logan, Utah, 2010.

[52] Murphey, T. W., Banik, J. A., "Triangular Rollable and Collapsible Boom," United States Patent 7895795, 1 March 2011.

[53] Adler, A., Hague, T., Spanjers, G., Engberg, B., Gooding, J., Murphy, D., Mikulas, M., "PowerSail: The Challenges of Large, Planar, Surface Structures for Space

Applications" *44th AIAA Structures, Structural Dynamics and Materials Conference*, AIAA 2003-1828, Norfolk, Virginia, 7-10 April 2003.

[54] Murphey, T., Botke, M., Blankinship, R., Hague, T., "An Articulated Motion and Vibration Isolator for Spacecraft" *44th AIAA Structures, Structural Dynamics and Materials Conference*, AIAA 2003-1829, Norfolk, Virginia, 7-10 April 2003.

[55] Murphey, T., "Solar Array Structural Architecture Fundamentals" *28th Space Power Workshop*, Los Angeles, California, 19-22 April 2010.

[56] Murphey, T., Cliff, E., Lane, S., "Matching Space Antenna Deformation Electronic Compensation Strategies to Support Structure Architectures." *IEEE Transactions on Aerospace and Electronic Systems*, Vol. 46, No. 3, July 2010. pp 1422-1436.

[57] Lake, M., Peterson, L., Levine, M., "Rationale for Defining Structural Requirements for Large Space Telescopes." *AIAA Journal of Spacecraft and Rockets*. Vol. 39, No. 5, September-October 2002. pp. 674-681.

[58] Schock, R., "Solar Array Flight Dynamics Experiment." *Workshop on Structural Dynamics and Control Interaction of Flexible Structures*, NASA Marshall Space Flight Center, Alabama, 22-24 April 1986.

[59] Reed, B., "What's Next?" *Space Power Workshop*, Los Angeles, California, 19-22 April 2011.

[60] Murphy, D., Eskenazi, M., White, S., Spence, B., "Thin-Film and Crystalline Solar Cell Array System Performance Comparisons" *29th Photovoltaic Specialist Conference*, 19-24 May 2002. pp 782-787.

[61] Hoffman, D., Kerslake, T., Hepp, A., Jacobs, M., Ponnusamy, D., "Thin-Film Photovoltaic Solar Array Parametric Assessment," *35th Intersociety Energy Conversion Engineering Conference and Exhibit Collection of Technical Papers*, AIAA-2000-2919, Vol. 1 (A00-37701 10-44), Las Vegas, Nevada, 24-28 July 2000, pp. 670-680.

[62] Boeing Company Press Release, "Boeing 702 HP Fleet" Accessed 30 November 2011 [URL: http://www.boeing.com/defense-space/space/bss/factsheets/702/702 fleet.html]

[63] Loral Company Press Release, "Space Systems/Loral Selected to Provide Two High-Power Satellites to Intelsat" 31 December 2008. Accessed 30 November 2011. [URL: http://investor.loral.com/releasedetail.cfm?ReleaseID=357228]

[64] National Aeronautics and Space Administration Website, "International Space Station Facts and Figures." Accessed November 30, 2011. [URL: http://www.nasa.gov/mission_pages/station/main/onthestation/facts_and_figures.html]

[65] Penn, J., Richardson, G., Brown, N., Ranieri, C., Henning, G., "Spacecraft Applications Enabled by High Powered Solar Array Technology." *28th Space Power Workshop*, Los Angeles, California, April 19-22, 2010.

[66] United States Government Federal Business Opportunities, "AXIOM-AMWSE_PRESOLICITATION_AND_BFI_ANNOUNCEMENT." Original Pre-Solicitation date February 9, 2011. Accessed November 30, 2011. [URL: https://www.fbo.gov/]

[67] Meink, T., Reinhardt, K., Luu, K., Blankinship, R., Huybrechts, S., Das, A., "PowerSail – A High Power Solution" *AIAA Space Conference and Exposition*, AIAA 2000-508, Long Beach, California, 19-21 September 2000.

[68] Kerslake, T., "Solar Electric Propulsion (SEP) Tug Power System Considerations" *29th Space Power Workshop*, Los Angeles, California, 18-21 April 2011.

[69] National Aeronautics and Space Administration Press Release 11-191, "NASA Issues Announcement For Solar Electric Propulsion Studies" June 17, 2011. [URL: http://www.nasa.gov/home/hqnews/2011/jun/HQ_11-191_Solar_Projects.html]

[70] Kurland, R., Stella, P., "Advanced Photovoltaic Solar Array Program Status." *Proceedings of the 24th Intersociety Energy Conversion Engineering Conference*, Washington DC, Vol. 2, 6-11 August 1989, pp. 829-834.

[71] "Advanced Photovoltaic Solar Array Design," NASA Final Report, NASA-CR-186345, JPL Contract No. 957358 (NAS7-918), 3 November 1986.

[72] Kimber, R., Regalado, O., Wu, C., "The EOS-AM Solar Array—A Flexible GaAs/Ge Array." Proceedings of the *23rd IEEE Photovoltaic Specialists Conference*, Louisville, Kentucky, 10-14 May 1993, pp. 1375-1380.

[73] Gerlach, L., Marks, G.W., Quittner, E., Renshall, J., Zwanenburg, R., "The Design of the L-SAT (Olympus) Solar Array," Proceedings of the *3rd European Symposium on Photovoltaic Generators in Space*, Bath, United Kingdom, 4-6 May 1982, pp. 241-248.

[74] Eskenazi, M., White, S., Spence, B., Douglas, M., Glick, M., Pavlick, A., Murphy, S., Oneil, M., McDanal, A., Piszczor, M., "Promising Results from Three NASA SBIR

Solar Array Technology Development Programs." NASA Final Report, NASA/CP—2005-213431, 2005.

[75] *Solar Cell Array Design Handbook*, Jet Propulsion Laboratory, NASA-CR-149364, Vol. 1, October 1976. Ch. 6.

[76] Paz, M., Leigh, W., *Structural Dynamics Theory and Computation*, Kluwer, Boston, 2004.

[77] "Design Data Handbook for Flexible Solar Array Systems" NASA Report N74-73793. NASA Contract NAS9-11039. Lockheed Missiles and Space Company. March 1973.

[78] Blevins, R., *Formulas for Natural Frequency and Mode Shape*, Krieger, Florida, 2001.

[79] Timoshenko, S. P., Gere, J., *Theory of Elastic Stability,* Dover, New York, 1961.

[80] *ABAQUS/Standard Users Manual*, Hibbitt, Karlsson, and Sorensen, Inc., Version 6.11-1, 2011.

[81] Alliant Tech Systems Data Sheet, "Coilable Boom Systems," Accessed 30 January 2014. [URL: http://www.atk.com/wp-content/uploads/2013/05/Coilable-2012.pdf]